Studies on Degradation Factors and Their Mitigation Methods of Cathode Materials for Advanced Lithium-ion Batteries

Satoshi Hashigami

March 2019

Contents

CHAPTER 3

Synthesis of SiO_2-modified Li_2MnO_3-$LiMn_{1/3}Ni_{1/3}Co_{1/3}O_2$ by Spray Pyrolysis with Acid Addition as Cathode Materials for Lithium-ion Batteries

CHAPTER 4

Durability Improvement of $LiNi_{0.5}Co_{0.2}Mn_{0.3}O_2$ Cathode Coated with Lithium Boron Oxide Glass Prepared by an Antisolvent Precipitation Method

CHAPTER 5

Influence of Lithium Silicate Coating on Retarding Crack Formation in $LiNi_{0.5}Co_{0.2}Mn_{0.3}O_2$ Cathode Particles

CHAPTER 6

Surface Modification of Spray Pyrolyzed $LiNi_{0.5}Co_{0.2}Mn_{0.3}O_2$ Cathode Particles with Lithium Boron Oxide

CHAPTER 7

General Conclusions and Publication List

CHAPTER 1

General Introduction

1.1 Significant Increase of Renewable Energy

Since the Industrial Revolution, energy consumption has increased along with the sophistication and diversification of energy use and improvement of living standards. Energy has been mainly produced from fossil fuels, but recognition of global warming in Japan and overseas is increasing. In recent years, the introduction of renewable energy from sunlight, wind power, solar heat, biomass, and ocean tides has begun to increase as we progress toward a low carbon society. Especially as a result of tight power supplies after the Great East Japan Earthquake, society's interest in energy conservation and renewable energy is growing. In addition to the proliferation of renewable energy, electricity system reform (the liberalization of electricity retail sales and the separation of power generation and transmission) and IT innovation are progressing in Japan. Therefore, new forms of power supply systems and business are being conceived, and their demonstration tests are being conducted in various places.

The large-scale introduction of renewable energy has been promoted politically by avoiding natural competition in the electricity market by increasing feed-in tariffs. However, renewable energy such as solar and wind power is not stable because the power generation output depends on weather conditions. As the proportion of these power sources increases, it places a burden on other power supplies for supply-demand

adjustment. For example, the operating rate of oil-fired and natural gas-fired power plants should be decreased. In addition, it causes supply stability problems including electricity generation surplus and overcrowding of transmission and distribution equipment. Moreover, in Hokkaido, Tohoku, and Kyushu areas in Japan, renewable energy resources are excessive compared to the demand, where problems of acceptability are beginning to emerge.

In this way, the recent trends in energy production are causing various problems in the electric power business, such as difficulties in maintaining the frequency and voltage of the grid power, and therefore some buffers are needed to absorb the output fluctuation from renewable energy. In the future, the supply capacity of electricity will increase as nuclear power plants are restarted and the introduction of renewable energy is expanded. However, it is expected that the need for power supply/demand adjustment will continue to grow due to an increase in unstable power sources such as renewable energy sources. The supply and demand of electric power have been adjusted by the supplier using output adjustment of thermal power plants and accommodating excess electricity to a wide area beyond their territory through regional interconnection lines. From now on, however, the efforts of the customer side, such as utilization of energy storage facilities including storage batteries, heat pumps, electric cars, and demand response (negawatt trading) using Energy Management System (EMS), will be more important.

As mentioned above, there is no negative opinion on the introduction of renewable energy itself, but it has been pointed out that the introduction of a large amount of renewable energy causes various problems arising from its instability. Electric power suppliers are required to fulfill their social mission in response to expectations from the society. Therefore, it is an urgent task for electric power suppliers to not only simply

manage the output fluctuations of renewable energy, but also to find a stable and sustainable method for utilizing renewable energy in the future.

1.2 Battery Materials for Energy Storage

There has been growing social interest in energy conservation and the introduction of renewable energy as awareness of power saving and risk management increases. Hence the development of energy storage technologies using batteries has attracted much attention to stabilize electricity supply and demand and to use the grid power more efficiently, which has stimulated research and development by various manufacturers and demonstration experiments by various local governments. Recent progress of energy storage technology has contradicted the common sense that "electricity cannot be stored". The technology not only compensates for the weakness of solar and wind power generation, i.e., unstable output, but also is effective as emergency power sources upon power outages and for a reduction of the power rate through peak cuts and peak shifts. It will therefore become a key technology of the electric power business in the future. In addition, the spread of storage batteries is expected to promote private consumption of solar power after the termination of Feed-In Tariff (FIT) of solar power surplus electricity and the promotion of Net Zero Energy Housing (ZEH).

Commercially available batteries in the domestic market include lead-acid batteries, nickel-cadmium batteries, nickel-metal hydride batteries, sodium-sulfur batteries, lithium-ion batteries (LIBs), and others. Of these, LIBs are currently attracting much attention as electric power storage devices in the domestic market. Large-sized stationary

LIB systems for grid power stabilization have been demonstrated by Tohoku Electric Power Co., Chugoku Electric Power Co., and other companies. Not only in electric power stabilization, but also in general households, LIBs have been considered useful as an emergency power source, and the movement to utilize storage batteries is expanding more and more in the near future.

However, LIBs also have some problems for these purposes. The biggest one is the degradation problem. For example, the internal resistance increases and the discharge capacity decreases with time or with repeated charge and discharge cycles (called capacity fading). It has been reported that the degradation factor of LIBs is complicated; e.g., the degradation factor during storage may be different from that during charge and discharge cycles. This is because capacity fading and its degradation mechanism have not been fully elucidated yet. LIBs for stationary use should be used for a long period of 20 years (Fig. 1-1, Battery Road Map 2013, New Energy and Industrial Technology Development). Since the degree of deterioration varies depending on the operating conditions of a battery, it is difficult to predict how much the battery deteriorates after 20 years when used in a supply/demand control system. When considering how to use the power storage device, the following considerations on battery characteristics are required: i) which range in state of charge (SOC) is the best for charge and discharge cycles, ii) which SOC is the best as a center for charge/discharge cycles, iii) how cycle characteristics change when other charge/discharge patterns are used, and iv) how capacity changes with temperature and current. Without these understandings, it is difficult to determine an appropriate battery capacity when designing a power storage device, or to guarantee the battery characteristics when proposing it to user companies.

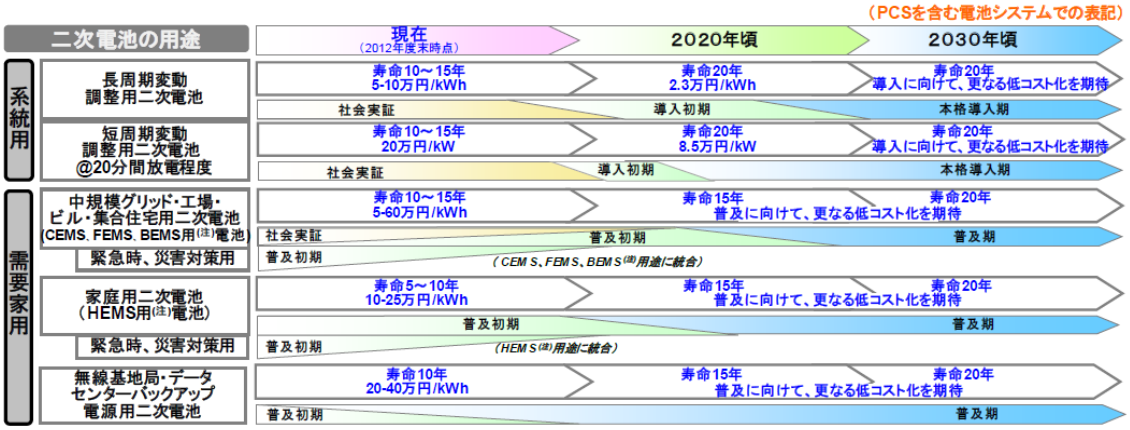

Fig. 1-1 New Energy and Industrial Technology Development Battery Road Map 2013.

In order to solve the above problems, it is indispensable for electric power companies to have technical capabilities to evaluate and predict deterioration of the battery not only from the viewpoint of the system, but also from the viewpoint of materials used in the battery. If we understand the deterioration factors, their mitigation methods, and the influence of temperature and charge/discharge rate on the performance of the storage battery, it will be possible to predict the degree of deterioration in advance. It will then be possible to decide how much we should use battery materials in a battery system with a high accuracy and when we should replace the batteries. It will also be possible to select which battery is the most suitable for load leveling or frequency control from a large variety of commercially available batteries. In order to balance the cost and reliability of batteries, it is necessary for electric power suppliers to understand deterioration factors of LIBs and establish guidelines on mitigation methods from the viewpoint of materials.

1.3 Lithium-ion Batteries

A lithium ion battery is a non-aqueous secondary battery having a lithium-containing transition metal compound as a cathode and a carbon material as a negative electrode [1, 2]. Fig. 1-2 shows the model of the reaction mechanism of the lithium ion battery [3]. Since the commercialization of LIBs by Sony in 1991, lithium cobalt oxide ($LiCoO_2$) having a layered rock-salt type (α-$NaFeO_2$ type), which was first reported by Goodenough et al. [4], has been used as a cathode and graphite as an anode for a long time until now [5]. The charge-discharge reactions are described as:

$$\text{Cathode: } LiCoO_2 \underset{\text{Discharge}}{\overset{\text{Charge}}{\rightleftarrows}} Li_{1-x}CoO_2 + xLi^+ + xe^- \quad \cdots (1\text{-}1)$$

$$\text{Anode: } 6C(\text{Graphite}) + xLi^+ + xe^- \underset{\text{Discharge}}{\overset{\text{Charge}}{\rightleftarrows}} Li_xC_6 \quad \cdots (1\text{-}2)$$

Lithium ions are de-intercalated from the cathode during charging and intercalated between the graphite layers of the anode as in Eqs. (1-1) and (1-2). The reverse reactions occur during discharging. The operating voltage and gravimetric energy density of this system are 3.7 V and 100-150 Wh kg^{-1}, respectively, which are higher than those of conventional nickel-metal hydride batteries and lead-acid batteries [3]. In particular, since the high voltage of 3.7 V can operate general semiconductor devices operating at 3.3 V with one battery, it worked advantageously for miniaturization and weight saving of portable electronic devices.

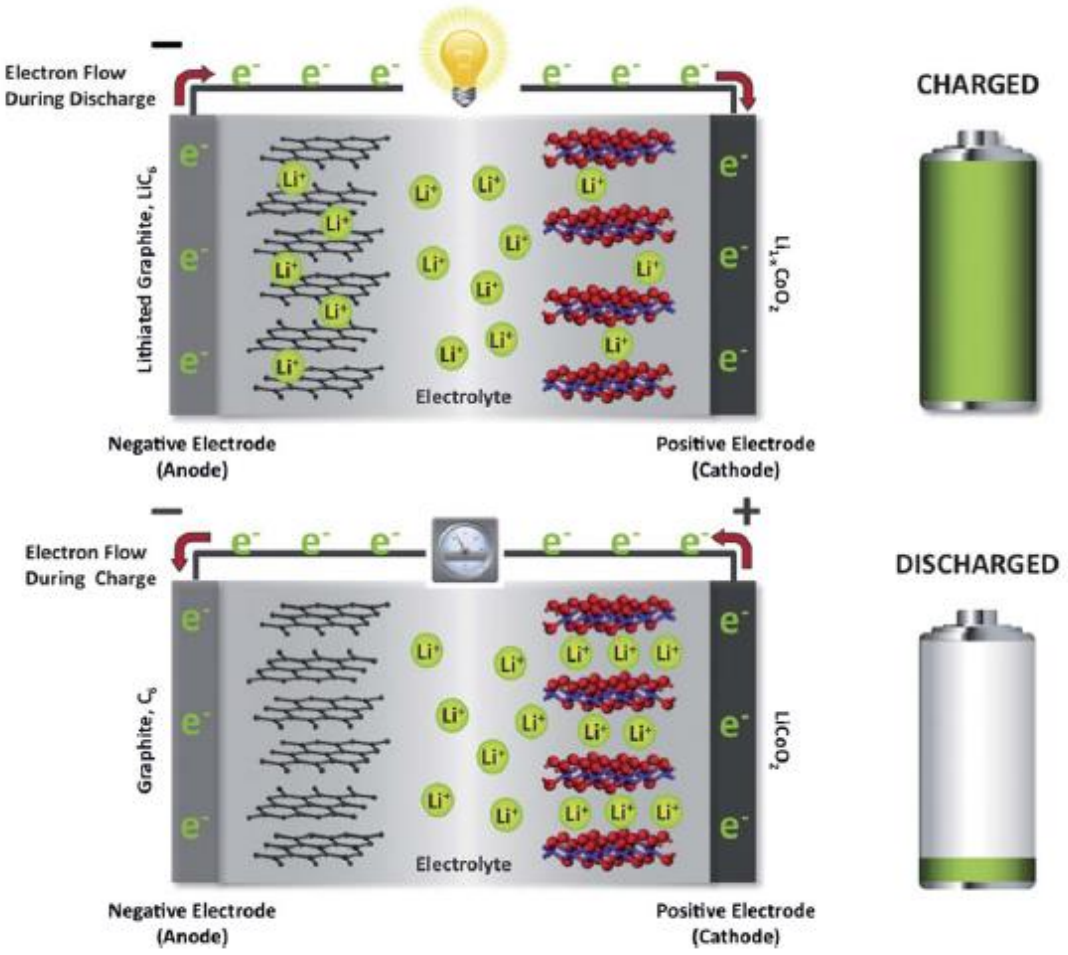

Fig. 1-2 A schematic illustration of the working principles of a $Li_xC_6/Li_{1-x}CoO_2$ lithium-ion cell. During discharge, lithium ions diffuse from a lithiated graphite (Li_xC_6) structure (the anode) into a delithiated $Li_{1-x}CoO_2$ structure (the cathode) with concomitant oxidation and reduction of the two electrodes, respectively. (M. M. Thackeray et al., Energy Environ. Sci. 5 (2012) 7854-7863.)

$LiCoO_2$ has a high working potential (ca. 3.9 V vs. Li/Li^+), a reasonable capacity of 140 mAh g^{-1} and good cycle performance. Fig. 1-3 shows the crystal structure of $LiCoO_2$ [6]. $LiCoO_2$ is an oxide having an α-$NaFeO_2$-type layered structure in which lithium ions

and cobalt ions occupy alternately the layer existing between cubic close-packed oxygen layers of a rock salt structure. It belongs to a hexagonal system with a space group of R3-m. This layered structure facilitates the diffusion of lithium ions within the lithium plane and is therefore suitable for the intercalation/de-intercalation reactions in the LIBs.

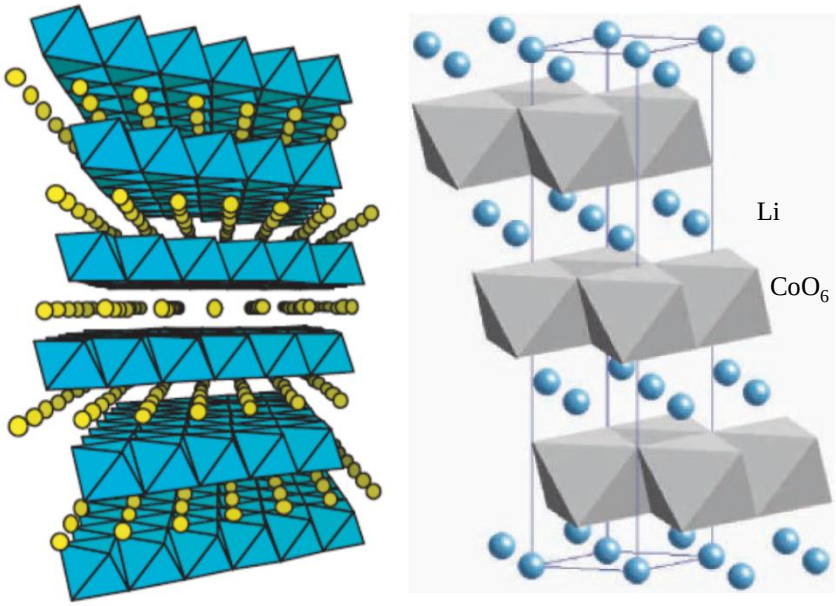

Fig. 1-3 Structures of an intercalation electrode, α-$NaFeO_2$ ($LiCoO_2$). (R. Kanno, GS Yuasa Technical Report 3(1) (2006) 1-11.)

Although the theoretical capacity of $LiCoO_2$ is 274 mAh g^{-1}, the cycle performance deteriorates remarkably when it is charged repeatedly to voltages higher than 4.2 V. This is because a phase transition from the hexagonal to a monoclinic phase occurs when more than half of the lithium ions in the cathode are de-intercalated during charging. When

charge and discharge cycles accompanying this phase transition are repeated, the volume changes upon the phase transition causes cracking of the active material particles, which results in severe degradation of the $LiCoO_2$ cathode. Hence the capacity is restricted at 140 mAh g^{-1} with an upper charging voltage limit of 4.2 V, which corresponds to nearly half of the theoretical capacity, in the commercially available cells. Cobalt used in $LiCoO_2$ is expensive because it is a rare-metal and its natural reserve is 8.3 million tons. Therefore it is important to decrease the amount of Co in the cathode materials to reduce the cost of the LIBs.

Lithium cobalt oxide co-substituted with manganese and nickel ($LiNi_xCo_yMn_zO_2$, $x + y + z = 1$) is called a layered ternary transition metal oxide. The active redox species contributing to charging and discharging is Ni^{2+}/Ni^{4+} and Co^{3+}/Co^{4+}, while the valence of manganese ion is unchanged at 4+ in the host structure [7]. Each transition metal element plays an important role. Nickel ions act as a main component for giving reversible capacity, and the charge/discharge capacity increases with an increase in nickel content. On the other hand, when the amount of nickel is increased too much, the crystal structure at charged states becomes unstable, which deteriorates the charge/discharge cycle performance and also thermal stability [8]. Cobalt ions also act as a capacity component. As the cobalt content increases, the working potential is increased slightly and the electrical conductivity is improved [9, 10]. Manganese ions have no role as a capacity component and mainly contribute to stabilization of the crystal structure during charging and discharging [11]. As the manganese content increases, the charge and discharge cyclic performance and thermal stability can be improved, and hence the upper voltage limit can be raised to a potential higher than 4.2 V. A typical composition of the layered ternary oxide is $LiNi_{1/3}Co_{1/3}Mn_{1/3}O_2$, in which the metal ratio is Ni: Co: Mn = 1:1:1. This cathode

material has already been used in commercially available cells because it can deliver a reasonable capacity of ca. 150 mAh g^{-1} with a lower cost and also has excellent thermal stability [12].

While LIBs have been so far used mainly in portable electronic devices since 1991, their applications such as hybrid vehicles (HVs), plug-in hybrid vehicles (PHVs) and electric vehicles (EVs) are now expanding every year because of their high energy density. The demand for high energy density has been increasing to improve the performance of these applications; therefore, materials for achieving high energy density are being developed intensively in the world. According to the Advanced and Innovative Storage Material Evaluation Technology Development (Phase 2) of National Institute for New Energy and Industrial Technology Development (NEDO), the trend for battery development is shown in Fig. 1-4. The gravimetric energy density of 150-200 Wh kg^{-1} of the present LIBs should be improved to 250-300 Wh kg^{-1} in the 2020's with advanced LIBs, while it should be further improved with all-solid batteries using lithium metal anode and sulfur cathode, and ultimately to achieve 500 Wh kg^{-1} in the 2030’s with innovative storage batteries such as multivalent ion batteries, lithium-air batteries, etc.

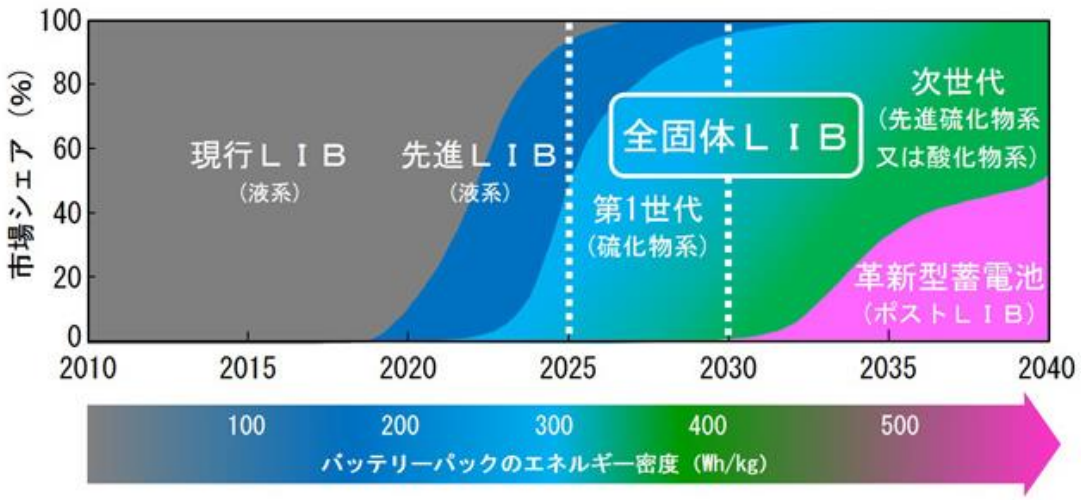

Fig. 1-4 Assumption of technology shift of EV battery.

It is widely recognized that the theoretical limit of the energy density of LIB is approximately 300 Wh kg^{-1}. In order to achieve an energy density of 500 Wh kg^{-1}, it is necessary to develop innovative rechargeable batteries that are not based on the principle of LIBs. It is therefore considered that enormous cost and time are required for their development and safety evaluation before practical use. On the other hand, if we can achieve 250-300 Wh kg^{-1}, which is close to the theoretical limit, with the advanced LIBs based on the principle of LIB, we can lower the cost of the total energy storage systems while ensuring the safety, and hence the advanced LIBs will accelerate the world-wide spread of large-scale power storage systems and emergency power supplies. Therefore advanced LIBs are also attracting much attention in the world. Silicon anode, which alloys with lithium, is the most promising candidate as an anode material in advanced LIBs because it has a very high capacity (4200 mAh g^{-1}). There have been many materials proposed so far as the candidates of the cathode materials for advance LIBs, they have

been recently narrowed down to the “lithium-rich layered ternary transition metal oxide cathodes” and the “high-nickel layered ternary transition metal oxide cathodes”. These two materials are now being recognized as practical cathode materials to replace $LiCoO_2$, spinel $LiMn_2O_4$, and $LiNi_{1/3}Co_{1/3}Mn_{1/3}O_2$ that are currently used in LIBs.

The lithium-rich layered ternary transition metal oxides (hereafter called Li-rich NCM) are solid-solution of Li_2MnO_3 and $LiMO_2$ (M = Co, Ni etc.), each of which has a layered structure. It has been reported that charging to 4.5 V (vs. Li / Li^+) or higher results in a very high capacity of about 250 mAh g^{-1}[13, 14]. The nickel-rich layered ternary transition metal oxides (hereafter called high-Ni NCM) are a series of materials with increased nickel contents based on $LiNi_xCo_yMn_zO_2$ (x + y + z = 1). For example, $LiNi_{0.5}Co_{0.2}Mn_{0.3}O_2$ (Ni: Co: Mn = 5: 2: 3) can deliver a high capacity of 200 mAh g^{-1} when charged to 4.6 V or higher [15]. In numerous recent reports including NEDO Battery Road Map 2013 (Fig. 1-5) and Annual Merit Review of U. S. Department of Energy (Figs. 1-6 and 1-7), Li-rich NCM and high-Ni NCM cathodes are highly expected as practical cathode materials in advanced LIBs that will be commercialized in the near future.

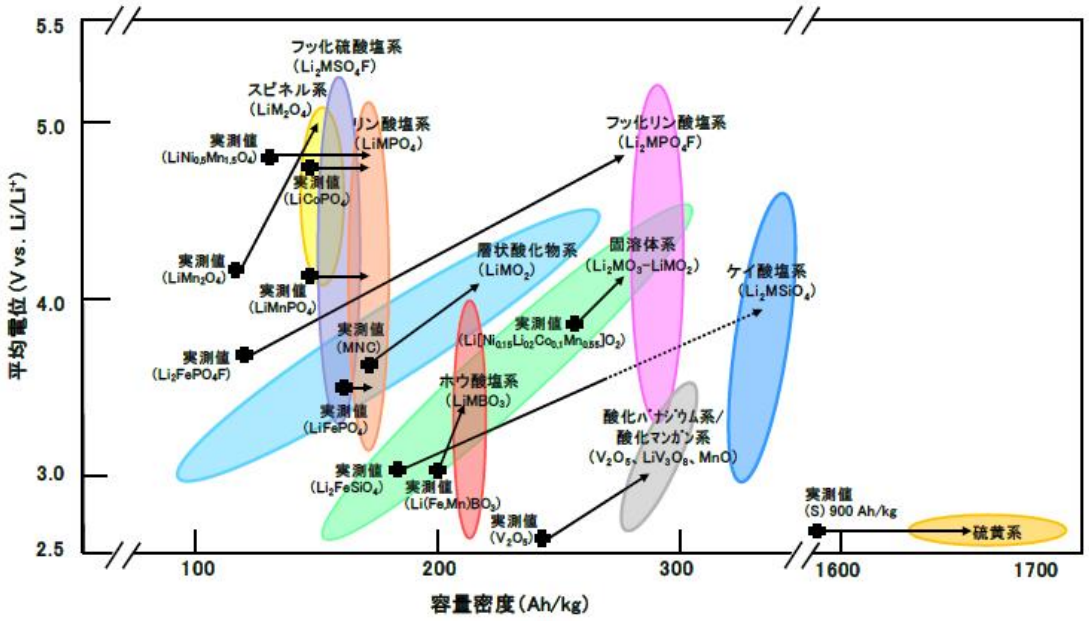

(1) ●は実測値（現行技術レベル、OCVで測定）、楕円は理論値（活物質単体の値）。矢印は改善の方向。
(2) 容量密度は、活物質単体が充・放電できるLiイオン量より計算された密度。

Fig. 1-5 New Energy and Industrial Technology Development Battery Road Map 2013.

RELEVANCE

Overall Project Objective

- Develop high-energy, long-life, safe high-nickel NMC cathodes
  - High-nickel NMC cathodes with a specific capacity of 200 – 250 mA h g^{-1}
  - Stabilization strategies for long cycle and calendar life
  - Stabilization strategies for acceptable thermal stability

Objectives for Year 2

- Synthesis scale-up and optimization of high-Ni NMC with in-depth investigation of their structure-morphology-property relationships
  - Scale up synthesis capacity with a careful control
  - Understand and suppress bulk and surface degradation during cycling
  - Assess and mitigate air sensitivity with compositional and surface control
  - Evaluate high-voltage cyclability and identify critical barriers
  - Balance energy density, cycle life, and thermal stability
  - Optimize electrochemical performance

BATTERY 500 CONSORTIUM — UNIVERSITY OF TEXAS AT AUSTIN

Fig. 1-6 Annual Merit Review of U. S. Department of Energy, Overview and Synthesis of high-Ni Nickel Manganese Cobalt Oxide (NMC) Cathodes.

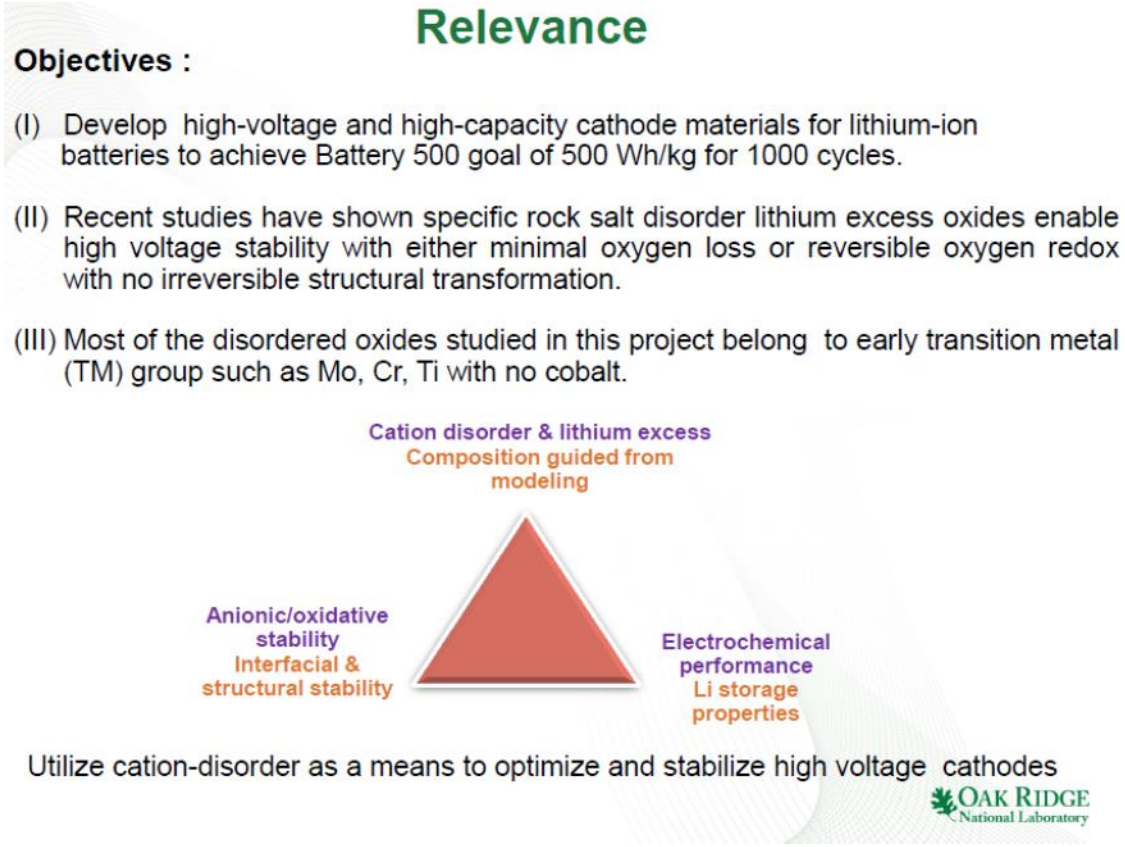

Fig. 1-7 Annual Merit Review of U. S. Department of Energy, High Capacity Multi-Lithium Oxide Cathodes and Oxygen Stability.

As described above, advanced LIBs having a higher energy density than the conventional ones are expected to be distributed in the 2020's. The Li-rich NCM cathode and the high-Ni NCM cathode are the most promising candidates for the cathode of the advanced LIBs. Though the high capacities of these cathode materials are attractive, they have still some problems, especially capacity fading upon cycling, to overcome before being used in commercially available cells. It is therefore necessary to understand the factors and mechanism for the capacity fading phenomena at the material level and to develop their mitigation methods before introduction into the market.

1.4 Li-rich NCM Cathodes for Advanced LIBs

Fig. 1-8 shows the crystal structure models of Li_2MnO_3 and $LiMO_2$ (M = Co, Ni etc.), which are the end members of the Li-rich NCM solid-solution cathode [16]. The basic structure of Li_2MnO_3 is close-packed layered rock salt type and can be rewritten as $Li[Li_{1/3}Mn_{2/3}]O_2$. This can be regarded as a layered structure similar to that of $LiCoO_2$ except that Li^+ and Mn^{4+} ions occupy the transition metal layer. The crystal structure of Li_2MnO_3 is a monoclinic crystal system with the C2/m space group [17]. The theoretical capacity of Li_2MnO_3 is as high as 344 mAh g^{-1}, but it is inactive to Li^+ intercalation/deintercalation [18]. On the other hand, $LiMO_2$ is active, but the practical capacity is moderate (about 140 mAh g^{-1}) as mentioned earlier. Therefore, lithium-rich NCM cathode was discovered based on the idea of obtaining a high capacity by solidifying Li_2MnO_3 and $LiMO_2$ to make the composition closer to the former while utilizing the high activity of the latter. In fact, charging to potentials higher than 4.5 V (vs. Li/Li^+), Li-rich NMC cathodes are activated, and give a high capacity of about 250 mAh g^{-1} as shown in Fig. 1-9 [16]. A plateau is observed at about 4.5 V on charging in the first cycle. According to Armstrong et al. [19], evolution of oxygen gas is observed at potentials above 4.5 V. Thus the plateau observed in the first charging process is an irreversible reaction and is considered to be related to oxygen loss from the Li-rich NCM cathode. Hong et al. suggested that elimination of Li^+ and O_2 is involved in the first charging reactions of the Li-rich NCM cathode as [20]:

$$LiMO_2 \rightarrow MO_2 + Li^+ + e^- \quad \cdots (1\text{-}3)$$

$$Li_2MnO_3 \rightarrow MnO_2 + 2Li^+ + 0.5O_2 + 2e^- \quad \cdots (1\text{-}4)$$

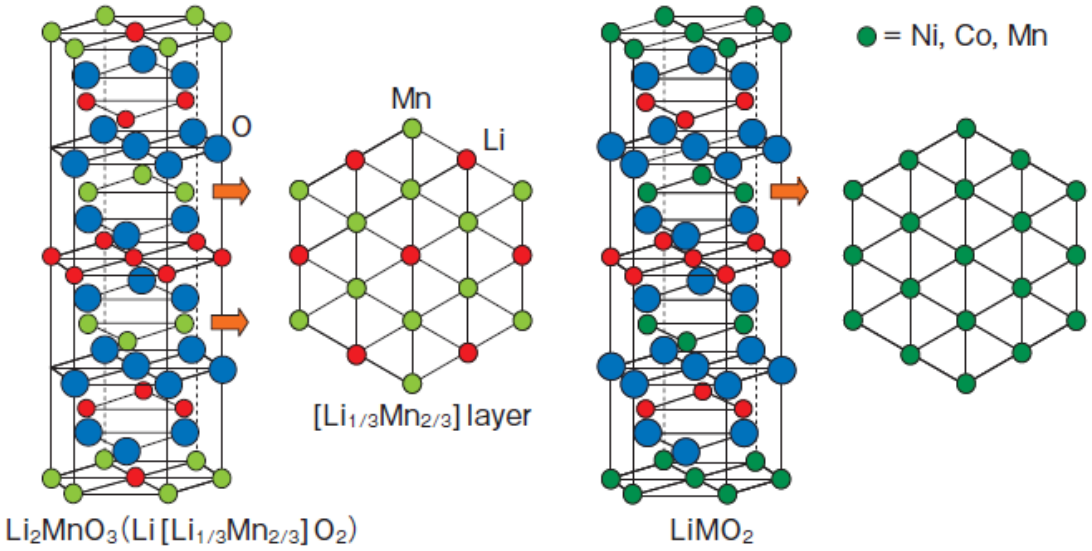

Fig. 1-8 The relationship between the crystal structures of Li_2MnO_3 and $LiMO_2$. (Y. Sato, FB Technical News, 66, (2011) 3-10.)

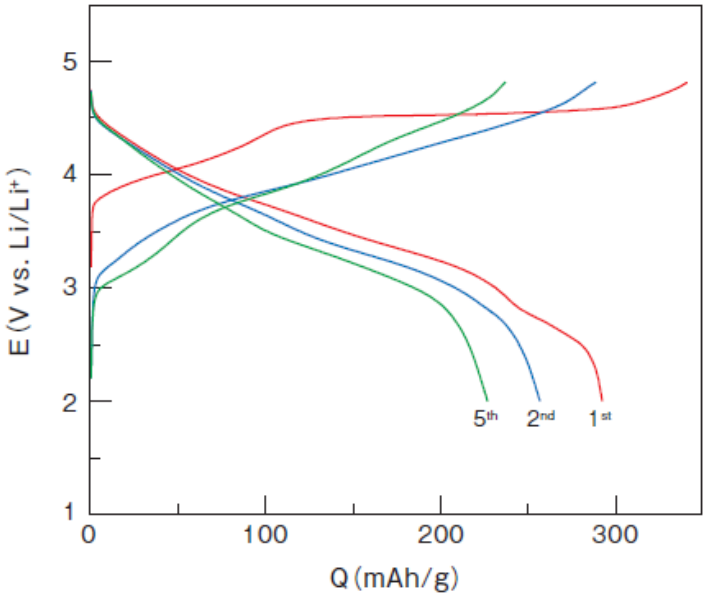

Fig. 1-9 Charge−discharge curves of $Li[Ni_{0.17}Li_{0.2}Co_{0.07}Mn_{0.56}]O_2$ between 2.0-4.8 V at 0.2 mA cm^{-2} and room temperature. (Y. Sato, FB Technical News, 66, (2011) 3-10.)

In this case, the discharge reaction is a reverse reaction of Eq. (1-3), and the theoretical capacity is calculated to be 252 mAh g^{-1}. However, many researchers have reported their practical capacities that greatly exceed 250 mAh g^{-1}, and it is not possible to explain the capacity higher than 250 mAh g^{-1} with the mechanism described above. Ohzuku et al. proposed that not only transition metal ions, but also O^{2-} ion takes part in the charging and discharging reactions, and partially oxidized O^{2-}, e.g. peroxide ion O_2^{-}, is formed inside the $Li[Li_{1/5}Ni^{2+}{}_{1/5}Mn^{4+}{}_{3/5}]O_2$ [21].

$$Li[Li_{1/5}Ni^{2+}{}_{1/5}Mn^{4+}{}_{3/5}]O_2$$

$$\rightarrow \square_{2/5}Li_{3/5}[Li_{1/5}Ni^{4+}{}_{1/5}Mn^{4+}{}_{3/5}]O_2 + 2/5\ Li^{+} + 2/5\ e^{-} \quad \cdots (1\text{-}5)$$

$$\square_{2/5}Li_{3/5}[Li_{1/5}Ni^{4+}{}_{1/5}Mn^{4+}{}_{3/5}]O_2$$

$$\rightarrow \square[\square_{1/5}Ni^{4+}{}_{1/5}Mn^{4+}{}_{3/5}](2O^{2-})_{3/5}(O_2^{2-})_{2/5} + 4/5\ Li^{+} + 4/5\ e^{-} \quad \cdots (1\text{-}6)$$

The theoretical capacity calculated from Eq. (1-5) is 126 mAh g^{-1} and that from Eq. (1-6) is 252 mAh g^{-1}. Therefore, the total reversible capacity is expected to be 378 mAh g^{-1}. In addition, Oishi et al. reported that the reversible appearance/disappearance of superoxide- and peroxide-like states during the charge/discharge reactions by using X-ray absorption spectroscopy [22]. From these results, it has been now widely recognized that a high capacity is given by a reversible oxide-anion redox, though the detailed charge and discharge mechanism of Li-rich NCM cathodes is still under debate.

One of serious problems of the Li-rich NCM cathodes is a severe capacity fading. It has been pointed out that the electrolyte solution is oxidized at high potentials during charging and the resulting decomposition products formed on the surface deteriorates the

cathode. Furthermore, it has confirmed that the metal ions are dissolved by the presence of hydrogen fluoride (HF) generated in a reaction between the lithium salts ($LiPF_6$) and moisture present in the electrolyte. Especially, the dissolution of Mn^{2+} ions is the most significant, which occurred through the disproportionation reaction of Mn^{3+} [23]. The dissolved Mn^{2+} ions are reduced at the graphite anode and the deposit gives a harmful effect on the cycle performance of the graphite anode.

It has been reported that surface modification (or coating) of the active material particles with a thin layer of an oxide is effective for mitigating deterioration phenomena of other types of cathode materials used in LIBs, such as the decomposition of the electrolyte at high potentials, and the dissolution of the transition metal ions from the cathode materials. Zheng et al. showed that the activity of extracted oxygen species from a Li-rich NCM, $Li[Li_{0.2}Mn_{0.54}Ni_{0.13}Co_{0.13}]O_2$, was greatly reduced and the decomposition of the electrolyte was significantly suppressed by AlF_3-coating using in situ differential electrochemical mass spectrometry [24]. Impregnation method has been studied for a long time as a surface modification method [25, 26]. Methods using polymeric processes [27] and mechano-chemical reactions [28] have been studied for uniform coating. It has been also reported that the addition of oxides particles to electrolyte solution is effective for suppressing degradation phenomena. Fu et al. reported that SiO_2 particles capture moisture in electrolyte solution [29], and Wu et al. reported that the addition of Li_2SiO_3 is effective for removing HF and PF_5 from electrolyte solution [30]. Though surface modification and additives to electrolyte have been repeatedly reported as techniques effective for suppressing degradation of the cathode particle/electrolyte interface in the literature, the detailed mechanism has not been elucidated. Apart from surface modification and additives, Sun et al. prepared particles of high-Ni NCM cathode with a

concentration gradient, and successfully improved the cycle performance [31]. Ito et al. reported that a stepwise increase of the upper voltage limit from 4.5 to 4.8 V in the initial charge/discharge cycles suppresses a structural change of the active material surface and improves the capacity retention during cycling [32].

Besides, the Li-rich cathodes have a problem in rate performance, which does not match with the requirement of today's lithium-ion batteries. Li et al. reported a high-rate capability by reducing the particle size and increasing the surface area [33]. It is widely known that the average voltage gradually decreases during cycling, which is also a big problem for practical use and called “voltage fading”. Though many researchers have tried to explain the mechanism for the voltage fading, there have been only a few examples suppressing the voltage fading. The voltage fading is widely believed to be caused by a structural change from the layered structure to a spinel structure; however, Gallagher et al. reported that reversible and irreversible transition metal migration phenomena causes the hysteresis on the charge/discharge curves and the voltage fading, respectively [34].

As described above, the Li-rich NCM cathodes are very attractive in advanced LIBs because of their high capacity that exceeds 250 mAh g^{-1}. However, there are several problems, such as capacity fading, voltage fading, transition metal ion dissolution, and poor rate-capability to be solved for practical use. Therefore the mechanisms for these degradation phenomena should be clarified in detail, and their mitigation methods should be developed to utilize the Li-rich NCM cathodes in advanced LIBs.

1.5 High-Ni NCM Cathodes for Advanced LIBs

The high-Ni NCM cathode is a series of materials based on $LiNi_xCo_yMn_zO_2$ (x + y + z = 1) in which the content of nickel is higher than that in $LiNi_{1/3}Co_{1/3}Mn_{1/3}O_2$ used already in commercially available cells. The crystal structure is the same as that of Li*M*O_2 shown in Fig. 1-8. The variations of the discharge capacity of high-Ni NCM cathodes of different Ni contents are shown in Fig. 1-10 [8]. The initial discharge capacity increases with increasing Ni content, and $LiNi_{0.8}Co_{0.1}Mn_{0.1}O_2$ (NCM811) can deliver a capacity of more than 200 mAh g^{-1} when charged to 4.3 V. However the capacity retention is poor as shown in Fig. 1-10 owing to its unstable crystal structure. It is also known that its thermal stability is poor, which causes a safety problem when the temperature is raised upon thermal runaway. On the other hand, moderately high-Ni $LiNi_{0.5}Co_{0.2}Mn_{0.3}O_2$ (NCM523) gives a reasonably high capacity of approximately 160 mAh g^{-1} with a good cycleability when charged to 4.3 V, and are hence attracting much attention as a promising cathode material from industry. The moderately high capacity of the NCM523 cathode can be further improved to 180-200 mAh g^{-1} when the upper voltage limit is raised to 4.6 V as shown in Fig. 1-11. The capacity of 200 mAh g^{-1} is attractive as a cathode in advanced LIBs; however, raising the upper voltage limit to 4.6 V again deteriorates cycleability.

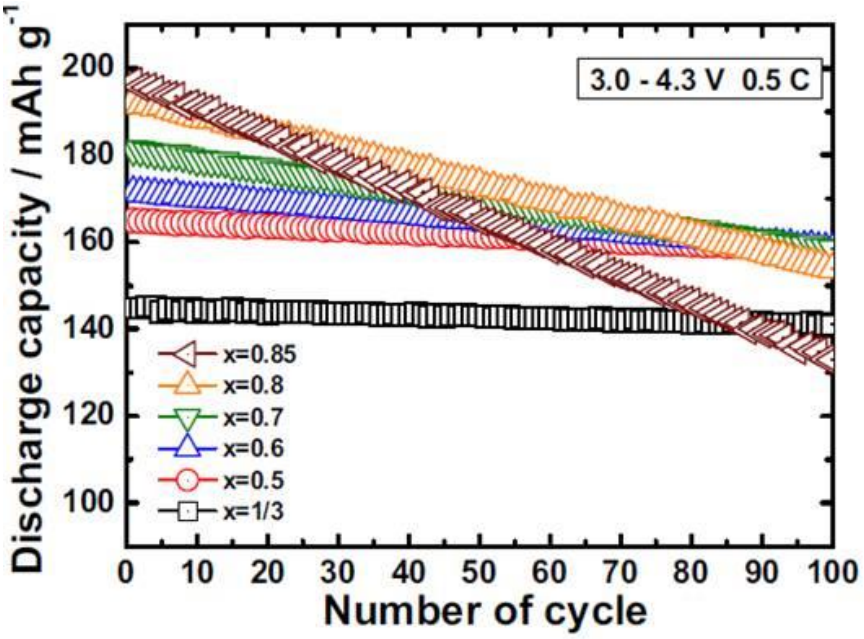

Fig. 1-10 Capacity retention of high-Ni NCM cathodes of different compositions between 3.0 and 4.3 V. (H.-J. Noh et al., J. Power Sources, 233 121-130 (2013).)

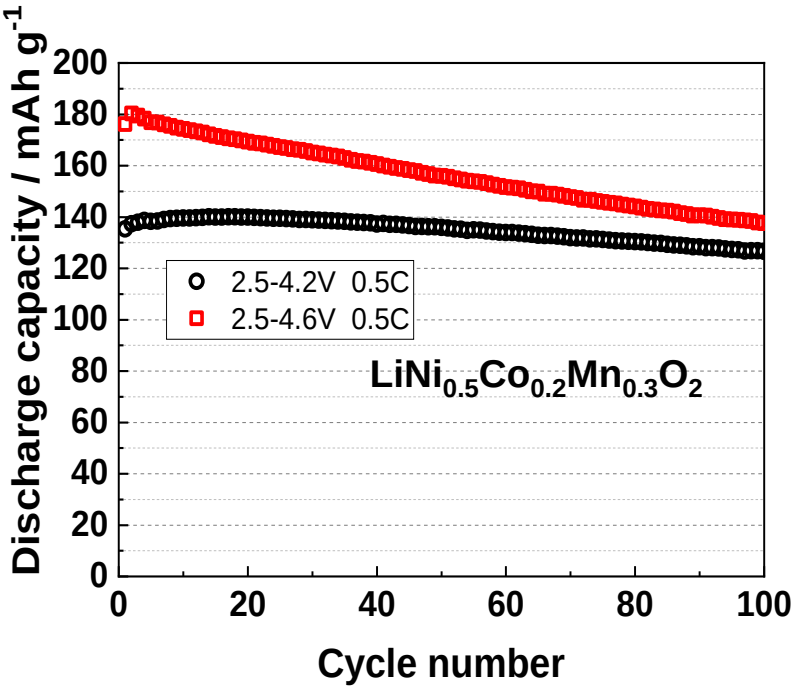

Fig. 1-11. Variations of discharge capacity of NCM523 cathode between 2.5 and 4.2 V and between 2.5 and 4.6 V (unpublished data).

The degradation mechanisms of NCM523 proposed so far are: i) Dissolution of metal ions from NCM523 particles by hydrogen fluoride, which is generated *via* the reaction between the lithium salts ($LiPF_6$) and moisture present in the electrolyte [35], ii) Deposition of oxidative decomposition products of the electrolyte solution on NCM523 particles [36], iii) Irreversible crystal structural change in the vicinity of the particle/electrolyte interface [37]. The higher the charging voltage is, the more electrolyte decomposition and the structural change become remarkable, which accelerates the capacity fading during cycling. Lin et al. reported that not only a surface reaction layer consisted of a LiF phase and a complex organic matrix, but also a surface reduction layer is formed on NCM523 particles after cycled between 2.0-4.3 V and 2.0-4.7 V [38]. June et al. reported that the formation of the spinel phase and rock salt phase on the NCM523 particle surface is dominant factor of deterioration during 3.0-4.8 V operation, which is attributable to the highly oxidative environment that triggers the oxygen loss from the surface [37].

In addition to these degradation mechanisms, it has been recently reported that crack formation inside the particles is an important degradation factor for high-Ni NCM cathodes as shown in Fig. 1-12 [39]. Cracks are formed inside a secondary particle by the expansion and contraction of the primary particles of the active material during cycling. In addition, oxidative decomposition of the electrolyte solution that penetrated inside through the cracks accelerates the disintegration of the secondary particles. Watanabe et al. reported that electrolyte decomposition products and a NiO-like phase were formed along the cracks formed at the grain boundaries of the secondary particles, which deteriorated remarkably the ionic/electronic conductivity of the cathode [40]. Ishidzu et al. showed that many micro cracks were generated at the grain boundary of the primary

particles for high-Ni $LiNi_{0.7}Co_{0.2}Mn_{0.1}O_2$ rather than $LiNi_{1/3}Co_{1/3}Mn_{1/3}O_2$ in the voltage region of 2.5 to 4.5 V at the current rate of 0.5 C and 40ºC for 100 cycles [41]. Ryu showed that the micro cracks in high-Ni $LiNi_{0.9}Co_{0.05}Mn_{0.05}O_2$ that connect the particle core to the surface could provide channels for electrolyte penetration, exposing the particle interior to the deleterious electrolyte reactions [39]. Furthermore, Yan et al. observed the formation of intragranular cracks besides the intergranular cracks in $LiNi_{1/3}Co_{1/3}Mn_{1/3}O_2$ cathode materials when cycling at 4.7 V [15].

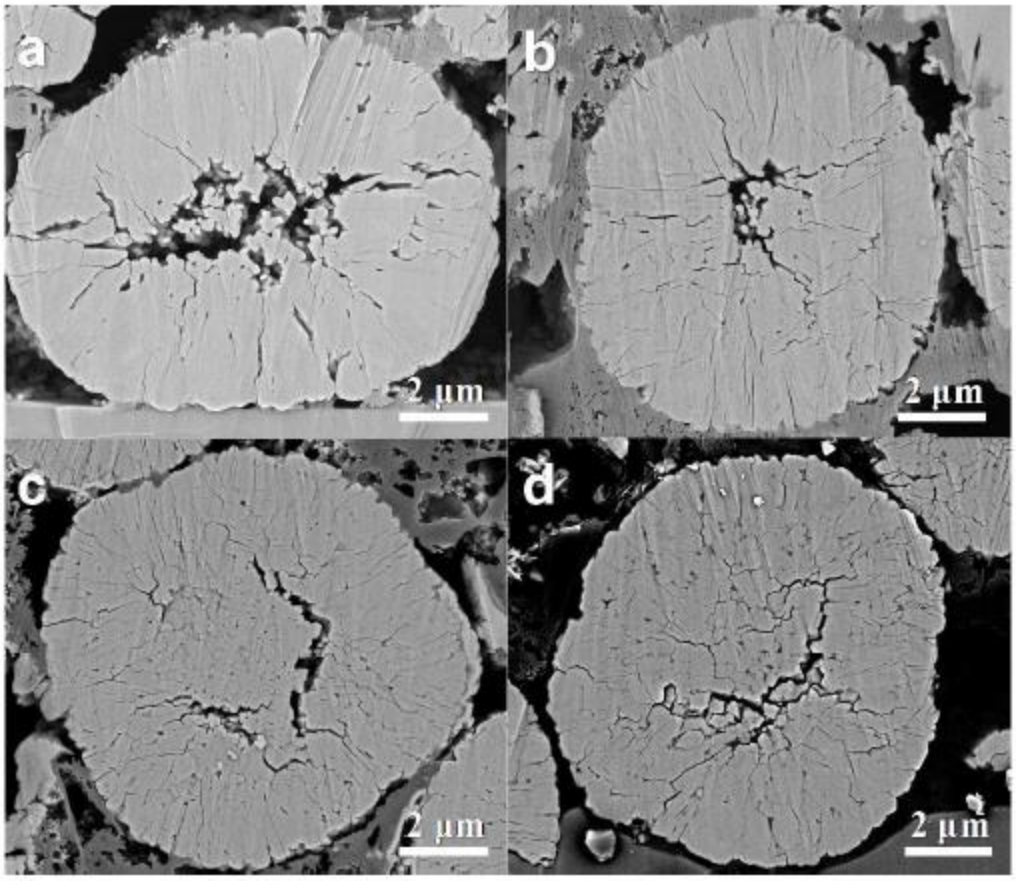

Fig. 1-12 Cross-sectional SEM images of the $Li_{1-\delta}[Ni_xCo_yMn_{1-x-y}]O_2$ cathodes in the fully charged state (at 4.3 V in the first charge cycle): (a) x = 0.6, (b) x = 0.8, (c) x = 0.9, and (d) x = 0.95. (H.-H. Ryu et al., Chem. Mater. 80 (2018) 1155-1163.)

The degradation mechanism of high-Ni NCM cathode is thus very complex, and the degradation factors seems to be classified into the two categories: (i) deterioration of the particle/electrolyte interface and (ii) disintegration of the secondary particles by crack formation along the grain boundaries during cycling. It is therefore important to distinguish the two categories and to solve the capacity fading of NCM523 cathodes. As in the case with other layered cathode materials, it has been reported that modifying the NCM523 particle surface with oxides is effective as an approach for suppressing direct contact with the electrolyte [42-46]. However, the influence of such surface modification on particle cracking has not been sufficiently clarified. Furthermore, in order to evaluate the influence of the electrode/electrolyte interface degradation discussed earlier, it is necessary to eliminate the influence of particle cracking.

1.6 Outline of the Work

As discussed in previous sections, Li-rich NCM and high-Ni NCM have higher capacities than conventional cathode materials in commercially available LIBs, and hence are promising cathode materials for advanced LIBs with high energy density, which are expected to be used for energy storage to utilize renewable energy and to stabilize electricity supply and demand in the future. However both materials suffer from the severe degradation and the capacity fading during cycling should be overcome before using in practical cells. The degradation mechanism of each cathode material is very complex and it is also important to understand the degradation mechanism for developing

the mitigation methods for capacity fading. In this thesis, the author focused on the surface modification of the active materials with oxides such as silicates and borates. The surfaces of Li-rich NCM and high-Ni NCM cathode particles were modified using a spray pyrolysis method and an antisolvent precipitation method, respectively, as mitigation methods for capacity fading. The degradation mechanisms were discussed in details and the roles of the surface modification in the improvement of cycle performance were discussed.

In Chapter 2, Li-rich Li_2MnO_3-$LiMn_{1/3}Ni_{1/3}Co_{1/3}O_2$ solid-solution cathode materials modified with SiO_2 were prepared by spray pyrolysis and their charge-discharge properties were investigated. Both the capacity and voltage fades of SiO_2-modified Li_2MnO_3-$LiMn_{1/3}Ni_{1/3}Co_{1/3}O_2$ during charge/discharge cycling were suppressed compared with that of the unmodified sample. It was found that the addition of SiO_2 suppressed the dissolution of manganese ions at 60ºC from the results of inductively coupled plasma (ICP) emission spectroscopy. X-ray diffraction (XRD) data indicated that weak reflections corresponding to Li_2SiO_3 appeared as the SiO_2 content increases to 5 wt%. Scanning electron microscope (SEM) studies showed that the microstructure of the particles was significantly changed by SiO_2 addition. As indicated by transmission electron microscope (TEM) analysis, Si-rich regions were seen on the Li_2MnO_3-$LiMn_{1/3}Ni_{1/3}Co_{1/3}O_2$ primary particles. The suppression of Mn ions and the improved charge and discharge properties were correlated with the microstructural changes.

In Chapter 3, SiO_2-modified Li-rich Li_2MnO_3-$LiMn_{1/3}Ni_{1/3}Co_{1/3}O_2$ cathode materials for LIBs were synthesized by a spray pyrolysis technique using starting

solutions containing citric acid and boric acid. SEM images showed that most of the particles using citric acid had spherical shapes and thin shell structures. Some particles were collapsed when the amount of citric acid was large. The specific surface area of the particles prepared from the citric acid-added solution was higher than that without citric acid. The addition of boric acid decreased the specific surface area of the material by acting as a sintering agent. The charge and discharge capacities for the synthesized materials were investigated and it was found that the addition of citric acid, which gave a higher specific surface area, enhanced the rate capability.

In Chapter 4, high-Ni $LiNi_{0.5}Co_{0.2}Mn_{0.3}O_2$ particles coated with lithium boron oxide (LBO) were prepared *via* an antisolvent precipitation and an impregnation method. Although crystalline borates were not detected from the LBO-coated sample, LBO powder prepared by the former method was $LiBO_2$, while a mixture of $LiBO_2$, $LiB_2O_4{\cdot}H_2O$ and $Li_2B_4O_9$ was obtained by the latter method. In the antisolvent precipitation method, the $LiNi_{0.5}Co_{0.2}Mn_{0.3}O_2$ particles were coated with a thin and uniform layer of $LiBO_2$. The capacity fading on charge/discharge cycling in the range of 2.5-4.6 V was suppressed for the LBO-coated samples prepared by the antisolvent precipitation method, while the impregnation method did not give clear effects. In addition, the rate capability was also improved by the antisolvent precipitation method.

In Chapter 5, high-Ni $LiNi_{0.5}Co_{0.2}Mn_{0.3}O_2$ particles coated with lithium silicate were prepared *via* an antisolvent precipitation method and their charge and discharge properties were investigated. The capacity retention of the lithium silicate-coated $LiNi_{0.5}Co_{0.2}Mn_{0.3}O_2$ was improved. Cross-sectional scanning electron microscope images

revealed that extensive cracks were formed within the uncoated $LiNi_{0.5}Co_{0.2}Mn_{0.3}O_2$ particles along the grain boundaries after the charge and discharge cycling, while the crack generation was significantly inhibited for the coated particles. From cross-sectional transmission electron microscope analysis, it was shown that Si-rich regions were concentrated not only on the surface, but also at the grain boundaries even at a depth of 400 nm from the surface of the lithium silicate-coated sample.

In Chapter 6, spray pyrolyzed high-Ni $LiNi_{0.5}Co_{0.2}Mn_{0.3}O_2$ cathode particles were coated with lithium boron oxide by an antisolvent precipitation method and their charge and discharge properties were investigated. The electrochemical impedance spectroscopy indicated that the stable impedance of the LBO-coated samples during cycling gave improved cyclic performance. The LBO coating layer was not changed in morphology and was maintained on the surface of $LiNi_{0.5}Co_{0.2}Mn_{0.3}O_2$ after cycling. Crack formation was not observed because of a small particle size of less than 1 μm. Hard x-ray photoelectron spectroscopy (HAXPES) revealed that the LBO coating suppressed the formation of LiF and organic decomposition products on the cathode particle surface. Furthermore, it suggested that the LBO-coated samples had a high durability against surface structural transformation caused by the reduction of surface Co during cycling.

In Chapter 7, the degradation factors and their suppression methods obtained in this thesis were summarized, and the prospects for practical application of Li-rich NCM and high-Ni NCM cathode materials were proposed.

References

[1] J. B. Goodenough and K.-S. Park, J. Am. Chem. Soc. 135 (2013) 1167-1176.

[2] J. B. Goodenough and Y. Kim, Chem. Mater. 22 (2010) 587-603.

[3] M. M. Thackeray et al., Energy Environ. Sci. 5 (2012) 7854-7863.

[4] K. Mizushima, P. C. Jones, P. J. Wiseman and J.B. Goodenough, Mat. Res. Bull. 15 (1980) 783-789.

[5] J.-M. Tarascon and M. Armand, Nature 414 (2001) 359-367.

[6] R. Kanno, GS Yuasa Technical Report, 3(1) (2006) 1-11.

[7] Y. Koyama, N. Yabuuchi, I. Tanaka, H. Adachi, T. Ohzuku, 151(10) (2004) A1545-A1551.

[8] H.-J. Noh, S. Youn, C. S. Yoon, Y.-K. Sun, J. Power Sources 233 (2013) 121-130.

[9] T. Ohzuku, A. Ueda, M. Nagayama, Y. Iwakoshi, H. Komori, 38(9) (1993) 1159-1167.

[10] C. Delmas, and I. Saadoune, Solid State tonics 370 (1992) 53-56.

[11] P. Yan, J. Zheng, J.-G. Zhang, C. Wang, Nano Lett. 17 (2017) 3946-3951.

[12] T. Liu, A. Garsuch, F. Chesneau, B. L. Lucht, J. Power Sources 269 (2014) 920-926.

[13] Z. Lu, J. R. Dahn, J. Electrochem. Soc. 149 (2002) A815-A822.

[14] M. M. Thackeray, C. S. Johnson, J. T. Vaughey, N. Li, S. A. Hackney, J. Mater. Chem. 15 (2005) 2257-2267.

[15] P. Yan, J. Zheng, M. Gu, J. Xiao, J.-G. Zhang, C.-M. Wang, Nat. Commun. 8 (2017) 14101.

[16] Y. Sato, FB Technical News 66 (2011) 3-10.

[17] K. Numata, C. Sakaki, S. Yamanaka, Chem. Lett. 8 (1997) 725-726.

[18] D. Y. W. Yu, K. Yanagida, Y. Kato, H. Nakamura, J. Electrochem. Soc. 156, (2009)

A417-A424.

[19] A. R. Armstrong, M. Holzapfel, P. Novak, C. S. Johnson, S. H. Kang, M. M. Thackeray, P. G. Bruce, J. Am. Chem. Soc. 128 (2006) 8694-8698.

[20] S. H. Kang, M. M. Thackeray, Electrochem. Commun. 11 (2009) 748-751.

[21] T. Ohzuku, M. Nagayama, K. Tsuji, K. Ariyoshi, J. Mater. Chem. 21 (2011) 10179-10188.

[22] M. Oishi, K. Yamanaka, I. Watanabe, K. Shimoda, T. Matsunaga, H. Arai, Y. Ukyo, Y. Uchimoto, Z. Ogumi, T. Ohta, J. Mater. Chem. A 4 (2016), 9293-9302.

[23] L. F. Wang, C. C. Ou, K. A. Striebel, J. S. Chen, J. Electrochem. Soc. 150(7) (2003) A905-A911.

[24] J. M. Zheng, Z. R. Zhang, X. B. Wu, Z. X. Dongk, Z. Zhu, Y. Yang, J. Electrochem. Soc. 155(10) (2008) A775-A782.

[25] S. T. Myung, K. Izumi, S. Komaba, Y. K. Sun, H. Yashiro, N. Kumagai, Chem. Mater. 17 (2005) 3695-3704.

[26] Z. Chen, J. R. Dahn, Electrochem. Solid-State Lett. 6(11) (2003) A221-A224.

[27] D. Arumugam, G. P. Kalaignan, J. Electroanal. Chem. 624 (2008) 197-204.

[28] H. Kobayashi, T. Okumura, M. Shikano, K. Takada, Y. Arachi, H. Nitani, Solid State Ionics 262 (2014) 43-48.

[29] Y. B. Fu, X. Ma, Q. H. Yang, X. F. Zong, Mater. Lett. 57 (2003) 1759-1764.

[30] B. Wu, Y. Ren, D. Mu, X. Liu, F. Wu, Electrochim. Acta 143 (2014) 324-330.

[31] Y. K. Sun, S. T. Myung, M. H. Kim, J. Prakash, K. Amine, 127 J. Am. Chem. Soc. 127 (2005) 13411-13418.

[32] A. Ito, D. Li, Y. Ohsawa, Y. Sato, J. Power Sources 183, (2008) 344-346.

[33] J. Li, R. Klopsch, M. C. Stan, S. Nowak, M. Kunze, M. Winter, S. Passerini, J. Power

Sources 196 (2011) 4821-4825.

[34] K. G. Gallagher, J. R. Croy, M. Balasubramanian, M. Bettge, D. P. Abraham, A. K. Burrell, M. M. Thackeray, Electrochem. Commun. 33 (2013) 96-98.

[35] J. A. Gilbert, I. A. Shkrob, D. P. Abraham, J. Electrochem. Soc. 164(2) (2017) A389-A399.

[36] M. Borner, F. Horsthemke, F. Kollmer, S. Haseloff, A. Friesen, P. Niehoff, S. Nowak, M. Winter, F. M. Schappacher, J. Power Sources 335 (2016) 45-55.

[37] S.-K. Jung, H. Gwon, J. Hong, K.-Y. Park, D.-H. Seo, H. Kim, J. Hyun, W. Yang, K. Kang, Adv. Energy Mater. 4 (2014) 1300787.

[38] F. Lin, L. M. Markus, D. Nordlund, T.-C. Weng, M. D. Asta, H. L. Xin, M. M. Doeff, Nat. Commun. 5 (2014) 3529.

[39] S. Watanabe, M. Kinoshita, T. Hosokawa, K. Morigaki, K. Nakura, J. Power Sources 258 (2014) 210-217.

[40] K. Ishidzu, Y. Oka, T. Nakamura, Solid State Ionics 288 (2016) 176-179.

[41] H.-H. Ryu, K.-J. Park, C. S. Yoon, Y.-K. Sun, Chem. Mater. 80 (2018) 1155-1163.

[42] K. Liu, G.-L. Yang, Y. Dong, T. Shi, and L. Chen, J. Power Sources 281 (2015) 370-377.

[43] Y. Shi, M. Zhang, D. Qian, Y. S. Meng, Electrochim. Acta 203 (2016) 154-161.

[44] W. Liu, M. Wang, X. L. Gao, W. Zhang, J. Chen, H. Zhou, X. Zhang, J. Alloys Comp. 543 (2012) 181-188.

[45] J.-Z. Kong, S.-S. Wang, G.-A. Tai, L. Zhu, L.-G. Wang, H.-F. Zhai, D. Wu, A.-D. Li, H. Li, J. Alloys Comp. 657 (2016) 593-600.

[46] D. Wang, X. Li, Z. Wang, H. Guo, X. Chen, X. Zheng, Y. Xu, J. Ru, Electrochim. Acta 174 (2015) 1225-1233.

CHAPTER 2

Suppression of Manganese-ion Dissolution by SiO_2 Aerosol Addition from Spray Pyrolyzed Li_2MnO_3-$LiMn_{1/3}Ni_{1/3}Co_{1/3}O_2$

2.1 Introduction

Lithium ion batteries with high energy density have a vital role as power sources, such as in portable devices and electric vehicles (EVs). The requirement for high capacity has grown recently to extend the driving range of EVs. High capacity cells are also being pursued for use in electric power grids with the aim of load frequency control and supply-demand control. A lithium-rich layered solid solution of Li_2MnO_3 and $LiMO_2$, where *M* denotes at least one 3*d* transition metal, has attracted much attention as a cathode material of lithium ion batteries in recent years because it offers high capacities of around 250 mAh g^{-1} within the potential range of 2.0 to 4.8 V (versus Li/Li^+) [1-4]. In the solid solution system, layered xLi_2MnO_3-$(1-x)LiMn_{0.33}Ni_{0.33}Co_{0.33}O_2$ electrodes have been reported to be promising because of their high capacities [5]. However, the cycle performance of the layered materials is not satisfactory at present. Another critical issue of the materials is the voltage fade during charge and discharge cycling. Croy et al. have reported a correlation between voltage fade and hysteresis in the charge/discharge profiles [6, 7]. The layered electrode materials such as $0.5Li_2MnO_3 \cdot 0.5LiMn_{0.375}Ni_{0.375}Co_{0.25}O_2$ exhibit a significant hysteresis loop, which is considerably different from other traditional lithium insertion electrode materials [6]. To account for this hysteresis, both the reversible

and irreversible migrations of transition metal ions were proposed [7].

Studies in the literature have so far revealed several important factors for the capacity fade of the layered materials, which include the dissolution of Mn ions into electrolytes [8], the decomposition of electrolytes through side reactions of $LiPF_6$ with water molecules [9], and structural transformations to a spinel-like phase on the surface [10]. One effective approach is to modify the surface with various oxides such as SiO_2 [8, 9], Al_2O_3 [11], ZrO_2 [12], TiO_2 [13], $Li_2O{\cdot}2B_2O_3$-glass [14], etc. They revealed that the surface modification suppresses the dissolution of Mn ions into the electrolytes as well as the decomposition of the electrolytes at high potentials.

Spray pyrolysis is a simple one-step synthesis technique to obtain various kinds of functional oxide powders [15, 16]. As compared with conventional solid-state methods, the particles prepared by spray pyrolysis have some advantages such as small particle size distribution, high purity, and easy control in composition and morphology of multi-component metal oxides. We have developed a synthetic method to prepare core-shell type particles for solid oxide fuel cell anode cermets using spray pyrolysis [17-19]. Such peculiar microstructures of oxide particles obtained by spray pyrolysis may produce unique properties in Li_2MnO_3-$LiMn_{1/3}Ni_{1/3}Co_{1/3}O_2$ as a cathode in lithium-ion batteries. It has been reported that Li_2MnO_3-$LiMn_{1/3}Ni_{1/3}Co_{1/3}O_2$ powder prepared by spray pyrolysis exhibited good charge and discharge performance [20, 21]. Furthermore, the powder morphology can be controlled by acid addition to the starting solution of spray pyrolysis [18, 22].

In Chapter 2, Li_2MnO_3-$LiMn_{1/3}Ni_{1/3}Co_{1/3}O_2$ modified with SiO_2 aerosol was synthesized by simple single-step spray pyrolysis. Li et al. modified $LiCoO_2$ with SiO_2 by mechano-thermal coating procedure [23]. Arumugam et al. reported that SiO_2-coated

$LiMn_2O_4$ significantly improved the capacity retention compared to the uncoated samples because of the reduction of Mn dissolution [8]. Furthermore, addition of SiO_2 to organic electrolyte has proved to be effective in trapping impurities [9]. To the best of our knowledge, SiO_2-modified Li_2MnO_3-$LiMn_{1/3}Ni_{1/3}Co_{1/3}O_2$ powder has never been prepared by spray pyrolysis until now. It was found that a small amount of SiO_2 addition remarkably suppressed the capacity and voltage fade of Li_2MnO_3-$LiMn_{1/3}Ni_{1/3}Co_{1/3}O_2$ during cycling. The microstructures of the particles and the dissolution of Mn ions at an elevated temperature of 60ºC were investigated in detail, and were correlated with the improved charge and discharge properties.

2.2 Experimental

2.2.1 Preparation of the cathode materials by spray pyrolysis

Stoichiometric amounts of lithium nitrate (99.9%, Wako Pure Chemical Industries, Ltd.), manganese nitrate hexahydrate (99.9%, Wako Pure Chemical Industries, Ltd.), nickel nitrate hexahydrate (99.9%, Wako Pure Chemical Industries, Ltd.), and cobalt nitrate hexahydrate (99.0%, Wako Pure Chemical Industries, Ltd.) were weighed to prepare 0.2 mol of Li_2MnO_3-$LiMn_{1/3}Ni_{1/3}Co_{1/3}O_2$, and were dissolved in 500 mL of deionized water. SiO_2 aerosol (Nissan Chemical Ltd., ST-O type) was added to the solution at a weight ratio of Li_2MnO_3-$LiMn_{1/3}Ni_{1/3}Co_{1/3}O_2$:$SiO_2$ = 100:0, 99:1, 98:2, or 95:5. The solution was stirred for an hour, diluted with deionized water to 1 L, and was used for spray pyrolysis.

Li_2MnO_3-$LiMn_{1/3}Ni_{1/3}Co_{1/3}O_2$ particles modified with SiO_2 were synthesized with a spray pyrolysis apparatus described in Fig. 2-1. The solution was atomized using ultrasonic vibrators with an oscillation frequency of 1.65 MHz in an atomizing vessel. Because the ultrasonic vibrators raise the temperature of the solution during atomizing, cold water was circulated around the atomizing vessel to keep the temperature of the solutions lower than 30ºC. This is because atomization at high temperatures tends to give inhomogeneous droplets. The reaction furnace consisted of four independent heating zones, whose temperatures were set at 200, 400, 800, and 800ºC from the inlet to the outlet. The atomized mists were flown into the furnace with 1 L min^{-1} of air. The droplets including Li^+, Mn^{2+}, Co^{2+}, Ni^{2+} and SiO_2 were dried, decomposed, reacted, and sintered when passing through the reaction furnace. The powder was collected using a membrane

filter, and was heat-treated at 800ºC for 3 h in air.

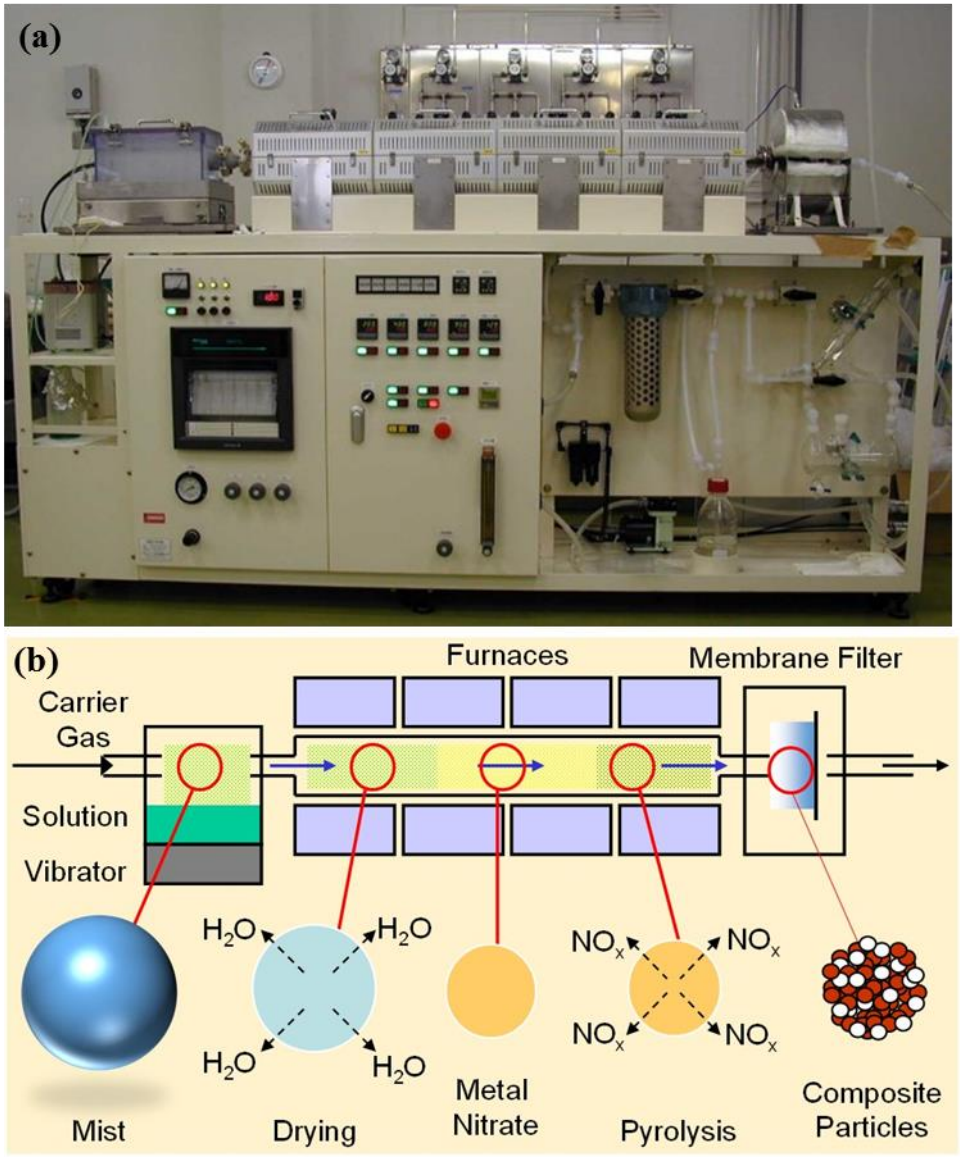

Fig. 2-1 (a) Spray pyrolysis apparatus and (b) schematic illustration of spray pyrolysis.

2.2.2 Cell fabrication and charge/discharge tests

A cathode slurry was prepared by mixing the oxide powder (80 wt.%), an acetylene black conductor (Denka Co., Ltd., 10 wt.%), a polyvinylidene fluoride binder (Kureha Corp., 10 wt.%) using 1-methyl-2-pyrrolidinone (Wako Pure Chemical Industries, Ltd.) as a solvent. The slurry was coated on an Al foil current collector (20 μm thickness), and dried at 120ºC for 24 h under vacuum. The loading of the cathode was typically 1.5 mg cm^{-2}.

Charge and discharge tests were carried out using two-electrode coin-type cells, which were assembled in an Ar-filled glove box (Miwa, MDB-1NKP-DS). Li metal foil (Honjo Metal) was used as a counter electrode, and a micro-porous monolayer membrane (Celgard® 2400) was used as a separator. The electrolyte solution was 1 M $LiPF_6$ dissolved in a 1:1 mixture of ethylene carbonate (EC) and dimethylcarbonate (DMC) by volume. The tests were performed galvanostatically at a 0.1 C rate (1 C = 314 mAh g^{-1}) between 2.0 and 4.8 V at 30ºC using a BTS2004W-10 battery test system (Nagano Co. Ltd.). Prior to cycling, a stepwise pre-cycling treatment was carried out by increasing the upper potential limit by 0.1 V from 4.5 V every two cycles to 4.8 V according to the procedure proposed by Ito et al. [24].

2.2.3 Powder characterization

The crystal structures of the Li_2MnO_3-$LiMn_{1/3}Ni_{1/3}Co_{1/3}O_2$ powders unmodified and modified with SiO_2 were investigated by X-ray diffraction (XRD, Shimadzu XRD-6000) using Cu Kα radiation. The morphology of the oxide particles was observed with a

scanning electron microscope (SEM, JSM-7001FD) using a secondary electron detector and with a transmission electron microscope (TEM, JEM-2100F) equipped with an energy dispersive X-ray spectroscopy (EDX). The oxide particles were embedded in a polymer resin, and samples for SEM and TEM observation were prepared by a cross-section polisher (JEOL, SM-09010DM) and a focused ion beam system (Hitachi, FB2000A), respectively. The BET surface area of the powder was measured with a Micromeritics TriStar.

2.2.4 Analysis of dissolved manganese-ions

In order to evaluate the effect of SiO_2 addition on manganese-ion dissolution, the amount of dissolved Mn ions was analyzed. The cell was pre-cycled stepwisely to 4.8 V, and stored at 60ºC for 3 days under the open-circuit conditions as an accelerated test. After disassembled the cell, the Li metal foil, on which Mn species were deposited, was soaked in ultra-pure water. The solution is acidified to 1 mol L^{-1} with hydrochloric acid, and Mn species were measured by inductively coupled plasma emission spectroscopy (ICP, Thermo Fisher Scientific, iCAP 6000 SERIES).

2.3 Results and Discussion

2.3.1 Structure and morphology analysis

XRD patterns of unmodified and SiO_2-modified Li_2MnO_3-$LiMn_{1/3}Ni_{1/3}Co_{1/3}O_2$ are shown in Fig. 2-2. The XRD pattern of each sample was typical of the Li_2MnO_3-$LiMn_{1/3}Ni_{1/3}Co_{1/3}O_2$ layered structure because the weak superstructure reflections appeared at around $2\theta = 22^{\circ}$, which originates from the ordering between the Li_2MnO_3 and the Li*M*O_2. The intensity ratio of the (003) to the (104) lines is known to be a measure of the cation mixing [25]; however, it was not appreciably changed by SiO_2 modification in the present study. The decrease in the (003)/(104) ratio means an increase in cation mixing caused by Li^+/H^+ exchange due to the strong acid such as nitric acid and the migration of transition metal cations into the lithium-ion layer during the annealing (drying) of the electrode, which results in poor cycling stability [26]. Before heat-treatment at 800ºC for 3 h (not shown), each powder had poor crystallinity and the peaks at around $2\theta = 22^{\circ}$ were not observed because of a short residence time (< 30 s) in the reaction furnaces.

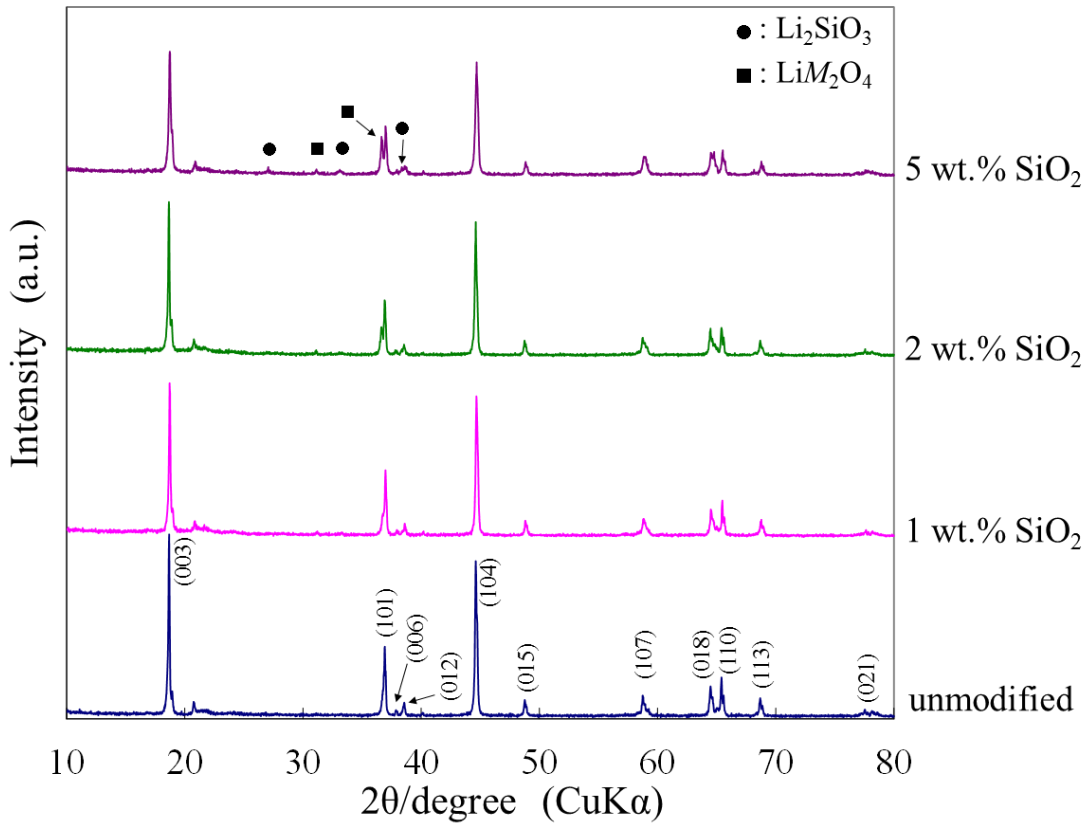

Fig. 2-2 X-ray diffraction patterns of Li_2MnO_3-$LiMn_{1/3}Ni_{1/3}Co_{1/3}O_2$ unmodified and modified with 1, 2, and 5 wt.% SiO_2 prepared by spray pyrolysis, followed by calcination at 800ºC for 3 h.

A clearly resolved peak was observed at 36.6º, which is not assigned to the layered oxide, and its intensity increased with SiO_2 content to 5 wt.%. This peak is assigned to the spinel LiM_2O_4 phase such as $LiNi_{0.3}Co_{0.4}Mn_{1.3}O_4$ and $LiNi_{0.2}Co_{0.6}Mn_{1.2}O_4$. Kang et al. reported that a $0.5Li_2MnO_3$-$0.5LiNi_{0.44}Co_{0.25}Mn_{0.31}O_2$ sample after acid-treated for 2 weeks showed a similar doublet peak in the range of 36.0-39.0º [27]. Besides, a weak reflection appeared at 2θ = 31.1-31.2º when SiO_2 was added, which is also assigned to

the spinel LiM_2O_4 phase. Very weak peaks appeared at 2θ = 26.94º, 33.00º, and 38.59º at a SiO_2 content of 5 wt.%. These peaks are assigned to Li_2SiO_3 that was formed from SiO_2 during annealing at 800ºC. The crystalline and amorphous SiO_2 were not detected by XRD. We prepared the mixture of $LiNO_3$ and SiO_2 powders (Li:Si = 2:1), and fired at 800ºC for 3 h. Most SiO_2 reacted with Li to give the Li_2SiO_3 phase without any appreciable XRD peaks assigned to crystalline SiO_2. Although some impurity peaks appeared, the main product was SiO_2-modified Li_2MnO_3-$LiMn_{1/3}Ni_{1/3}Co_{1/3}O_2$.

SEM images of as-synthesized and calcined Li_2MnO_3-$LiMn_{1/3}Ni_{1/3}Co_{1/3}O_2$ without SiO_2 are shown in Fig. 2-3. The as-synthesized particles were not agglomerated and had a spherical shape. Their diameter was distributed in the range of 100 nm to 2 μm. The surface of the particles consists of finely-dispersed primary particles of a diameter smaller than 100 nm. After heat-treatment, the particles retained their shape; however, the primary particles on the surface became larger than those of the as-synthesized powder. The interior microstructures of the as-synthesized and the calcined Li_2MnO_3-$LiMn_{1/3}Ni_{1/3}Co_{1/3}O_2$ particles are shown in Figs. 2-3(b) and (d), respectively. Before heat-treatment, the interior of the Li_2MnO_3-$LiMn_{1/3}Ni_{1/3}Co_{1/3}O_2$ particle consisted of finely-dispersed primary particles as was observed on the surface (Fig. 2-3(a)). After heat treatment, however, the grain growth progressed significantly at the surface of the secondary particles. Bigger particles (1-2 μm) had a hollow structure with a relatively dense shell with a thickness of 0.3 μm and aggregates of smaller primary particles in the interior. On the other hand, smaller particles of less than 1 μm in diameter were almost completely solidified.

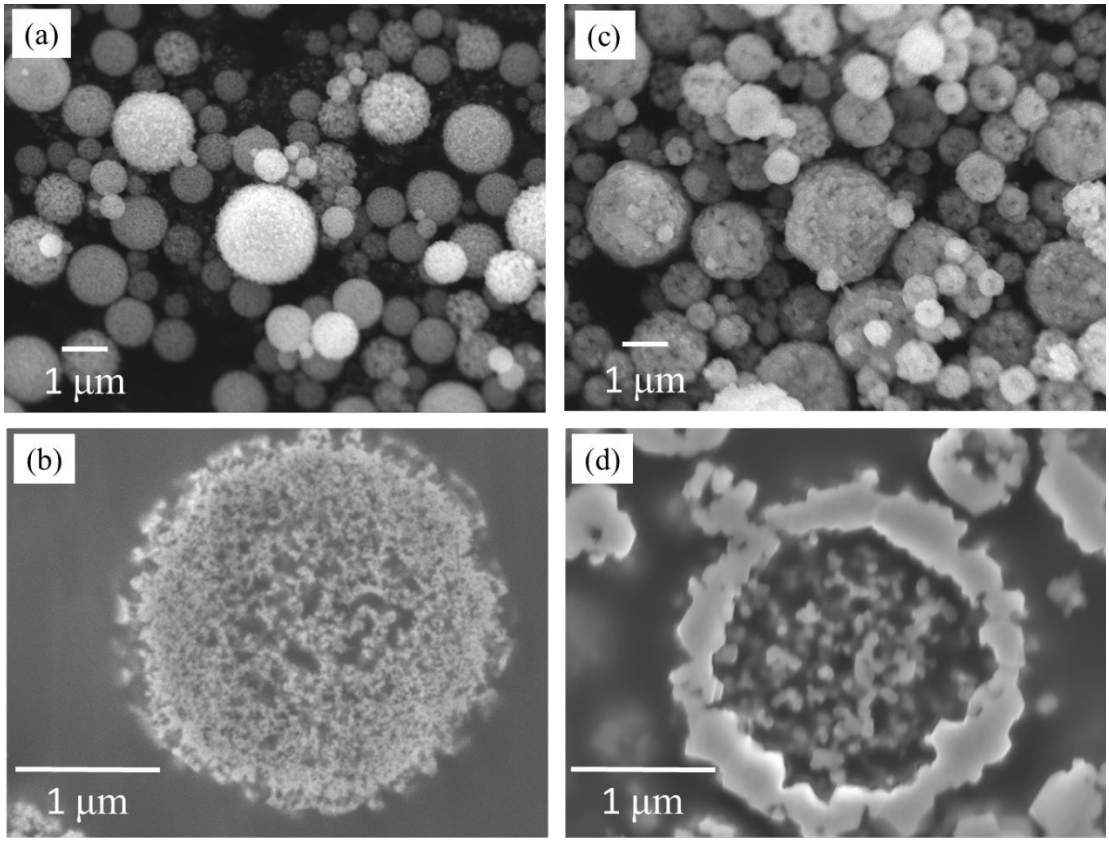

Fig. 2-3 SEM images of unmodified Li_2MnO_3-$LiMn_{1/3}Ni_{1/3}Co_{1/3}O_2$ particles. (a, b) as-synthesized and (c, d) after calcined at 800ºC for 3 h.

Fig. 2-4 show SEM images of 2 and 5 wt.% SiO_2-modified samples after heat-treatment at 800ºC. The interior primary particles were more agglomerated than those of the unmodified particles (Fig. 2-3(d). The size of the secondary particle was not appreciably changed by the addition of SiO_2 aerosol. The specific surface area of 0, 1, 2 and 5 wt.% SiO_2-modified samples were 3.44, 3.56, 3.04, and 4.70 $m^2\ g^{-1}$ respectively. The specific surface area of the unmodified sample was almost the same as that of the 1 wt.% SiO_2-modified sample. However, the specific surface area slightly decreased with

SiO_2 content to 2 wt.%. Here SiO_2 may have worked as a sintering agent before changing to Li_2SiO_3. It has been widely recognized that the reduction in surface area improves the stability of cathode oxide materials such as spinel $LiMn_2O_4$ [4, 28]. The specific surface area increased at a SiO_2 content of 5 wt.% and this may be due to the collapsed shape compared with those of other SiO_2 contents. Lengyel et al. reported that the major factor to determine the secondary particle size in spray pyrolysis is the oscillation frequency for atomization [20]. Moreover, the spherical shape was partially collapsed by SiO_2 modification. The droplet-to-particle conversion process in spray pyrolysis consists of some complicated transport phenomena such as drying, thermal decomposition, and sintering. The particle morphology is mainly determined by the evaporation rate of the solvent on drying. By the addition of SiO_2 aerosol, the solvent molecules may have evaporated heterogeneously from the surface of the atomized droplets. This may be a reason why the SiO_2-modified particles were slightly collapsed.

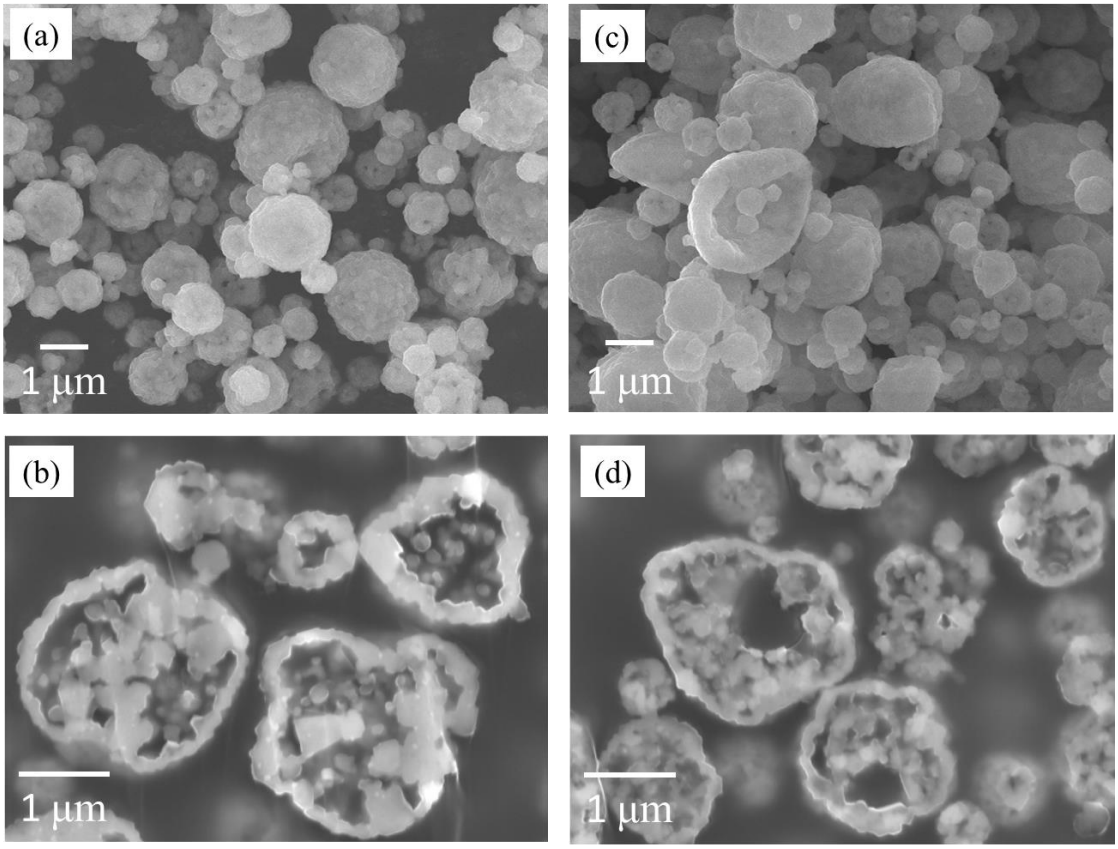

Fig. 2-4 SEM image of (a,b) 2 wt.% SiO_2- and (c,d) 5 wt.% SiO_2-modified Li_2MnO_3-$LiMn_{1/3}Ni_{1/3}Co_{1/3}O_2$ particles after calcined at 800ºC for 3 h.

TEM-EDX analysis was performed for the Li_2MnO_3-$LiMn_{1/3}Ni_{1/3}Co_{1/3}O_2$ modified with 2 wt.% SiO_2 to evaluate the elementary distribution of Mn, Ni, Co and Si inside the particle (Fig. 2-5). The distributions of Mn, Ni, Co were uniform throughout the powder as shown in Figs. 2-5(a)-(c), while the distribution of Si is not uniform as shown in Fig. 2-5(e). The largest size of the Si regions was about 50 nm, which was larger than the original size of SiO_2 aerosol (10-15 nm). The signal of Si indicates that Si-rich regions were seen on the primary particles, but not in the particles. The line profiles of Mn, Ni,

Co and Si are shown in Fig. 2-5(f). The profiles of Si and the transition metals did not coincide with each other. It seemed that SiO_2 did not cover the surface of the primary particles, but were dispersed between the primary particles.

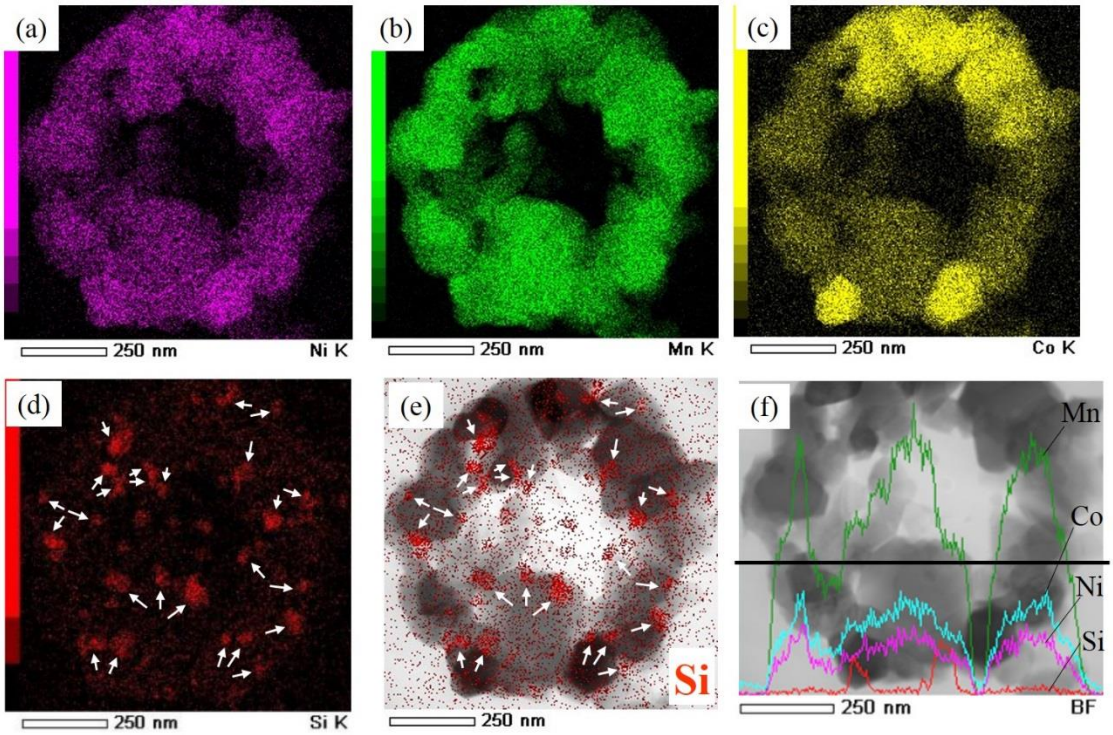

Fig. 2-5 TEM-EDX elemental maps for (a) Ni, (b) Mn, (c) Co, (d, e) Si in 2 wt.% SiO_2-modified Li_2MnO_3-$LiMn_{1/3}Ni_{1/3}Co_{1/3}O_2$ particle after calcined at 800ºC for 3 h, and (f) line profile for Ni, Mn, Co, and Si. TEM images are superposed in (e) and (f). Arrows indicate SiO_2 particles.

2.3.2 Charge and discharge properties

Fig. 2-6 compares the 1st, 10th, and 50th cycle charge-discharge profiles for the unmodified and the SiO_2-modified Li_2MnO_3-$LiMn_{1/3}Ni_{1/3}Co_{1/3}O_2$ samples after the stepwise pre-cycling treatment. All samples delivered discharge capacities higher than 220 mAh g^{-1} after activation at ca. 4.8 V on charging (in the pre-cycling treatment) which is inherent to the lithium-rich layered transition-metal oxide cathodes. The unmodified sample gave an initial discharge capacity of 248 mAh g^{-1}. The 1, 2, and 5 wt.% SiO_2-modified samples exhibited initial discharge capacities of 245, 237, and 228 mAh g^{-1}, respectively. The 1 wt.% modified sample showed a discharge capacity very close to the pristine sample considering the weight ratio of Li_2MnO_3-$LiMn_{1/3}Ni_{1/3}Co_{1/3}O_2$ (i.e., 99%). However, the 5 wt.% modified sample exhibited a slightly lower discharge capacity than the pristine samples (236 mAh g^{-1} for 95 wt.%). In this sample, the presence of Li_2SiO_3 was confirmed on the XRD pattern (Fig. 2-2), and part of Li ions in Li_2MnO_3-$LiMn_{1/3}Ni_{1/3}Co_{1/3}O_2$ was consumed to form Li_2SiO_3 by the addition of SiO_2. Therefore, the discharge capacity may have decreased with increasing SiO_2 content.

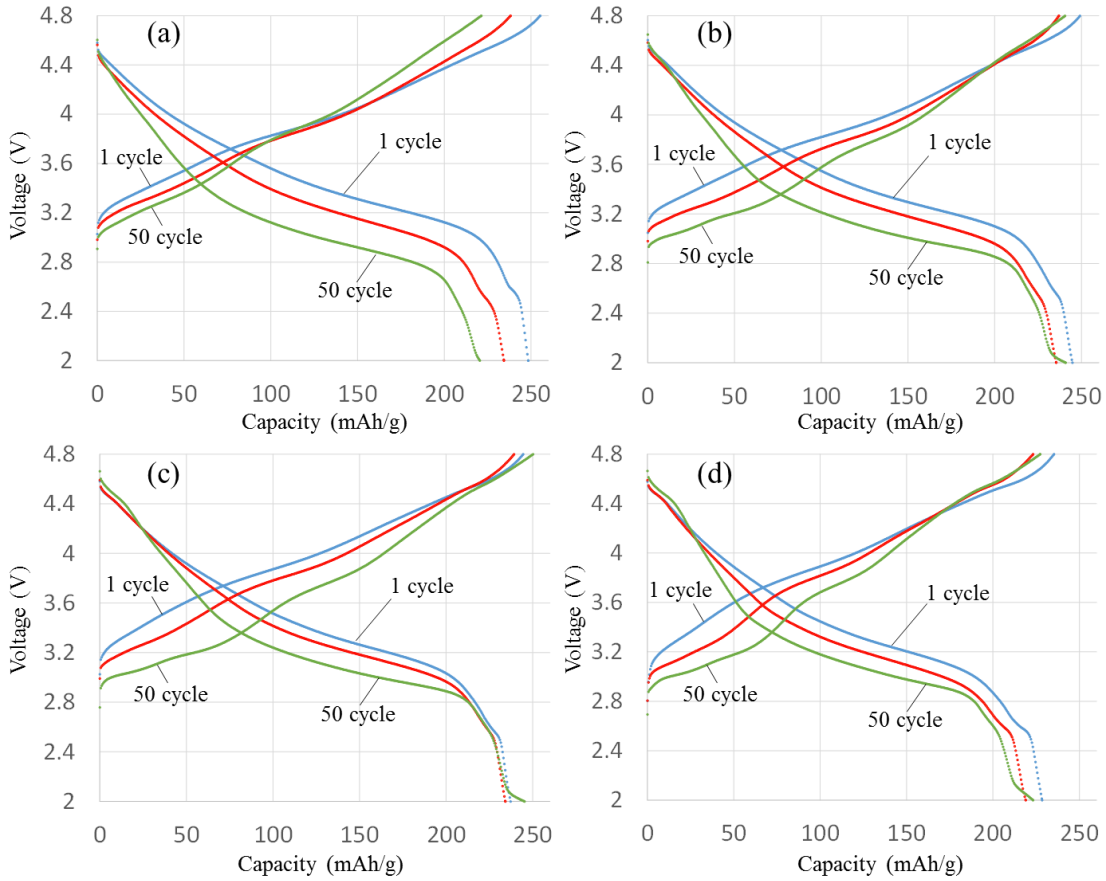

Fig. 2-6 Charge and discharge curves of Li_2MnO_3-$LiMn_{1/3}Ni_{1/3}Co_{1/3}O_2$ cathodes modified with (a) 0, (b) 1, (c) 2, and (d) 5 wt.% of SiO_2 in 1 M $LiPF_6$/EC+DMC (1:1) at 0.1 C and 30ºC.

The discharge capacity of the unmodified sample declined rapidly. The capacity retention was improved by SiO_2 modification. For the SiO_2-modified samples, a new plateau appeared at ca. 2 V on the discharge curve at the 50th cycle. Appearance of a similar plateau at ca. 2 V was reported for Li-rich layered manganese oxide cathodes operated between 2.0 to 5.0 V for 20 cycles [29]. The mechanism for the 2-V plateau and

its effect on cycleability are not clear at present. It should be noted that even if the capacity at the 2-V plateau is ignored, the capacity retention is improved for SiO_2-modified samples. Fig. 2-7 shows the variations of capacity retention for unmodified and SiO_2-modified samples. Here we plotted the discharge capacities between 4.8 and 2.1 V to ignore the capacity for the 2-V plateau in Fig. 2-6. The capacity of the unmodified sample gradually decreased on cycling. On the other hand, the capacity fade on cycling was successfully suppressed for all SiO_2-modified samples. The highest capacity retention was obtained for the 2 wt.% SiO_2-modified sample.

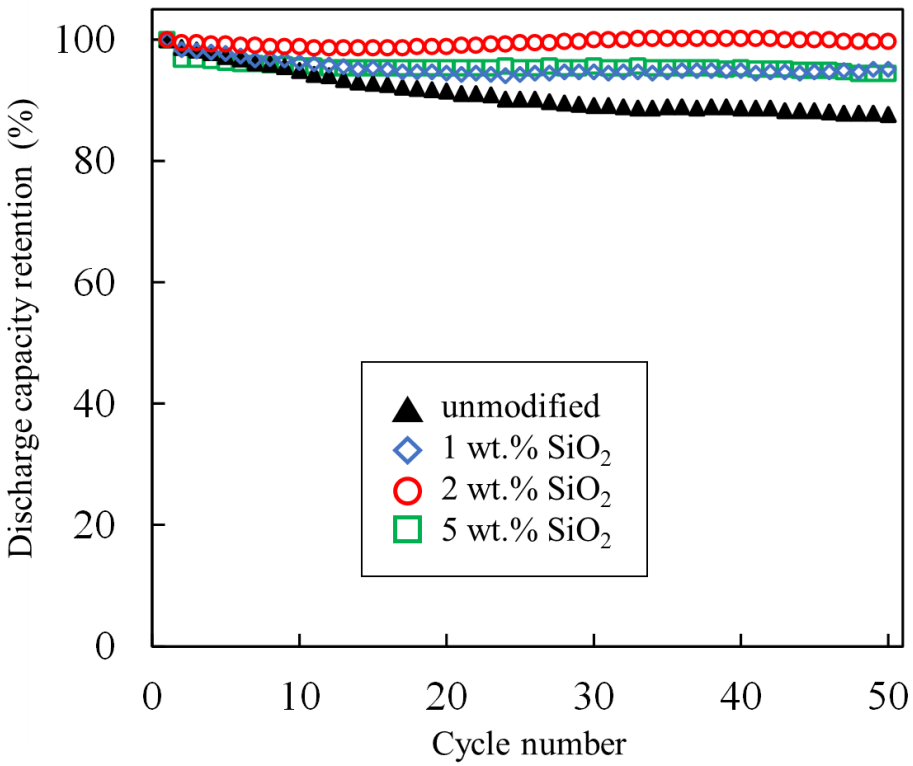

Fig. 2-7 Variations of discharge capacity retention of Li_2MnO_3-$LiMn_{1/3}Ni_{1/3}Co_{1/3}O_2$ cathodes unmodified and modified with 1, 2, and 5 wt.% of SiO_2 in 1 M $LiPF_6$/EC+DMC (1:1) at 0.1 C and 30ºC. The discharge capacities between 4.8 and 2.1 V were plotted to ignore the capacity for the 2 V plateau in Fig. 2-6.

A close inspection in Fig. 2-6 revealed that voltage depression was observed on the discharge curve after cycling for each sample, which is another problem for the Li-excess layered oxides called “voltage fade” [24]. However, the voltage fade was clearly improved by SiO_2 modification. The average discharge voltages at the 1st and 50th cycles were calculated, and are summarized in Table 2-1. An excess amount of insulating SiO_2 causes an increase in electrical resistivity, and hence the average discharge voltage at the 1st cycle (V_{D1}) of the 5 wt.% modified sample was slightly lower than that of the pristine sample. On the other hand, the average discharge voltages at the 50th cycle (V_{D50}) of the SiO_2-modified samples were higher than that of the unmodified sample. As a result, the voltage fade during 50 cycles (V_{D1}-V_{D50}) decreased with increasing SiO_2 content, though it was not completely mitigated by SiO_2 addition. Gallagher et al. reported that irreversible migration of the transition metal ions, which does not lead to the arrangement of a perfect spinel structure, results in the voltage fade [7]. Taking the morphology and the crystal structure of the SiO_2-modified samples into account, we note the possibility of lowering the migration of the transition metal ions during charge and discharge because of the presence of the SiO_2 (or Li_2SiO_3) on the primary particles.

Table 2-1 Average discharge voltages of unmodified and SiO_2-modified Li_2MnO_3-$LiMn_{1/3}Ni_{1/3}Co_{1/3}O_2$.

Amount of SiO_2 (wt.%)	V_{D1}:Ave. discharge voltage in 1st cycle (V)	V_{D50}:Ave. discharge voltage in 50th cycle (V)	V_{D1}-V_{D50} (V)
0	3.48	3.20	0.28
1	3.48	3.23	0.25
2	3.47	3.26	0.21
5	3.43	3.25	0.18

2.3.3 Mechanisms for performance improvements

As indicated by the TEM-EDX analysis in Fig. 2-5, SiO_2 was not included in the primary particles, but was present on the primary particles. The SiO_2 (or Li_2SiO_3) particles partially covered the surface of active material particles and prevented the active material surface from direct contact with the electrolyte. Therefore one of the reasons for the observed positive effects of SiO_2 modification is that SiO_2 particles partly suppress electrolyte decomposition and the dissolution of the metal ions from the layered structure into the electrolyte.

Borong et al. reported that the capacity fade of $LiNi_{0.5}Mn_{1.5}O_4$ electrode was suppressed when the electrolyte containing Li_2SiO_3 is reduced [30]. They concluded that Mn dissolution and PF_5-initiated solvent polymerization were mitigated because HF and PF_5 were consumed by Li_2SiO_3 if it precipitated on the cathode surface. In the present study, the suppression of capacity fade may be related to the presence of SiO_2 in the secondary particles. Fig. 2-8 shows the variations of dissolved Mn ions at 60ºC with the amount of modified SiO_2. It is clear that the dissolution of Mn ions were remarkably suppressed by SiO_2 modification, especially at 2 and 5 wt.%. One reason is clear because the presence of SiO_2 enhanced the growth of the interior primary particles, which resulted in a reduced surface area. Another reason may be related to the fact that modified SiO_2 particles consumed HF and PF_5 that accelerate Mn dissolution as mentioned above. This suppressed the capacity and voltage fade, and improved the cycle performance of Li_2MnO_3-$LiMn_{1/3}Ni_{1/3}Co_{1/3}O_2$, though further investigation is needed in the future.

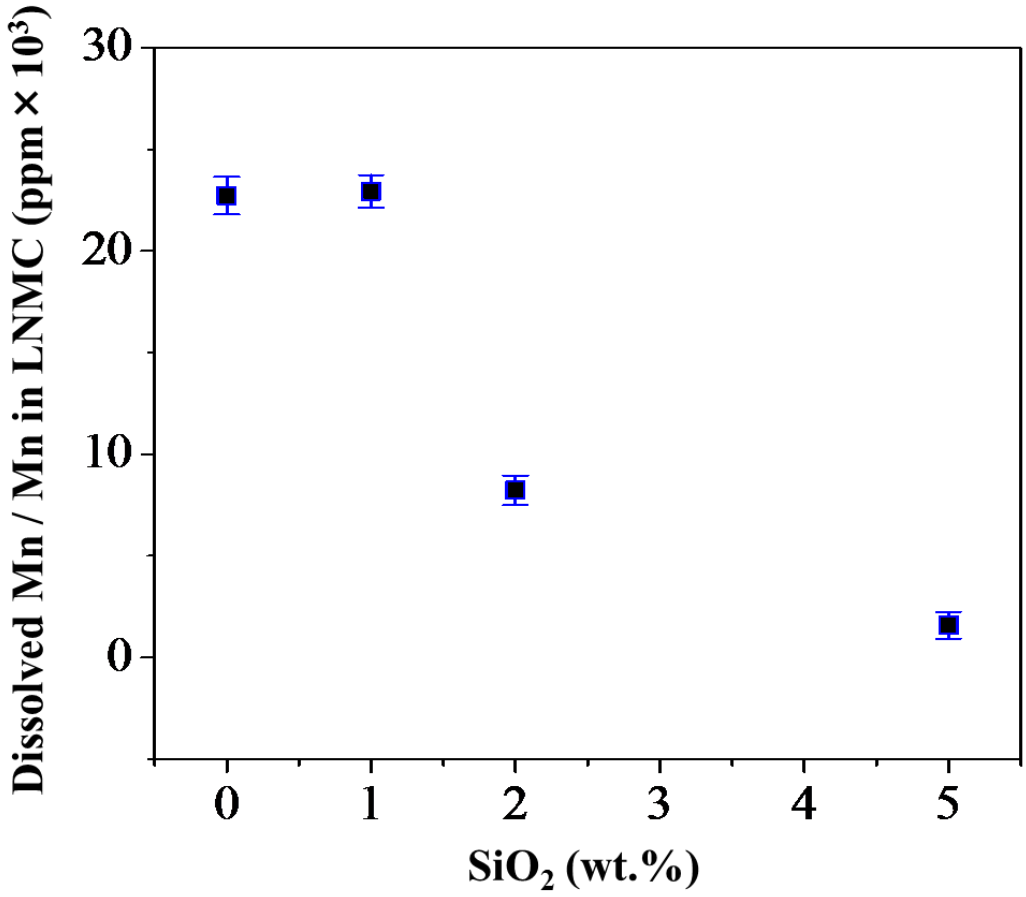

Fig. 2-8 Amounts of dissolved Mn ions from Li_2MnO_3-$LiMn_{1/3}Ni_{1/3}Co_{1/3}O_2$ cathodes unmodified and modified with 1, 2, and 5 wt.% of SiO_2 in 1 M $LiPF_6$/EC+DMC (1:1) under the open-circuit conditions at 60ºC for after charged to 4.8 V. The amount of dissolved Mn ions is normalized by the total Mn ions contained in each sample before the test.

2.4 Conclusions

SiO_2 modified layered Li_2MnO_3-$LiMn_{1/3}Ni_{1/3}Co_{1/3}O_2$ particles were prepared by spray pyrolysis and their charge and discharge characteristics as cathodes in lithium-ion batteries were investigated. SiO_2 modification effectively suppressed not only capacity fade, but also voltage fade. ICP measurements showed that Mn dissolution at an elevated temperature was suppressed by SiO_2 addition. SEM analysis revealed that the addition of SiO_2 enhanced the sintering of the primary particles in the spherical secondary particles, while TEM-EDX analysis indicated that SiO_2 particles were not included inside the primary particles, but on the surface of the primary particles. These results demonstrate that SiO_2 modification is an effective way for suppressing the reaction of Mn dissolution and improving the cycle performance of lithium-excess layered lithium manganese oxide cathodes.

References

[1] J. Zheng, S. Deng, Z. Shi, H. Xu, H. Xu, Y. Deng, Z. Zhang, G. Chen, J. Power Sources 221, 108 (2013).

[2] J. Li, R. Klopsch, M. C. Stan, S. Nowak, M. Kunze, M. Winter, S. Passerini, J. Power Sources 196, 4821 (2011).

[3] S. Kaneko, B. Xia, Q. Zhang, G. Fang, W. Liu, H. Sun, F. Matsumoto, Y. Sato, J. Zheng, D. Li, Electrochemistry 82, 438 (2014).

[4] X. Guo, Y. Li, M. Zheng, J. Zheng, J. Li, Z. Gong, Y. Yang, J. Power Sources 184, 414 (2008).

[5] C. S. Johnson, N. Li, C. Lefief, M. M. Thackeray, Electrochem. Commun. 9, 787 (2007).

[6] J. R. Croy, K. G. Gallagher, M. Balasubramanian, Z. Chen, Y. Ren, D. Kim, S. Kang, D. W. Dees, M. Thackeray, J. Phys. Chem. C 117, 6525 (2013).

[7] K. G. Gallagher, J. R. Croy, M. Balasubramanian, M. Bettge, D. P. Abraham, A. K. Burrell, M. M. Thackeray, Electrochem. Commun. 33, 96 (2013).

[8] D. Arumugam, G. P. Kalaignan, J. Electroanal. Chem. 624, 197 (2008).

[9] Y. Fan , J. Wang, Z. Tang, W. He, J. Zhang, Electrochim. Acta 52, 3870 (2007).

[10] W. He, D. Yuan, J. Qian, X. Ai, H. Yang, Y. Cao, J. Mater. Chem. 1, 11397 (2013).

[11] H. Kobayashi, T. Okumura, M. Shikano, K. Takada, Y. Arachi, H. Nitani, Solid State Ionics 262, 43 (2014).

[12] J. Zhao, G. Qu, J. C. Flake, Y. Wang, Chem. Commun. 48, 8108 (2012).

[13] L. Yu, X. Qiu, J. Xi, W. Zhu, L. Chen, Electrochim. Acta 51, 6406 (2006).

[14] J. S. Chae, S. B. Yoon, W. S. Yoon, Y. M. Kang, S. M. Park, J. W. Lee, K. C. Roh, J.

Alloys Comp. 601, 217 (2014).

[15] I. Taniguchi, C. K. Lim, D. Song, M. Wakihara, Solid State Ionics 146, 239 (2002).

[16] B. Ebin, S. Gurmen, C. Arslan, G. Lindbergh, Electrochim. Acta 76, 368 (2012).

[17] H. Yoshida, H. Deguchi, M. Kawano, K. Hashino, T. Inagaki, H. Ijichi, M. Horiuchi, K. Kawahara, S. Suda, Solid State Ionics 178, 399 (2007).

[18] M. Kawano, H. Yoshida, K. Hashino, H. Ijichi, S. Suda, K. Kawahara, T. Inagaki, J. Power Sources 173, 45 (2007).

[19] S. Hashigami, H. Yoshida, D. Ueno, M. Kawano, T. Inagaki, J. Power Sources 248, 190 (2014).

[20] M. Lengyel, G. Atla, D. Elhassid, P. Y. Luo, X. Zhang, I. Belharouak, R. L. Axelbaum, J. Power Sources 262, 286 (2014).

[21] M. Y. Son, Y. J. Hong, S. H. Choi, Y. C. Kang, Electrochim. Acta 103, 110 (2013).

[22] Y. J. Hong, S. H. Choi, C. M. Sim, J.K. Lee, Y. C. Kang, Mater. Res. Bull. 47, 4359 (2012).

[23] C. Li, H. P. Zhang, L. J. Fu, H. Liu, Y. P. Wu, E. Rahm, R. Holze, H. Q. Wu, Electrochim. Acta 51, 3872 (2006).

[24] A. Ito, D. Li, Y. Ohsawa, Y. Sato, J. Power Sources 183, 344 (2008).

[25] T. Ohzuku, A. Ueda, M. Nagayama, Y. Iwakoshi, H. Komori, Electrochim. Acta 38, 1159 (1993).

[26] C. S. Johnson, N. Li, C. Lefief, J. T. Vaughey, M. M. Thackeray, Chem. Mater. 20, 6095 (2008).

[27] S. H. Kang, C. S. Johnson, J. T. Vaughey, K. Amine, M. M. Thackeray, J. Electrochem. Soc. 153, A1186 (2006).

[28] Y. Xia, N. Kumada, M. Yoshio, J. Power Sources 90, 135 (2000).

[29] T. Ohzuku, M. Nagayama, K. Tsuji, K. Ariyoshi, J. Mater. Chem. 21, 10179 (2011).

[30] B. Wu, Y. Ren, D. Mu, X. Liu, F. Wu, Electrochim. Acta 143, 324 (2014).

CHAPTER 3

Synthesis of SiO_2-modified Li_2MnO_3-$LiMn_{1/3}Ni_{1/3}Co_{1/3}O_2$ by Spray Pyrolysis with Acid Addition as Cathode Materials for Lithium-ion Batteries

3.1 Introduction

Lithium-rich layered solid solutions of Li_2MnO_3 and $LiMO_2$, where *M* denotes at least one 3d transition metal, has attracted much attention as a cathode material of lithium ion batteries because they offer high capacities of around 250 mAh g^{-1} within the potential range of 2.0 to 4.8 V (versus Li/Li^+) [1-4]. However, most of the works on the material have reported the electrochemical performance at low current rates, because of its intrinsically poor rate-capability. Designing the powder morphologies of the materials is particularly important for improving the cell performance [5, 6].

Spray pyrolysis is a simple one-step synthesis technique to obtain various kinds of functional oxide powders. The particles prepared by spray pyrolysis have some advantages such as small particle size distribution, high purity, and easy control in composition and morphology of multi-component metal oxides [7]. In addition, powder morphology can be controlled by acid addition to the starting solution of spray pyrolysis [8]. It was found in Chapter 2 that the addition of a small amount of SiO_2 remarkably suppressed the capacity fade of Li_2MnO_3-$LiMn_{1/3}Ni_{1/3}Co_{1/3}O_2$ prepared by spray pyrolysis during charge and discharge cycling [9]. In Chapter 3, the effect of acid addition

to the starting solutions of the SiO_2-modified Li_2MnO_3-$LiMn_{1/3}Ni_{1/3}Co_{1/3}O_2$ of spray pyrolysis was investigated. The properties of the synthesize particles and the rate capabilities using these particles as the cathode were discussed.

3.2 Experimental

3.2.1. Preparation of the cathode materials by spray pyrolysis

Stoichiometric amounts of lithium nitrate (99.9%, Wako Pure Chemical Industries, Ltd.), manganese nitrate hexahydrate (99.9%, Wako Pure Chemical Industries, Ltd.), nickel nitrate hexahydrate (99.9%, Wako Pure Chemical Industries, Ltd.), cobalt nitrate hexahydrate (99.0%, Wako Pure Chemical Industries, Ltd.) were weighed to prepare 0.2 mol of Li_2MnO_3-$LiMn_{1/3}Ni_{1/3}Co_{1/3}O_2$, and were dissolved in 500 mL of deionized water. SiO_2 sol (Nissan Chemical Ltd., ST-O type) was added to the solution at a weight ratio of Li_2MnO_3-$LiMn_{1/3}Ni_{1/3}Co_{1/3}O_2$: SiO_2 = 98 : 2. Citric acid (Wako Pure Chemical Industries, Ltd.) or boric acid (Wako Pure Chemical Industries, Ltd.) was also added to the starting solution. Citric acid was added by 0.2, 0.4, 0.5 times of the total mols of Li^+, Mn^{2+}, Co^{2+} and Ni^{2+} cations in the solution. Boric acid was added to the solution at a weight ratio of Li_2MnO_3-$LiMn_{1/3}Ni_{1/3}Co_{1/3}O_2$: H_3BO_3 = 99.9 : 0.1, 99.7 : 0.3, or 99.5 : 0.5. The solution was stirred for an hour, diluted with deionized water to 1 L, and was used for spray pyrolysis.

Li_2MnO_3-$LiMn_{1/3}Ni_{1/3}Co_{1/3}O_2$ particles modified with SiO_2 were synthesized with a spray pyrolysis apparatus described in Chapter 2 [10]. The solution was atomized using ultrasonic vibrators with an oscillation frequency of 1.65 MHz in an atomizing vessel. Because the ultrasonic vibrators raise the temperature of the solution during atomizing, cold water was circulated around the atomizing vessel to keep the temperature of the solutions lower than 30 ºC. This is because atomization at high temperatures tends to give inhomogeneous droplets. The reaction furnace consisted of four independent heating

zones, whose temperatures were set at 200, 400, 800, and 800 ºC from the inlet to the outlet. The atomized mists were flown into the furnace with 1 L min^{-1} of air as a carrier gas. The droplets including Li^{+}, Mn^{2+}, Co^{2+}, Ni^{2+} and SiO_2 were dried, decomposed, reacted, and sintered when passing through the reaction furnace. The powders were collected using a membrane filter, and were heat-treated at 800 ºC for 3 h in air. We denoted the synthesized Li_2MnO_3-$LiMn_{1/3}Ni_{1/3}Co_{1/3}O_2$ particles as LNMC, SiO_2-modified ones as S-LNMC, SiO_2-modified ones prepared from the starting solutions containing citric acid and boric acid such as C-S-LNMC (0.4 times) and B-S-LNMC (0.3 wt.%), respectively.

3.2.2. Cell fabrication and charge/discharge tests

A cathode slurry was prepared by mixing the sample powders (80 wt.%), an acetylene black conductor (Denka Co., Ltd., 10 wt.%), a polyvinylidene fluoride binder (Kureha Corp., 10 wt.%) using 1-methyl-2-pyrrolidinone (Wako Pure Chemical Industries, Ltd.) as a solvent. The slurry was coated on an Al foil current collector (20 μm thickness), and dried at 120 ºC for 24 h under vacuum. The loading of the cathode was typically 1.5 mg cm^{-2}.

Charge and discharge tests were carried out using two-electrode coin-type cells, which were assembled in an Ar-filled glove box (Miwa, MDB-1NKP-DS). Li metal foil (Honjo Metal) was used as a counter electrode, and a micro-porous monolayer membrane (Celgard®2400) was used as a separator. The electrolyte solution was 1 M $LiPF_6$ dissolved in a 1:1 (by volume) mixture of ethylene carbonate (EC) and dimethylcarbonate (DMC). The charge and discharge tests were performed galvanostatically between 2.0 and 4.8 V

at 30 ºC using a BTS2004W-10 battery test system (Nagano Co. Ltd.). For the rate capability tests the current increased stepwisely from 0.1 to 1 C (1 C = 314 mAh g^{-1}) for five cycles each. Prior to the charge and discharge tests, a stepwise pre-cycling treatment was carried out by increasing the upper potential limit by 0.1 V from 4.5 V every two cycles to 4.8 V according to the procedure proposed by Ito et al. [11].

3.2.3. Powder characterization

The morphology of the synthesized LNMC powders was observed with a scanning electron microscope (SEM, TM-3000) and a transmission electron microscope (TEM, JEM-2100F) equipped with an energy dispersive X-ray spectroscopy (EDX). The oxide particles were embedded in a polymer resin, and samples for TEM observation were prepared by a cross-section polisher (JEOL, SM-09010DM) and a focused ion beam system (Hitachi, FB2000A). The crystal structures of the synthesized LNMC powders were investigated by X-ray diffraction (XRD, Rigaku Smartlab) using Cu Kα radiation. The BET surface area of the powders was measured with a Belsorp mini.

3.3 Results and Discussion

Fig. 3-1 shows SEM images of LNMC, S-LNMC, and C-S-LNMC. Both LNMC and S-LNMC had spherical shapes and were not aggregated. It seemed that the particle shape and size were not strongly affected by SiO_2 modification. Fig. 3-1 (c) shows a SEM image of C-S-LNMC (0.4 times). The addition of a small amount of citric acid (C-S-LNMC (0.2 times)) did not change the morphology, but further addition of citric acid changed the morphology as shown in Figs. 3-1(c) and (d). C-S-LNMC (0.4 times) had spherical shapes, but the particle walls seemed to be much thinner. C-S-LNMC (0.5 times) particles were partially collapsed spheres with thin walls.

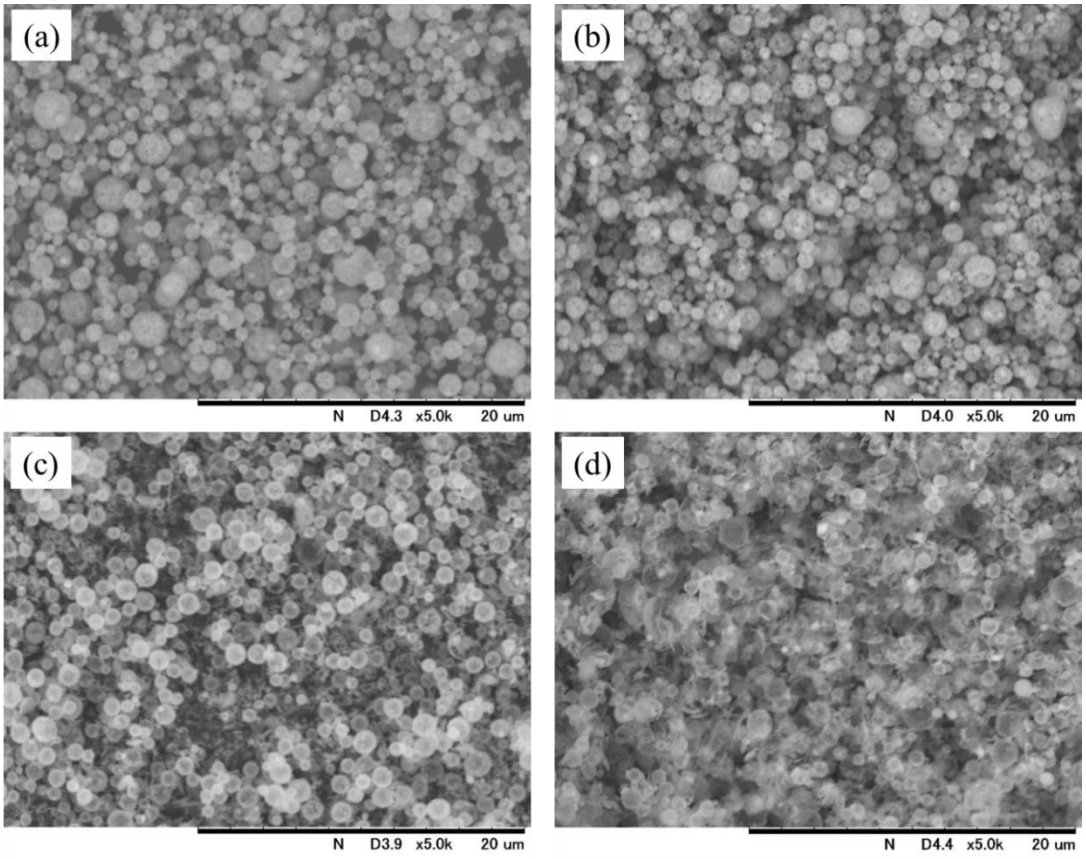

Fig. 3-1 SEM images of (a) LNMC, (b) S-LNMC, (c) C-S-LNMC (0.4 times) and (d) C-S-LNMC (0.5 times).

TEM image and the distribution of nickel, manganese, cobalt, and silica inside the C-S-LNMC (0.4 times) are shown in Fig. 3-2. The addition of citric acid to the spray solution increased the hollowness of the powders. It was confirmed that the powders had a thin walled structure. The primary particles in C-S-LNMC (0.4 times) were smaller than those of S-LNMC, and the distributions of Mn, Ni, and Co were uniform throughout the powder. Citric acid works as a chelating agent, and decreases the solubility of transition metal ions in the solution. Hence the metal salts precipitated at the liquid droplet surface at lower temperatures near the inlet and formed the hollow particles with thin walls before the droplets were shrunk by the evaporation of water. The small primary particles and uniform distributions of transition metal ions are also due to the chelation by citric acid. On the other hand, the distribution of Si is not uniform and the largest size of the Si regions was about 50 nm, which was the same as S-LNMC without citric acid. It is considered that the SiO_2 particles effectively suppress electrolyte decomposition and the dissolution of the metal ions from the layered structure into the electrolyte as was observed for S-LNMC in Chapter 2.

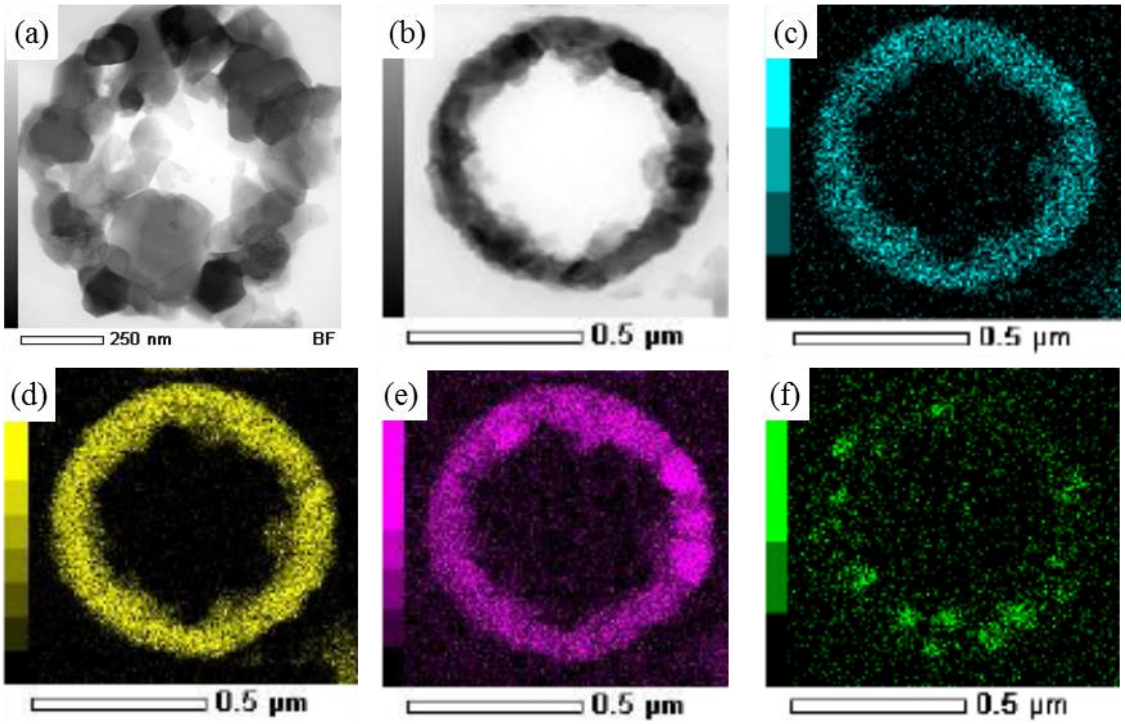

Fig. 3-2 TEM image showing the interior morphology of (a) S-LNMC and (b) C-S-LNMC (0.4 times), and TEM-EDX elemental maps for (c) Ni, (d) Mn, (e) Co, (f) Si in C-S-LNMC (0.4 times).

Fig 3-3 shows SEM images of B-S-LNMC. Though B-S-LNMC (0.1 wt.%) displayed similar morphologies to S-LNMC, the spherical shape of B-S-LNMC (0.3 wt.%) was partially collapsed due to the cohesion of secondary particles. B-S-LNMC (0.5 wt.%) displayed strongly aggregated structures with large sizes, which indicates that boric acid served as a sintering agent of the cathode powders.

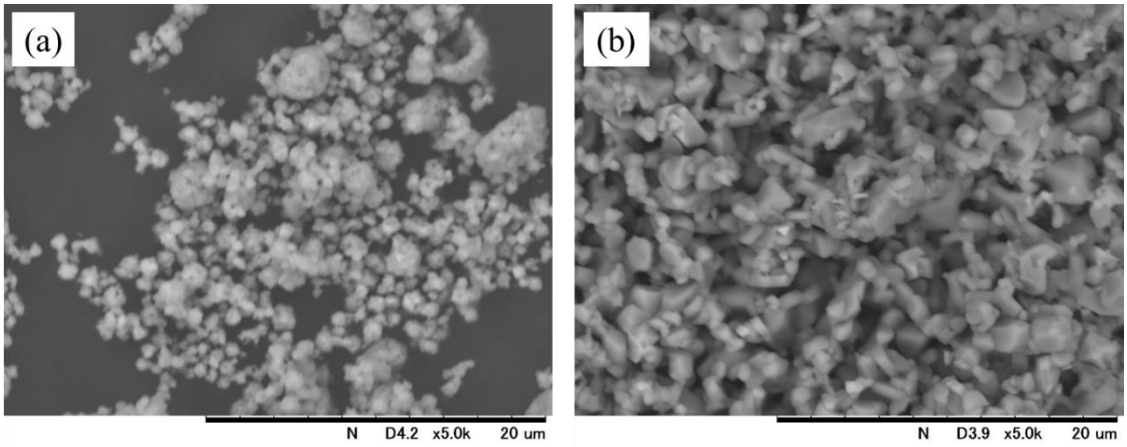

Fig. 3-3 SEM images of (a) B-S-LNMC (0.3 wt.%), and (b) B-S-LNMC (0.5 wt.%).

Table **3-1 shows the specific surface areas of the LNMC powders.** The specific surface area slightly decreased with SiO_2 content at 2 wt.%. Here SiO_2 may have worked as a sintering agent before transforming to Li_2SiO_3. The specific surface area of C-S-LNMC (0.4 times) and (0.5 times) was 4.75 and 6.96 $m^2 g^{-1}$, respectively, which were higher than that of S-LNMC (3.04 $m^2 g^{-1}$). The high specific surface area of C-S-LNMC is expected to enhance the rate capability. On the other hand, the specific surface area of B-S-LNMC (0.3 wt.%) was lower than that of S-LNMC. It is clear that only a few tenths of weight percent of boric acid worked as a sintering agent.

Table 3-1 Specific surface areas of synthesized LNMC powders.

Material	Specific surface area ($m^2 g^{-1}$)
LNMC	3.44
S-LNMC	3.04
C-S-LNMC (0.4 times)	4.75
C-S-LNMC (0.5 times)	6.96
B-S-LNMC (0.3 wt.%)	1.37

Fig 3-4 shows the XRD patterns of LNMC, S-LNMC, C-S-LNMC and B-S-LNMC. The XRD pattern of each sample was typical of the Li_2MnO_3-$LiMn_{1/3}Ni_{1/3}Co_{1/3}O_2$ layered structure because the weak superstructure diffractions appeared at around $2\theta = 22°$, which originates from the ordering between the Li_2MnO_3 and the Li*M*O_2. Very weak peaks appeared at $2\theta = 26.94º$, 33.00º, and 38.59º at a SiO_2 content of 2 wt. % are assigned to Li_2SiO_3 that was formed from SiO_2 during annealing at 800 ºC. Some impurity peaks appeared at 31.1° and 36.6°, which is assigned to the spinel LiM_2O_4 phase such as $LiNi_{0.3}Co_{0.4}Mn_{1.3}O_4$ and $LiNi_{0.2}Co_{0.6}Mn_{1.2}O_4$. The XRD patterns of C-S-LNMC were similar to that of S-LNMC. No diffraction peaks corresponding to the boron-related phases were seen for B-S-LNMC. This is due to a small quantity and amorphous nature of boron compounds. The peaks near 21.77° were attributed to the structure of Li_2MnO_3.

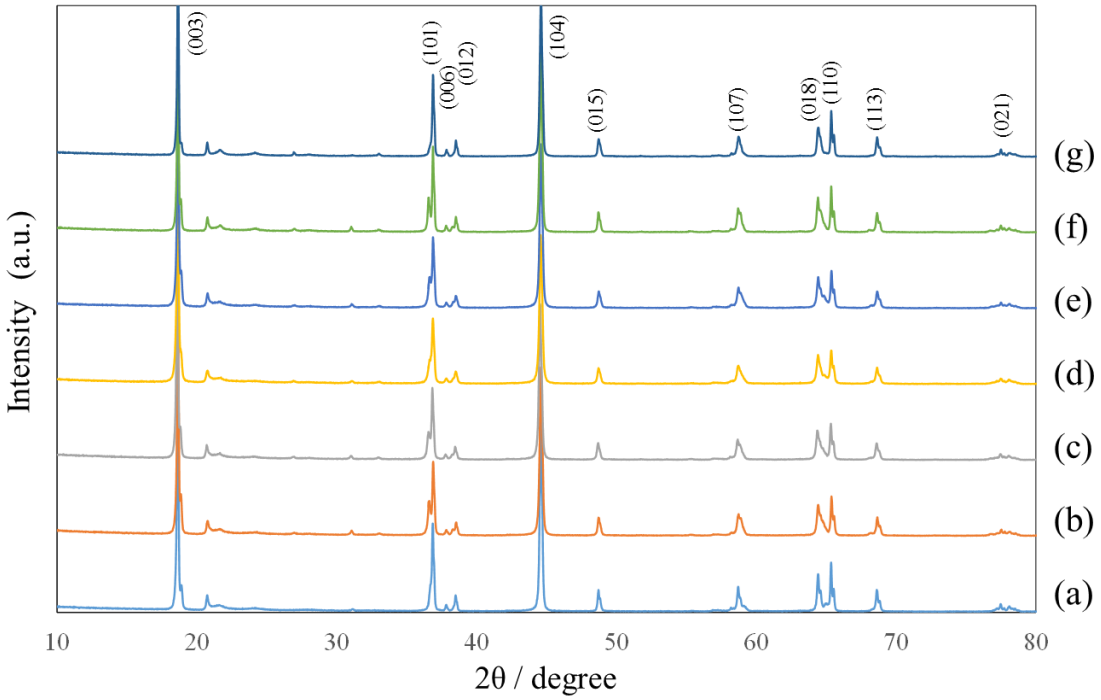

Fig. 3-4 X-ray diffraction patterns of (a) LNMC, (b) S-LNMC, (c) C-S-LNMC (0.2 times), (d) C-S-LNMC (0.4 times), (e) C-S-LNMC (0.5 times), (f) B-S-LNMC (0.1 wt.%), and (g) B-S-LNMC (0.3 wt.%).

The charge and discharge curves at various rates for LNMC, S-LNMC, C-S-LNMC, and B-S-LNMC are shown in Fig 3-5. SiO_2-modified Li_2MnO_3-$LiMn_{1/3}Ni_{1/3}Co_{1/3}O_2$ showed improved capacity retention at any rate (0.1, 0.2, 0.5, and 1 C) when compared with that of the unmodified sample. The addition of citric acid enhanced the capacity of S-LNMC at each rate. C-S-LNMC (0.4 times) delivered a higher discharge capacity (178-181 mAh g^{-1}) even at a high rate of 1 C (314 mA g^{-1}). The cycleability of the material was not inferior to that of S-LNMC, indicating that the addition of citric acid did not have a harmful effect on the cycleability. This result confirmed that the high specific surface area

obtained by spray pyrolysis using citric acid improves the rate-capability without sacrificing the cycleability. However, C-S-LNMC (0.5 times) showed a lower discharge capacity and poorer capacity retention especially at higher rates although it showed a relatively high discharge capacity (240 mAh g^{-1}) at 0.1 C. The collapsed particles (Fig. 3-1(d)) may have led to the deterioration of rate capability because the electrical path was insufficient. The addition of boric acid deteriorated the rate capability of B-S-LNMC. This may be due to the reduced specific surface area (Table 3-1) and the presence of a glass layer formed from the Li and B components.

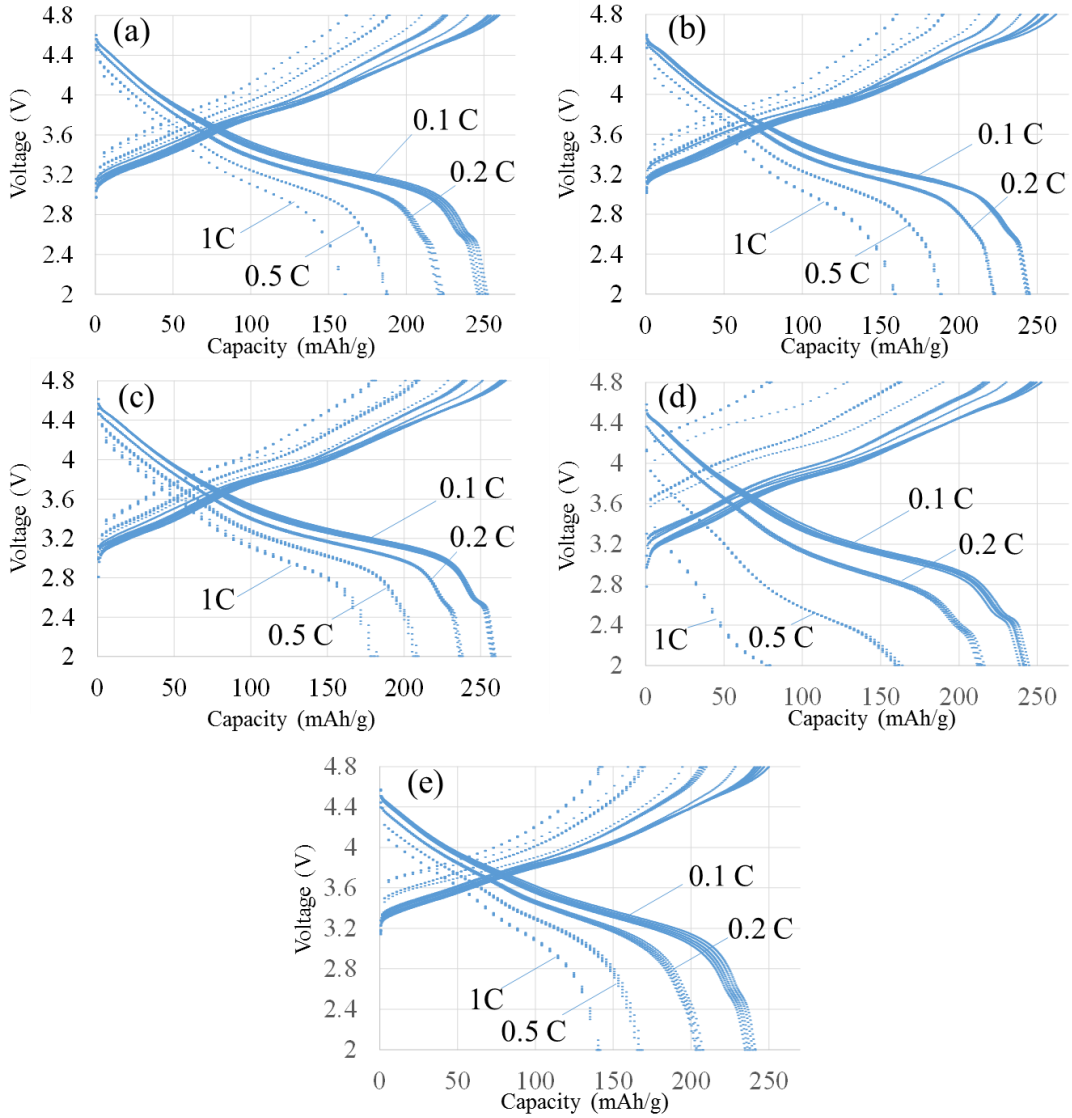

Fig. 3-5 Charge-discharge curves of (a) LNMC, (b) S-LNMC, (c) C-S-LNMC (0.4 times), (d) C-S-LNMC (0.5 times), and (e) B-S-LNMC (0.3 wt.%) at 0.1 C, 0.2 C, 0.5 C, and 1C.

The materials exhibiting a high cycleability and rate capability by adding citric acid to the starting solution were synthesized. However, the fade in the average cell voltage was still observed on repeated cycling of the cathode. It is necessary to overcome the voltage fade by further optimizing the synthesis conditions.

3.4 Conclusions

SiO_2-modified LNMC particles were prepared by spray pyrolysis using starting solutions containing citric acid and boric acid, and their charge and discharge characteristics as cathodes in lithium-ion batteries were investigated. The addition of citric acid increased the specific surface area and enhanced the rate capability of SiO_2-modified LNMC; however, an excess amount of citric acid (0.5 times) resulted in the collapsed particles, which showed poor capacity retention. The addition of boric acid deteriorated the rate performance of SiO_2-modified LNMC, which was considered to be due to the reduced specific surface area and the presence of a glass layer formed from the Li and B components. It was confirmed that the highly dispersed particles having a higher specific surface area obtained by spray pyrolysis using citric acid show better performance in both rate-capability and cycleability.

References

[1] J. Zheng, S. Deng, Z. Shi, H. Xu, H. Xu, Y. Deng, Z. Zhang, G. Chen, J. Power Sources 221, 108 (2013).

[2] J. Li, R. Klopsch, M. C. Stan, S. Nowak, M. Kunze, M. Winter, S. Passerini, J. Power Sources 196, 4821 (2011).

[3] T. Ohzuku, M. Nagayama, K. Tsuji, K. Ariyoshi, J. Mater. Chem. 21, 10179 (2011).

[4] X. Guo, Y. Li, M. Zheng, J. Zheng, J. Li, Z. Gong, Y. Yang, J. Power Sources 184, 414 (2008).

[5] S. Kaneko, B. Xia, Q. Zhang, G. Fang, W. Liu, H. Sun, F. Matsumoto, Y. Sato, J. Zheng, D. Li, Electrochemistry 82, 438 (2014).

[6] J. Li et al, J. Power Sources 196, 4821 (2011).

[7] M. Lengyel, G. Atla, D. Elhassid, P. Y. Luo, X. Zhang, I. Belharouak, R. L. Axelbaum, J. Power Sources 262, 286 (2014).

[8] J. R. Sohn, Y. C. Kang, and H. D. Park, Jpn. J. Appl. Phys. 41, 3006 (2002).

[9] S. Hashigami, M. Kawanishi, S. Ujiie, T. Inagaki, M. Hashinokuchi, T. Doi, and M. Inaba, Electrochemistry, 84, 842 (2016).

[10] M. Kawano, H. Yoshida, K. Hashino, H. Ijichi, S. Suda, K. Kawahara, and T. Inagaki, J. Power Sources 173, 45 (2007).

[11] A. Ito, D. Li, Y. Ohsawa, Y. Sato, J. Power Sources 183, 344 (2008).

CHAPTER 4

Durability Improvement of $LiNi_{0.5}Co_{0.2}Mn_{0.3}O_2$ Cathode Coated with Lithium Boron Oxide Glass Prepared by an Antisolvent Precipitation Method

4.1 Introduction

Lithium ion batteries (LIBs) have been so used mainly in small electronic devices. However, the number of applications such as plug-in hybrid vehicles (PHEVs) and electric vehicles (EVs) is now expanding every year because of their high energy density. The demand for high energy density has been increasing to improve the performance of these applications. Therefore, the development of high energy density batteries has been actively pursued worldwide [1]. High energy density cells are also being pursued for use in electric power grids aiming at load frequency control and supply-demand control. Recently, the substitution of cobalt in cathode materials with other transition metals has become important for high energy density, low cost and safety with regard to large scale applications. Layered Ni-rich lithium transition metal oxides have attracted much attention as cathode materials of lithium ion batteries because they provide high capacities of around 200 mAh g^{-1}[2-4].

$LiNi_{0.5}Co_{0.2}Mn_{0.3}O_2$ has been considered to be one of the most promising cathodes because it has a higher discharge capacity than $LiCoO_2$ and $LiNi_{1/3}Co_{1/3}Mn_{1/3}O_2$, both of which are currently used in commercially available LIBs [4-6]. However, the high content

of Ni and the high cut-off voltage (4.5-4.6 V vs. Li^+/Li) used to obtain a high capacity result in poor cyclic performance [7]. Studies in the literature have so far revealed several important factors for the capacity fading of the layered materials, which include the decomposition of electrolytes through side reactions of $LiPF_6$ with water molecules [6-8] and structural transformations to a mixed spinel/rock-salt structure on the individual particle surface [8, 9]. The dissolution of transition metal ions from $LiNi_{0.5}Co_{0.2}Mn_{0.3}O_2$ is also considered as a degradation factor [10]. Besides chemical instability, crack formation within the secondary particles is well-known to be a degradation factor at high potentials [11, 12]. The cracks disconnect the electrical pathway among the grains in a secondary particle. The irreversible reaction of electrolyte decomposition occurs not only on the surface, but also inside the cracks, and as a result it accelerates crack formation.

As an approach to suppress direct contact between the cathode materials and the electrolyte solution, surface coating with various oxides such as Al_2O_3 [13, 14], ZrO_2 [15], TiO_2 [16, 17], and CeO_2 [18] has been investigated. In addition, there have been several reports that lithium boron oxide having high ion conductivity is being used as a coating material in order to reduce the over-potential on the surface of the cathode particles [19-21]. However, we preliminarily confirmed that the cathode coated with lithium boron oxide by an impregnation method showed poor performance. In the case of the conventional impregnation method, it is considered that the coating material tends to aggregate at the time of deposition. Moreover, the crystal structures of the boron coating material were not clear [19-21].

In Chapter 4, lithium boron oxide (LBO) was coated on $LiNi_{0.5}Co_{0.2}Mn_{0.3}O_2$ by an antisolvent precipitation method to improve electrochemical performance. The conventional impregnation method was also examined for comparison. The surface of the

cathode active materials coated by the antisolvent precipitation method had a more uniform surface morphology than that coated by the impregnation method. In addition, the coating material formed by the antisolvent precipitation method had a structure containing more lithium than the impregnation method. It was considered that these properties of LBO coating contributed to improvement of cyclability and rate capability. In addition, the effects of the LBO coating on the improvement of chemical and physical stability of $LiNi_{0.5}Co_{0.2}Mn_{0.3}O_2$ were discussed.

4.2 Experimental

4.2.1 Synthesis of LBO-coated $LiNi_{0.5}Co_{0.2}Mn_{0.3}O_2$

LBO-coated $LiNi_{0.5}Co_{0.2}Mn_{0.3}O_2$ powder was prepared *via* an antisolvent precipitation method. Lithium metaborate ($LiBO_2$, Wako Pure Chemical Industries, Ltd.) was added to ultra-pure water by 0.5, 1, 2, 5 wt.% with respect to $LiNi_{0.5}Co_{0.2}Mn_{0.3}O_2$. This suspension was allowed to stand overnight at 45ºC and lithium metaborate was completely dissolved. $LiNi_{0.5}Co_{0.2}Mn_{0.3}O_2$ (NCM) powder was added to the LBO solution followed by stirring at 50ºC. Then ethanol was added dropwisely to the suspension with vigorous stirring. LBO was precipitated out on the $LiNi_{0.5}Co_{0.2}Mn_{0.3}O_2$ by a poor solubility in ethanol. The precipitate was filtered, and dried at 60ºC for 12 h. The powder was then annealed at 500ºC for 8 h to obtain the LBO-coated $LiNi_{0.5}Co_{0.2}Mn_{0.3}O_2$. The powder samples of different amounts of LBO coating were prepared, and hereafter referred to as 0.5, 1, 2, and 5 wt.% LBO-NCM.

A conventional impregnation procedure was also used to obtain LBO-coated sample as a reference to those prepared *via* the antisolvent precipitation method. $LiNi_{0.5}Co_{0.2}Mn_{0.3}O_2$ powder was added to an aqueous LBO solution ($LiNi_{0.5}Co_{0.2}Mn_{0.3}O_2$: $LiBO_2$ = 100 : 0.5) followed by stirring until the solvent was completely evaporated. The powder was then annealed at 500ºC for 8 h to obtain the LBO-coated $LiNi_{0.5}Co_{0.2}Mn_{0.3}O_2$, which is referred to as 0.5 wt.% LBO-NCM-im.

4.2.2 Electrode fabrication and charge/discharge tests

A cathode slurry was prepared by mixing the oxide powder (94 wt.%), an acetylene black conductor (Denka Co., Ltd., 3 wt.%), a polyvinylidene fluoride binder (Kureha Corp., 3 wt.%) using 1-methyl-2-pyrrolidinone (Wako Pure Chemical Industries, Ltd.) as a solvent. The slurry was cast by the doctor blade method on an Al foil current collector (20 μm in thickness), and then dried at 80ºC for 18 h under vacuum. Disks of 13 mm in diameter were punched out from the cast, and used as cathodes. The loading of the cathode was typically 6.0 mg cm^{-2}.

Charge and discharge tests were carried out using two-electrode half cells, which were assembled in an Ar-filled glove box (Miwa Manufacturing Co., Ltd., MDB-1NKP-DS). Li metal foil (Honjo Metal) was used as a counter electrode, and a microporous polypropylene monolayer membrane (Celgard® 2400) was used as a separator. The electrolyte solution was 1 M $LiPF_6$ dissolved in a 1:2 (by volume) mixture of ethylene carbonate (EC) and dimethyl carbonate (DMC) (Kishida Chemical Co., Ltd., Battery Grade). The charge and discharge tests were performed galvanostatically at a 0.1 C rate (1 C = 200 mAh g^{-1}) between 2.5 and 4.6 V at 30ºC using a TOSCAT-3100 battery test system (TOYO SYSTEM CO., LTD.). The rate capability tests were performed in the voltage range of 2.8-4.6 V at 0.1, 0.2, 0.5, 1, and 2 C rates. The electrochemical impedance spectroscopy was evaluated at 3.8 V over the frequency range of 100 kHz and 0.1 Hz at 30ºC after 1, 20, 60, and 100 cycles using a three-electrode cell.

4.2.3 Characterization

The crystal structures of the $LiNi_{0.5}Co_{0.2}Mn_{0.3}O_2$ powders uncoated and coated with LBO were investigated by X-ray diffraction (XRD, RIGAKU, Rint2500) using Cu Kα

radiation. The morphology of the particles was observed with a scanning electron microscope (SEM, JSM-7001FD). The particles were embedded in a polymer resin, and cross-sectional samples for SEM observation were prepared by a cross-section polisher (JEOL, SM-09010DM). Elemental distribution was investigated by an electron energy loss spectroscopy (EELS) coupled with a scanning transmission electron microscope (STEM).

4.2.4 Estimation of dissolved transition metal ions

The amounts of transition metal ions dissolved from NCM during cycling and storing were measured inductively coupled plasma emission spectroscopy (ICP, Thermo Fisher Scientific, iCAP 6000 SERIES). In order to promote the dissolution of transition metals, charge and discharge tests of the uncoated and coated samples were performed at 0.5 C in the voltage range of 2.8-4.6 V at an elevated temperature of 45ºC. The cell was fully charged to 4.6V at 10^{th} cycle, and stored at 45ºC for 120 h under the open-circuit conditions. After the cell was disassembled, the Li metal anode was soaked in ultra-pure water to dissolve transition metals deposited on it. The solution was diluted with aqueous 0.05 mol dm^{-3} HCl. The concentration of dissolved transition metal ions in the solution was analyzed by ICP.

4.3 Results and Discussion

4.3.1 Structure and morphology of LBO-coated $LiNi_{0.5}Co_{0.2}Mn_{0.3}O_2$

XRD patterns of uncoated and LBO-coated NCM samples are shown in Fig. 4-1(a). The XRD pattern of each sample was typical of the layered structure of NCM. Crystalline LBOs were not detected by XRD, which indicated that LBO may exist as amorphous state. The peak intensity ratio *R* of the (003) to the (104) peak is known to be a measure of the cation mixing [7]. The *R* values of 0.5 wt.% LBO-NCM and 0.5 wt.% LBO-NCM-im were almost equal to each other. The *R* value decreased with increasing the amount of modification. Han et al. reported that this phenomenon is attributed to partial occupation of small-sized boron ions in lithium ion positions within the layered structure [22]. In order to estimate the structure of LBO, only the coating material (without $LiNi_{0.5}Co_{0.2}Mn_{0.3}O_2$) were synthesized *via* the antisolvent precipitation and the impregnation method in similar manners. Their XRD patterns are shown in Fig. 4-1(b) and (c), respectively. The diffraction pattern of the coating material prepared by the antisolvent precipitation method was assigned to that of $LiBO_2$. On the other hand, the diffraction peaks of the coating material prepared by the impregnation method were assigned to the mixture of $LiB_2O_4{\cdot}H_2O$, $Li_2B_4O_9$, and $LiBO_2$.

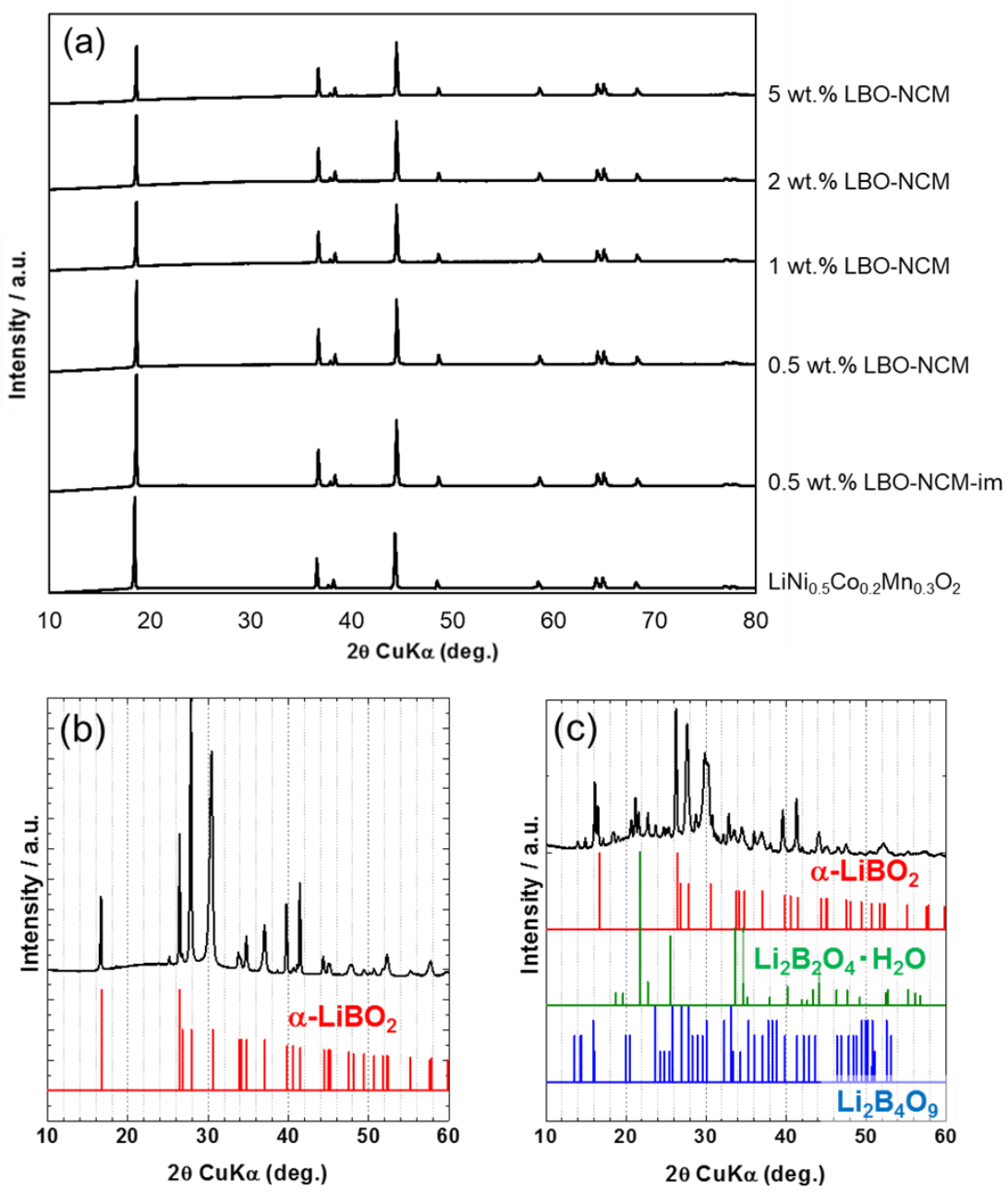

Fig. 4-1 X-ray diffraction patterns of (a) uncoated and LBO-coated NCM samples by the antisolvent precipitation method, and the coating material (without NCM particles) prepared by (b) the antisolvent precipitation method and (c) the impregnation method after heat-treated at 500°C for 8 h.

In the antisolvent precipitation method, ethanol was used to strip off the hydrated water coordinated with lithium ions and borate ions. This treatment promotes the reaction of free lithium ions and borate ions to give lithium metaborate precipitation. Since the coating material is deposited in a large amount of solution, a uniform coating film can be formed. As a result, it was considered that a single phase of $LiBO_2$ was obtained. On the contrary, in the impregnation method, the solute is recrystallized during evaporating the solvent. Because the structure of the coating material is varied with the solubility of the solute, it may be difficult to obtain a single phase. In addition, since the hydrate, $Li_2B_2O_4{\cdot}H_2O$, formed *via* the impregnation method introduces moisture into the cell, it is considered to promote the generation of hydrogen fluoride. Furthermore, it has been reported that the lithium-ion conductivity of $x Li_2O$-B_2O_3 glass exhibits the maximum at around x = 3.5 at room temperature [23]. Therefore, the lithium ion conductivity of the coating layer, which is mainly consisted of $LiBO_2$, obtained by the precipitation method is expected to be higher than the mixture of $LiBO_2$, $LiB_2O_4{\cdot}H_2O$ and $Li_2B_4O_9$ obtained by the impregnation method because $LiBO_2$ has a higher Li/B ratio and thereby closer ratio to the optimum value than the other two.

Fig. 4-2(a)-(f) show SEM images of the uncoated and the LBO-coated $LiNi_{0.5}Co_{0.2}Mn_{0.3}O_2$ samples. No appreciable difference in surface morphology was observed between the uncoated NCM (Fig. 4-2(a)) and 0.5 wt.% LBO-NCM (Fig. 4-2(b)). The coating layer on the surface of 0.5 wt.% LBO-NCM seemed to be thin and uniform. On the other hand, the surface of 0.5 wt.% LBO-NCM-im was covered with small particles (100 nm or less in diameter). This result suggests that the coating material prepared by the impregnation method is aggregated. Fig. 4-2(c)-(f) showed that the grain boundaries of the primary particles became unclear as the amount of LBO increased on

the surface of $LiNi_{0.5}Co_{0.2}Mn_{0.3}O_2$. In the 5 wt.% LBO-NCM (Fig. 4-2(f)), the modification with LBO seems to be excessive.

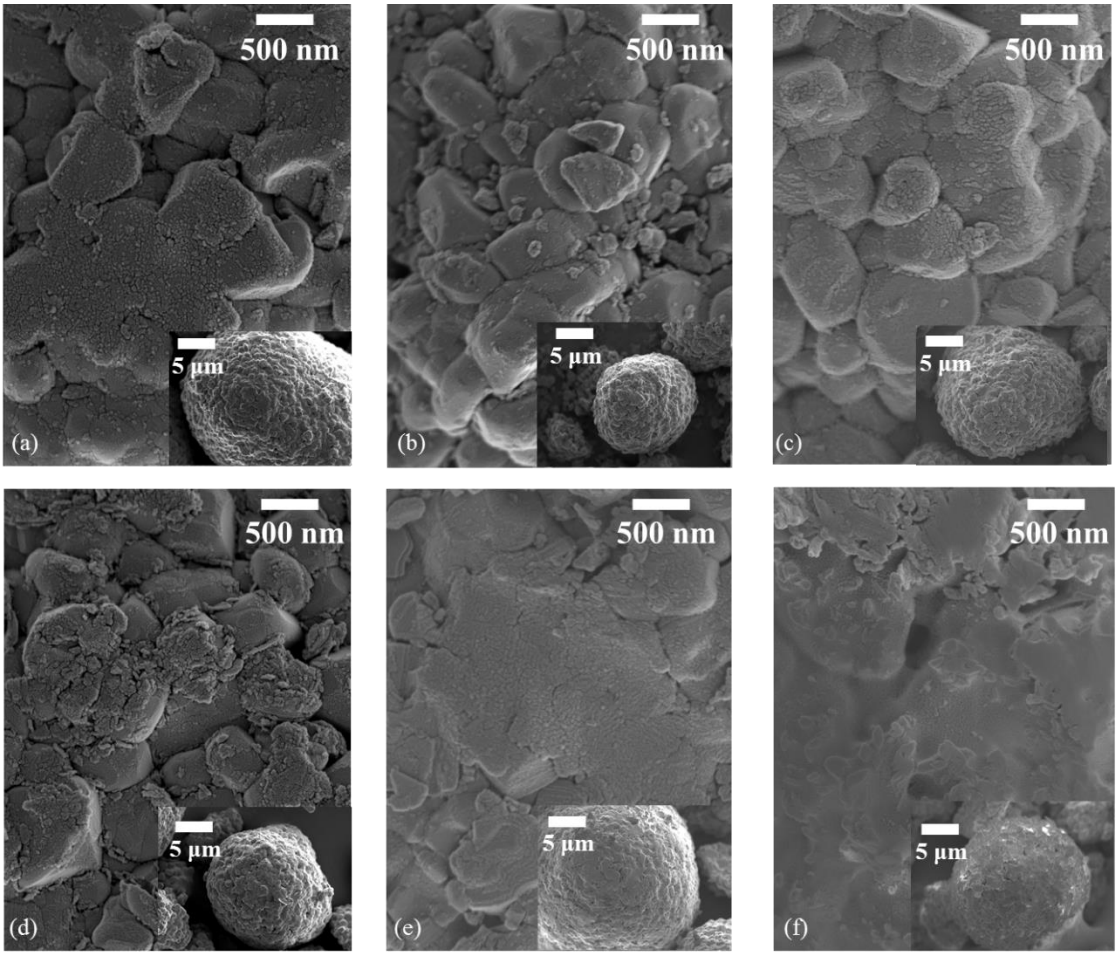

Fig. 4-2 SEM images of (a) uncoated NCM, (b) 0.5 wt.% LBO-NMC-im prepared by the impregnation method, (c) 0.5, (d) 1, (e) 2, and (f) 5 wt.% of LBO-NCM prepared by the precipitation method.

A STEM-BF and a STEM-HAADF image of 0.5 wt.% LBO-NCM are shown in Fig. 4-3(a) and (b), respectively. In Fig. 4-3(a), it was confirmed that the primary particles are densely sintered to form a secondary particle. Fig. 4-3(b) shows the vicinity of the surface

of 0.5 wt.% LBO-NCM, in which three layers labelled as 1, 2, and 3 were observed. Layer 1 is the surface of the particle. It is considered to be impurity deposits, and is unavoidable in the analysis. Layer 2 is the LBO coating layer, the thickness of which was 3 nm. Layer 3 is the NCM bulk. STEM-EELS line analysis (Fig. 4-3(c)) showed the presence of boron in Layer 2, which clearly confirmed the presence of LBO on the particle surface.

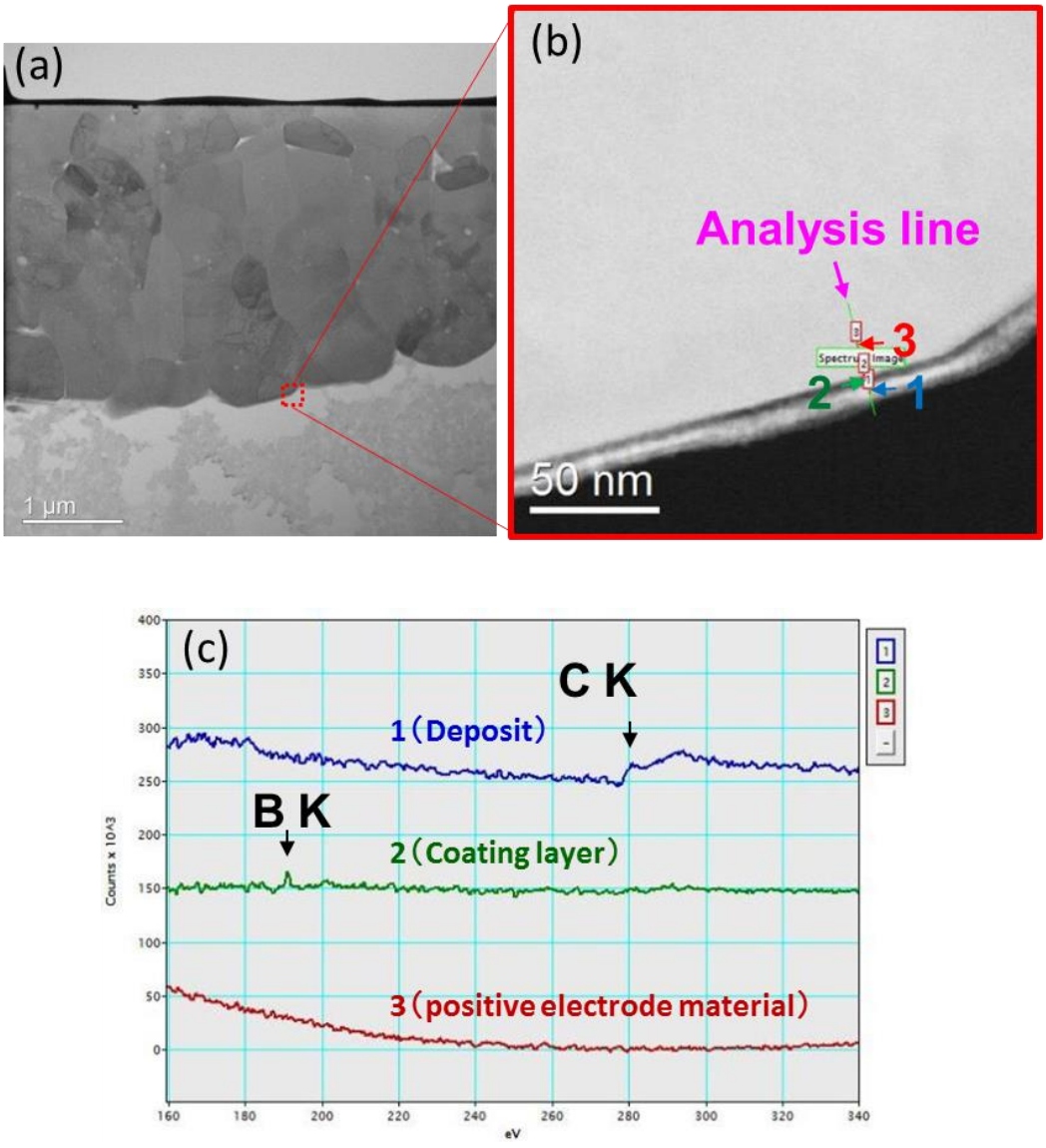

Fig. 4-3 (a) STEM-BF image, (b) STEM-HAADF image, and (c) STEM-EELS line analysis of 0.5 wt.% LBO-NCM.

4.3.2 Charge and discharge properties

Figs. 4-4(a)-(c) show the charge and discharge profiles at 0.1 C between 2.5 and 4.6 V at 30ºC for the uncoated NCM, 0.5 wt.% LBO-NCM and 0.5 wt.% LBO-NCM-im, respectively. All samples provided discharge capacities of around 200 mAh g^{-1} at the initial cycles, which are typical values of the layered Ni-rich lithium transition metal oxide cathodes [2-4]. From these results, it was considered that the LBO coating layers synthesized by both methods do not inhibit lithium ion transport. Fig. 4-4(d) shows the variations of specific capacity with cycle number. The capacity of the uncoated NCM and 0.5 wt.% LBO-NCM-im decreased more rapidly than that of 0.5 wt.% LBO-NCM; that is, the capacity fading on cycling was successfully suppressed for the LBO-coated sample prepared by the antisolvent precipitation method. At the 150^{th} cycle, 64.5% of the initial discharge capacity was maintained for 0.5 wt.% LBO-NCM, which was much higher than that for the other samples (46.6% and 46.9% for the uncoated NCM and 0.5 wt.% LBO-NCM-im, respectively). It was shown that the LBO coating prepared by the antisolvent precipitation method is effective for improving the cycleability of $LiNi_{0.5}Co_{0.2}Mn_{0.3}O_2$. However, the coating using the impregnation method did not contribute to improvement of cycleability probably because it was non-uniform as shown in Fig. 4-2(b) and thereby the suppression of side reactions at $LiNi_{0.5}Co_{0.2}Mn_{0.3}O_2$ cathode/electrolyte interface was insufficient.

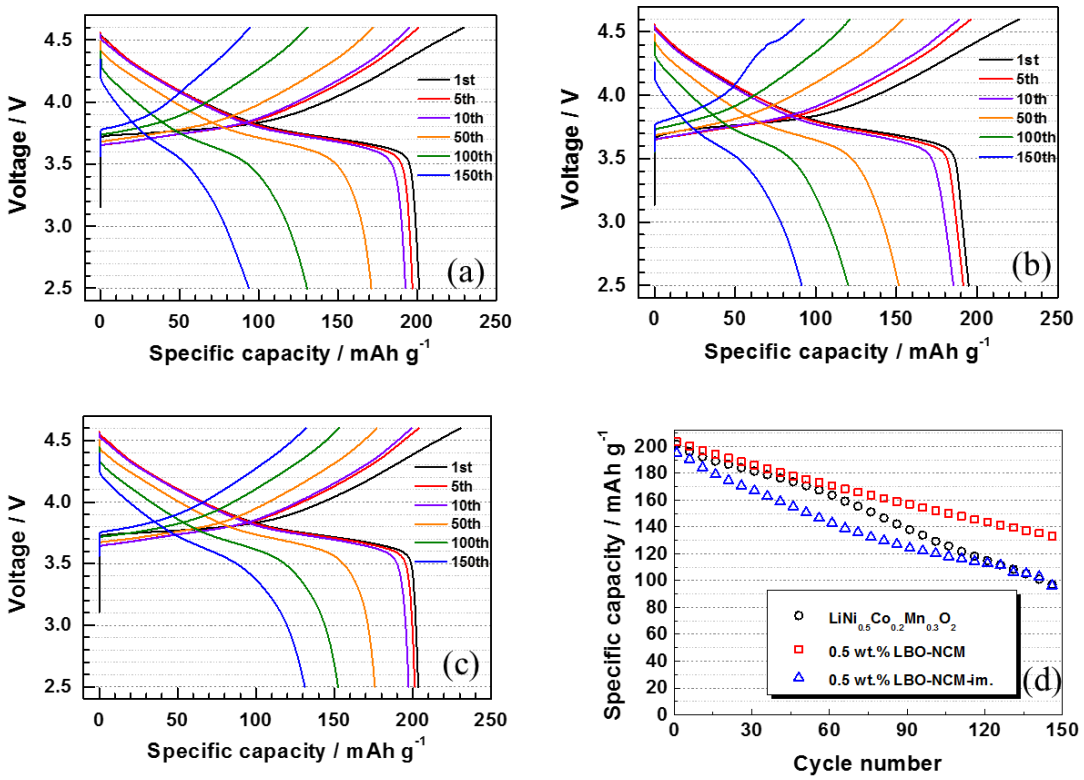

Fig. 4-4 Charge-discharge curves of (a) uncoated NCM, (b) 0.5 wt.% LBO-NCM-im, and (c) 0.5 wt.% LBO-NCM and (d) their capacity retentions measured at 0.1C between 2.5 and 4.6 V at 30°C.

4.3.3 Effect of coating amount

Fig. 4-5(a) shows the variations of specific capacity with cycle number for LBO coated samples with different amounts. The charge/discharge tests were performed at 0.5 C, and the fully reversible capacity was confirmed at 0.1 C in every 20 cycles. The capacity retentions of the uncoated NCM, and 1 and 2 wt.% LBO-NCM at the 211th cycle (measured at 0.1 C) were 78.3%, 81.4% and 82.2%, respectively. In the case of 5 wt.%

LBO-NCM, the discharge capacity decreased rapidly; therefore, the cycle test was interrupted at the 80th cycle. This deterioration was attributable to an increase in the interfacial resistance owing to an excess amount of the coating material as shown in Fig. 4-2(f). Thus, we concluded that the optimum coating amount was 2 wt.%.

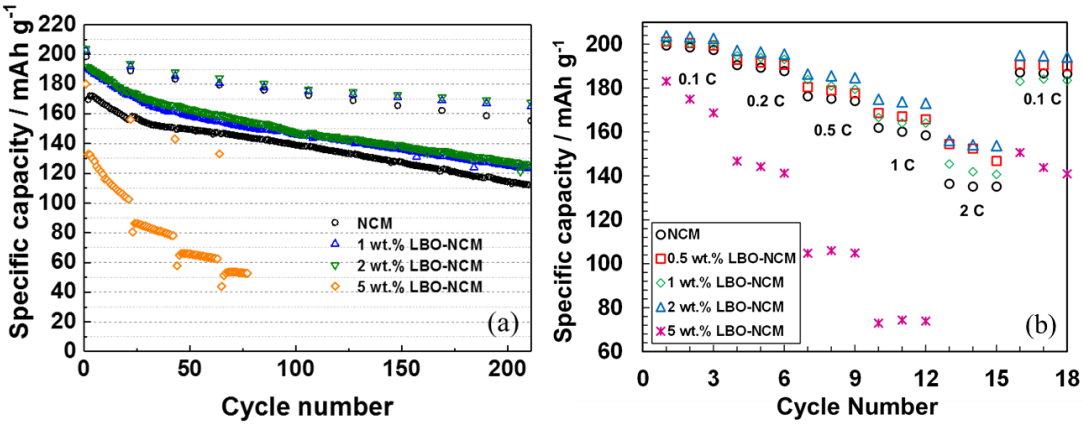

Fig. 4-5 (a) Variations of discharge capacity with cycle number of uncoated NCM, 1, 2 and 5 wt.% LBO-NCM cycled at 0.5 C between 2.8 and 4.6 V at 30°C. The full reversible capacity was checked at 0.1 C every 20 cycles. (b) Rate performance of uncoated NCM, 0.5, 1, 2 and 5 wt.% LBO-NCM measured at 0.1, 0.2, 0.5, 1.0, and 2.0 C.

Fig. 4-5(b) shows the rate capability of the uncoated NCM, 0.5, 1, 2 and 5 wt.% LBO-NCM. The LBO coated cathodes exhibited better rate capability than the uncoated NCM, and especially the discharge capacity of 2 wt.% LBO-NCM at 2 C was by 14% higher than the uncoated NCM. These results suggest that the optimum amount of coating material promotes the diffusion of lithium ions in addition to suppressing side reactions at the cathode/electrolyte interface.

In order to investigate the reactivity of LBOs with impurities in the electrolyte solution, 1 g of the coating material (without $LiNi_{0.5}Co_{0.2}Mn_{0.3}O_2$) prepared by the antisolvent precipitation method was soaked in a mixture of the electrolyte (20 mL), and stirred at 45ºC for 20 days being exposed to the air as an accelerated test. The solution was filtered and the XRD pattern of the residue was measured, which is shown in Fig. 4-6. $LiB(OH)_4$ was a main compound in the residue, which was formed by a reaction of H_2O with $LiBO_2$. From this result, it was suggested that the presence of the coating material effectively traps H_2O in the electrolyte solution, which may inhibit HF formation from $LiPF_6$ [21].

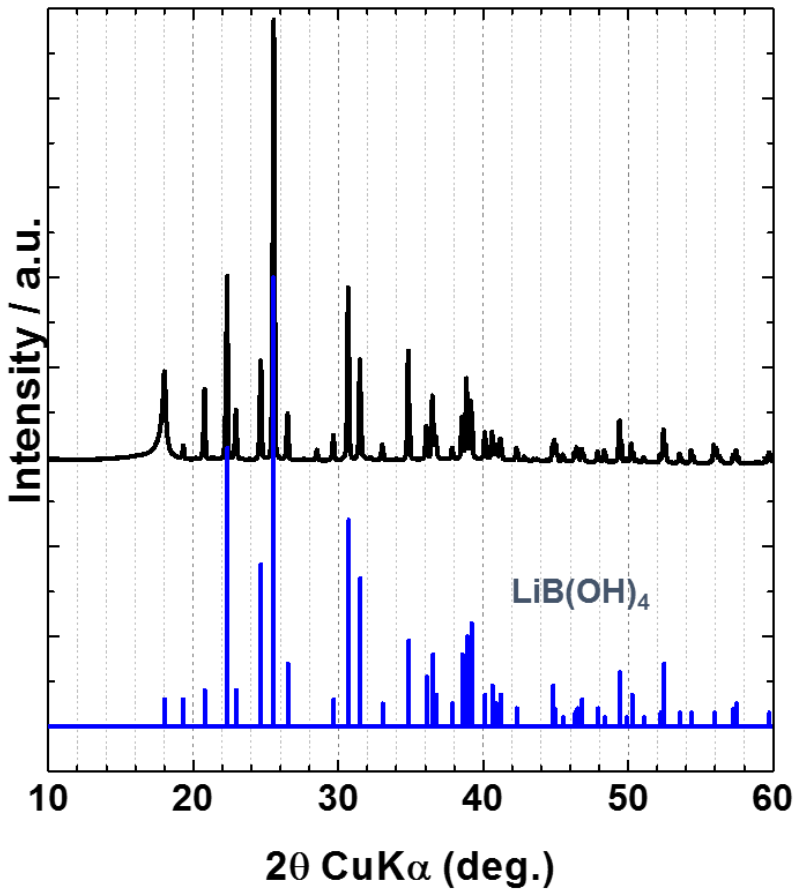

Fig. 4-6 XRD patterns of the LBO powder prepared by the antisolvent precipitation method after soaked in a mixture of the electrolyte (20 ml) for 20 days in the air.

As mentioned earlier, dissolution of transition metal ions from the cathode is one of the reasons for capacity fading. Hence the effect of LBO-coating on transition metal ion dissolution into the electrolyte was investigated. Fig. 4-7 shows the amounts of dissolved transition metal ions at 45ºC plotted against the amount of coated $LiBO_2$. All the three transition metals were dissolved more or less at 45°C, and the highest amount was Ni followed by Mn and Co. However, the presence of LBO at the surface was significantly effective for suppression of the dissolution, and 2 wt.% LBO reduced the total amount of dissolved transition metal ions to 37% of the uncoated NCM. It is considered that the surface modification of NCM with LBO suppresses direct contact with the electrolyte and decreases side reactions at the cathode/electrolyte interface, which resulted in the suppression of the dissolution of transition metal ions.

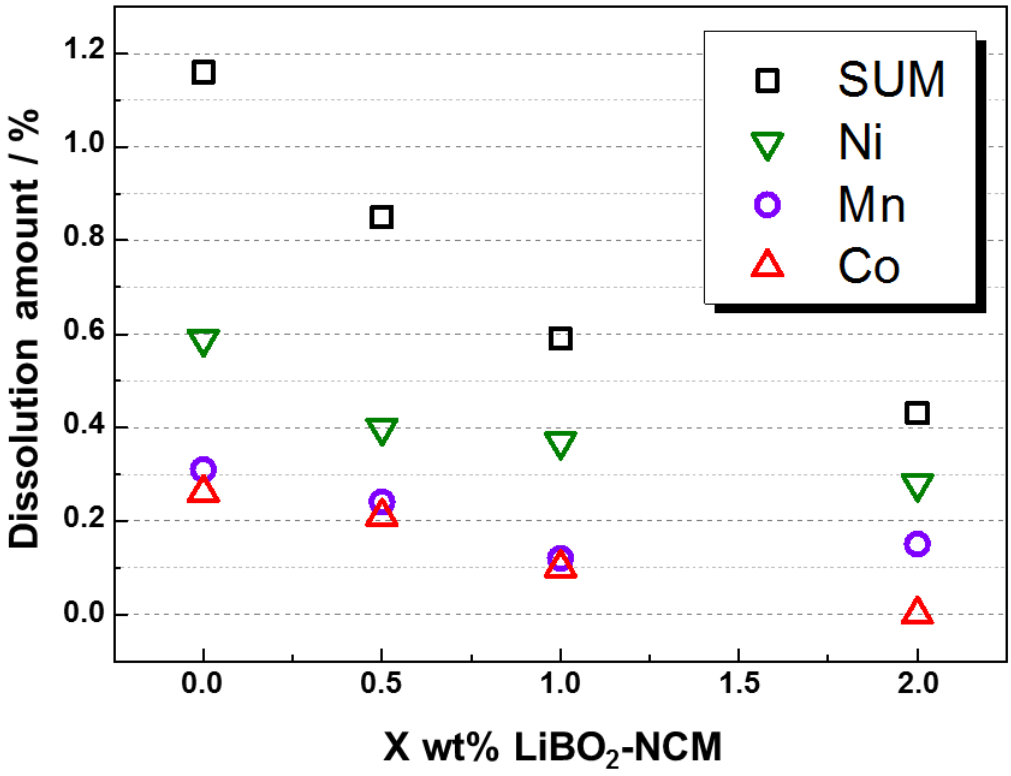

Fig. 4-7 Amounts of dissolved transition metal ions from uncoated and LBO coated NCM after 10 cycles at 0.5 C and stored at the charged state at 45°C for 120 h.

Electrochemical impedance spectroscopy was carried out to investigate the interfacial electrochemistry. Fig. 4-8 shows Nyquist plots of the uncoated NCM, 0.5 and 2 wt.% LBO-NCM at 3.8 V after the 1st, 20th, 60th, and 100th cycle. Generally, the intersection between the real axis and the higher frequency arc is attributed to the ohmic resistance of the electrolyte solution. The higher-frequency arc is assigned to the contact resistance among the active material and conducting carbon particles. The lower frequency arc is assigned to the lithium ion transfer resistance (charge transfer resistance) at the electrode/electrolyte interface. Though the initial impedance of the 2 wt.% LBO-NCM sample was higher than that of the uncoated one, the increase in the total impedance

was suppressed by the LBO coating during cycling. These results indicate that the oxidative decomposition of the electrolyte on the particle surface and the resulting inactivation of the particle surface were inhibited by the LBO coating.

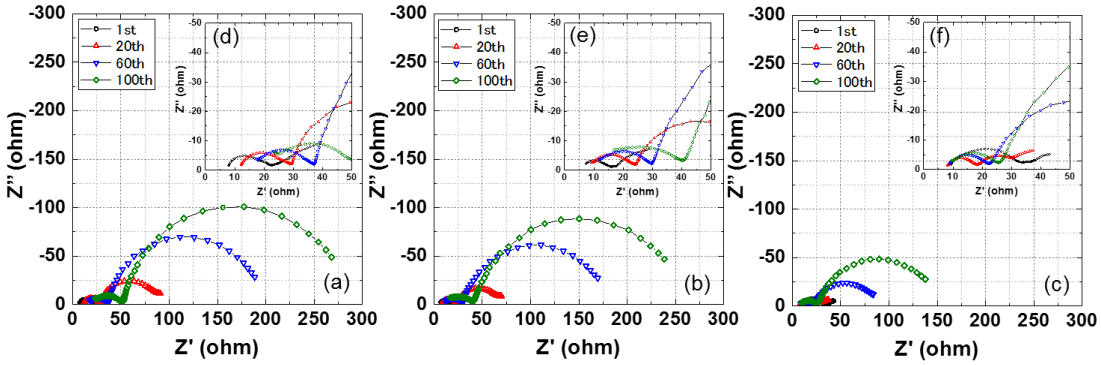

Fig. 4-8 Nyquist plots of (a) uncoated NCM, (b) 0.5 wt.% LBO-NCM and (c) 2 wt.% LBO-NCM measured at 3.8 V in the 1st, 20th, 60th, and 100th cycle at 30°C. Plots (d), (e) and (f) are magnified ones of (a), (b) and (c), respectively.

Fig. 4-9 shows cross-sectional SEM images of the uncoated NCM and 2 wt.% LBO-NCM obtained before and after long-term cycling. The tests were performed at 0.5 C between 2.5 and 4.6 V, while the reversible capacity was checked every 20 cycles at 0.1 C. Before cycling, the particle consisted of small and tightly bound primary particles of NCM. However, many cracks were formed along the grain boundaries of the secondary particles after 106 cycles in the uncoated sample, and crack formation was further extended after 211 cycles. On the other hand, crack formation was less significant even after 211 cycles for the 2 wt.% LBO-NCM. The electrolyte solution can penetrate into the

intergranular cracks inside the particles. This may cause irreversible electrolyte decomposition within the particles. As a result, the decomposition products accumulated in the intergranular cracks and accelerated the capacity fading as shown in Fig. 4-5(a). On the other hand, the generation of cracks was clearly suppressed for the LBO-coated sample. It is considered that the LBO coating suppressed the progress of the cracks probably by inhibiting the penetration of the electrolyte solution into the intergranular cracks.

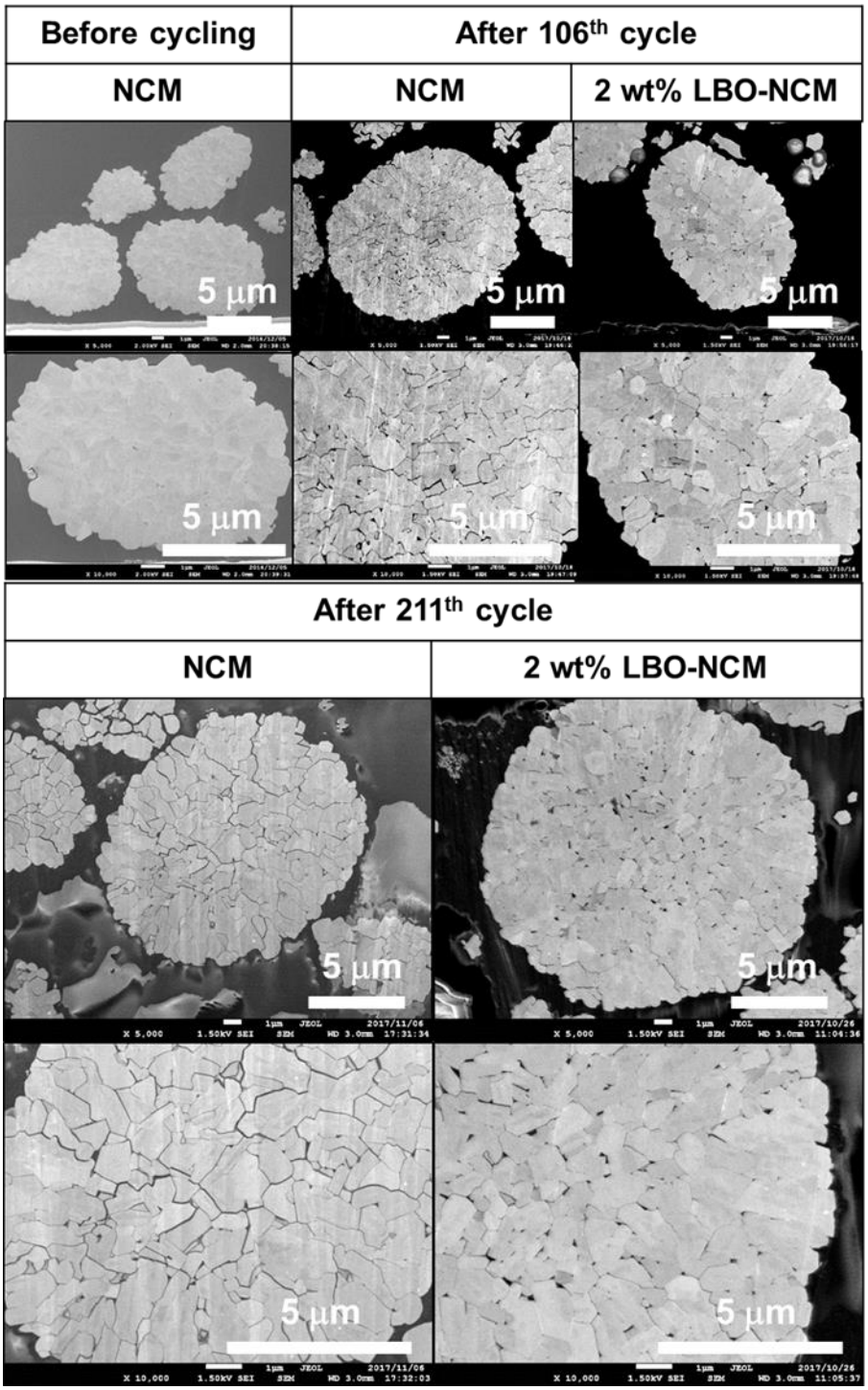

Fig. 4-9 Cross sectional FE-SEM images of uncoated NCM and 2 wt.% LBO-NCM particles before cycling, after 106 and after 211 cycles at 0.5 C between 2.5 and 4.6 V in 1 M $LiPF_6$/EC+DMC (1:2) at 30°C.

4.4 Conclusions

The surface of $LiNi_{0.5}Co_{0.2}Mn_{0.3}O_2$ was coated with LBOs by an antisolvent precipitation and an impregnation method to improve its electrochemical performance. In the antisolvent precipitation method, the $LiNi_{0.5}Co_{0.2}Mn_{0.3}O_2$ particles were coated with a thin and uniform layer of $LiBO_2$. On the contrary, the surface was covered with small particles of a mixture of $LiB_2O_4{\cdot}H_2O$, $Li_2B_4O_9$, and $LiBO_2$ in the impregnation method. The LBO layer coated by the antisolvent precipitation method suppressed the capacity fading on cycling more effectively than that coated by the impregnation method. The optimum value of the amount of the coating material was 2 wt.%. The LBO-coated cathode prepared by the antisolvent precipitation method also exhibited improved rate capability. As the reasons for the improvement in cyclability, it was found that the dissolution of transition metal ions and the increase of impedance are suppressed by the LBO coating. Another important factor is that the LBO-coating suppressed clack formation along the grain boundaries of the secondary particles by inhibiting the penetration of the electrolyte solution into the intergranular cracks. It is therefore concluded that LBO coating by the antisolvent precipitation method is an easy and effective way for improving the cyclability of $LiNi_{0.5}Co_{0.2}Mn_{0.3}O_2$ cathode.

References

[1] J.-M. Tarascon, M. Armand, Issues and challenges facing rechargeable lithium batteries, Nature 414 (2001) 359-367.

[2] P. Yan, J. Zheng, M. Gu, J. Xiao, J.-G. Zhang, C.-M. Wang, Intragranular cracking as a critical barrier for high-voltage usage of layer-structured cathode for lithium-ion batteries, Nat. Commun. 8 (2017) 14101.

[3] K. Ishidzu, Y. Oka, T. Nakamura, Lattice volume change during charge/discharge reaction and cycle performance of $Li[Ni_xCo_yMn_z]O_2$, Solid State Ionics 288 (2016) 176-179.

[4] S.-K. Jung, H. Gwon, J. Hong, K.-Y. Park, D.-H. Seo, H. Kim, J. Hyun, W. Yang, K. Kang, Understanding the Degradation Mechanisms of $LiNi_{0.5}Co_{0.2}Mn_{0.3}O_2$ Cathode Material in Lithium Ion Batteries, Adv. Energy Mater. 4 (2014) 1300787.

[5] M. Noh, J. Cho, Optimized Synthetic Conditions of $LiNi_{0.5}Co_{0.2}Mn_{0.3}O_2$ Cathode Materials for High Rate Lithium Batteries via Co-Precipitation Method, J. Electrochem. Soc. 160(1) (2013) A105-A111

[6] M. Borner, F. Horsthemke, F. Kollmer, S. Haseloff, A. Friesen, P. Niehoff, S. Nowak, M. Winter, F. M. Schappacher, Degradation effects on the surface of commercial $LiNi_{0.5}Co_{0.2}Mn_{0.3}O_2$ electrodes, J. Power Sources 335 (2016) 45-55.

[7] H.-J. Noh, S. Youn, C. S. Yoon, Y.-K. Sun, Comparison of the structural and electrochemical properties of layered $Li[Ni_xCo_yMn_z]O_2$ (x=1/3, 0.5, 0.6, 0.7, 0.8 and 0.85) cathode material for lithium-ion batteries, J. Power Sources 233 (2013) 121-130.

[8] F. Lin, L. M. Markus, D. Nordlund, T.-C. Weng, M. D. Asta, H. L. Xin, M. M. Doeff,

Surface reconstruction and chemical evolution of stoichiometric layered cathode materials for lithium-ion batteries, N. Commun. 5 (2014) 3529.

[9] C.-H. Shen, Q. Wang, H.-J. Chen, C.-G. Shi, H.-Y. Zhang, L. Huang, J.-T. Li, S.-G. Sun, In Situ Multitechnical Investigation into Capacity Fading of High-Voltage $LiNi_{0.5}Co_{0.2}Mn_{0.3}O_2$, ACS Appl. Mater. Interfaces 8 (2016) 35323-35335.

[10] J. A. Gilbert, I. A. Shkrob, D. P. Abraham, Transition Metal Dissolution, Ion Migration, Electrocatalytic Reduction and Capacity Loss in Lithium-Ion Full Cells, J. Electrochem. Soc. 164(2) (2017) A389-A399.

[11] J. Li, L. E. Downie, L. Ma, W. Qiu, J. R. Dahn, Study of the Failure Mechanisms of $LiNi_{0.8}Co_{0.1}Mn_{0.1}O_2$ Cathode Material for Lithium Ion Batteries, J. Electrochem. Soc. 162(7) (2015) A1401-A1408.

[12] H. Liu, M. Wolf, K. Karki, Y. -S. Yu, E. A. Stach, J. Cabana, K. W. Chapman, P. J. Chupas, Intergranular Cracking as a Major Cause of Long-Term Capacity Fading of Layered Cathodes, Nano Lett. 17 (2017) 3452-3457.

[13] Y. Shi, M. Zhang, D. Qian, Y. S. Meng, Ultrathin Al_2O_3 Coatings for Improved Cycling Performance and Thermal Stability of $LiNi_{0.5}Co_{0.2}Mn_{0.3}O_2$ Cathode Material, Electrochim. Acta 203 (2016) 154-161.

[14] B. Seteni, N. Rapulenyane, J. C. Ngila, S. Mpelane, H. Luo, Coating effect of $LiFePO_4$ and Al_2O_3 on $Li_{1.2}Mn_{0.54}Ni_{0.13}Co_{0.13}O_2$ cathode surface for lithium ion batteries, J. Power Sources 353 (2017) 210-220.

[15] J.-Z. Kong, S.-S. Wang, G.-A. Tai, L. Zhu, L.-G. Wang, H.-F. Zhai, D. Wu, A.-D. Li, H. Li, Enhanced electrochemical performance of $LiNi_{0.5}Co_{0.2}Mn_{0.3}O_2$ cathode material by ultrathin ZrO_2 coating, J. Alloys Comp. 657 (2016) 593-600.

[16] W. Liu, M. Wang, X. L. Gao, W. Zhang, J. Chen, H. Zhou, X. Zhang, Improvement

of the high-temperature, high-voltage cycling performance of $LiNi_{0.5}Co_{0.2}Mn_{0.3}O_2$ cathode with TiO_2 coating, J. Alloys Comp. 543 (2012) 181-188.

[17] L. Yu, X. Qiu, J. Xi, W. Zhu, L. Chen, Enhanced high-potential and elevated-temperature cycling stability of $LiMn_2O_4$ cathode by TiO_2 modification for Li-ion battery, Electrochim. Acta 51 (2006) 6406-6411.

[18] K. Liu, G.-L. Yang, Y. Dong, T. Shi, and L. Chen, Enhanced cycling stability and rate performance of $LiNi_{0.5}Co_{0.2}Mn_{0.3}O_2$ by CeO_2 coating at high cut-off voltage, J. Power Sources 281 (2015) 370-377.

[19] D. Wang, X. Li, Z. Wang, H. Guo, X. Chen, X. Zheng, Y. Xu, J. Ru, Multifunctional Li_2O-$2B_2O_3$ coating for enhancing high voltage electrochemical performances and thermal stability of layered structured $LiNi_{0.5}Co_{0.2}Mn_{0.3}O_2$ cathode materials for lithium ion batteries, Electrochim. Acta 174 (2015) 1225-1233.

[20] S. Tan, L. Wang, L. Bian, J. Xu, W. Ren, P. Hu, A. Chang, Highly enhanced low temperature discharge capacity of $LiNi_{1/3}Co_{1/3}Mn_{1/3}O_2$ with lithium boron oxide glass modification, J. Power Sources 277 (2015) 139-146.

[21] J. S. Chae, S. B. Yoon, W. S. Yoon, Y. M. Kang, S. M. Park, J. W. Lee, K. C. Roh, Enhanced high-temperature cycling of Li_2O-$2B_2O_3$-coated spinel-structured $LiNi_{0.5}Mn_{1.5}O_4$ cathode material for application to lithium-ion batteries, J. Alloys Comp. 601 (2014) 217-222.

[22] S.-H. Han, J. H. Song, T. Yim, Y.-J. Kim, J.-S. Yu, S. Yoon, Improvement of structural stability during high-voltage cycling in high-nickel cathode materials with B_2O_3 addition, J. Electrochem. Soc. 163(5) (2016) A748-750.

[23] E. E. Horopanitis, G. Perentzis, E. Pavlidou, L. Papadimitriou, Electrical Properties of Lithiated Boron Oxide Fast-ion Conducting Glasses, IONICS 9 (2003) 88-94.

CHAPTER 5

Influence of Lithium Silicate Coating on Retarding Crack Formation in $LiNi_{0.5}Co_{0.2}Mn_{0.3}O_2$ Cathode Particles

5.1 Introduction

Lithium-ion batteries with high energy density have a vital role as power sources, such as in portable devices, plug-in hybrid vehicles (PHEVs) and electric vehicles (EVs). The requirement for high capacity has grown recently to extend the driving range of EVs. High capacity cells are also expected for use in electric power grids with the aim of load frequency control and supply-demand control. In addition, the substitution of cobalt in cathode materials is important for low cost and safety with regard to large-scale applications. Layered Ni-rich lithium transition metal oxides have attracted much attention as a cathode material of lithium-ion batteries in recent years because they offer high capacities of around 200 $mAh \cdot g^{-1}$ between a lower potential of 2.5-3.0 V and a higher potential of 4.5-4.8 V (versus Li/Li^+) [1-3].

$LiNi_{0.5}Co_{0.2}Mn_{0.3}O_2$ has been considered to be one of the most promising cathodes because it has a higher discharge capacity than $LiCoO_2$ and $LiNi_{1/3}Co_{1/3}Mn_{1/3}O_2$ used currently. However, the high content of Ni and the high cut-off voltage result in poor cycle performance [4]. Studies in the literature have so far revealed several important factors for the capacity fading of the layered materials, which include the decomposition of electrolytes through side reactions of $LiPF_6$ with water molecules [5-7] and structural

transformations to a spinel/rock salt phase on the individual particle surface [2, 5, 6, 8]. The dissolution of Mn ions from $LiNi_{0.5}Co_{0.2}Mn_{0.3}O_2$ is also considered as a degradation factor. In order to mitigate these problems, coating the surface of active materials with various oxides such as SiO_2 [9-11], Li_2SiO_3 [12], Al_2O_3 [13-15], ZrO_2 [16], TiO_2 [17], CeO_2 [18], and lithium boron oxide glass [19-21] has been investigated.

Besides chemical instability, crack formation within the secondary particles is well-known as a degradation factor at such high potentials [1, 3]. The reason for the crack formation is considered to be large volume changes of the materials during charging and discharging. The cracks disconnect the electrical pathway among the grains in a secondary particle. In addition, the irreversible reaction of electrolyte decomposition occurs at the crack surface, and as a result, it accelerates cell degradation including capacity retention and coulombic efficiency.

One effective approach to suppress the generation of the cracks is adding a sintering agent. Han et al., enhanced the mechanical strength of $LiNi_{0.7}Co_{0.2}Mn_{0.1}O_2$ and the cycle performance using boron oxide as a sintering agent [22]. However, the boron oxide addition resulted in a slight decrease of the lattice parameter and a slight increase in cation mixing [22]. In addition, the materials formed from the Li and B components may increase the resistance of the cathode powders [23]. Therefore, other approaches such as surface modification of $LiNi_xCo_yMn_{1-x-y}O_2$ is required to suppress crack formation during charging and discharging.

In Chapter 5, $LiNi_{0.5}Co_{0.2}Mn_{0.3}O_2$ particles were coated with a thin layer of lithium silicate by an antisolvent precipitation method, and the charge and discharge properties were investigated. The internal morphology changes of the uncoated and lithium silicate-coated $LiNi_{0.5}Co_{0.2}Mn_{0.3}O_2$ particles during cycling were also compared. It was found that

a small amount of lithium silicate coating penetrated along the grain boundaries inside of the secondary particles upon heat-treatment, and remarkably improved the cycleability of $LiNi_{0.5}Co_{0.2}Mn_{0.3}O_2$ by suppressing crack formation and propagation during cycling.

5.2 Experimental

5.2.1 Synthesis of lithium silicate-coated $LiNi_{0.5}Co_{0.2}Mn_{0.3}O_2$

Lithium silicate-coated $LiNi_{0.5}Co_{0.2}Mn_{0.3}O_2$ powder was prepared via an antisolvent precipitation method; $LiOH \cdot H_2O$ (Wako Pure Chemical Industries, Ltd.) was added to 0.0055 M $Li_2Si_5O_{11}$ (Sigma-Aldrich) aqueous solution so as to be a ratio of the Li/Si = 2 (Li_2SiO_3). $LiNi_{0.5}Co_{0.2}Mn_{0.3}O_2$ powder (Tanaka Chemical) was added to the lithium silicate solution to be a weight ratio of $LiNi_{0.5}Co_{0.2}Mn_{0.3}O_2$: Li_2SiO_3 = 99.5 : 0.5. Then ethanol was added dropwisely to the suspension with vigorous stirring. Lithium silicate was precipitated out on the $LiNi_{0.5}Co_{0.2}Mn_{0.3}O_2$ by a poor solubility in ethanol. The precipitate was filtered, and dried at 60°C for 12 h. Then, the powder was annealed at 500°C for 8 h to obtain the lithium silicate-coated $LiNi_{0.5}Co_{0.2}Mn_{0.3}O_2$.

5.2.2 Cell fabrication

A cathode slurry was prepared by mixing the oxide powder (80 wt.%), an acetylene black conductor (Denka Co., Ltd., 10 wt.%), a polyvinylidene fluoride binder (Kureha Corp., 10 wt.%) using 1-methyl-2-pyrrolidinone (Wako Pure Chemical Industries, Ltd.) as a solvent. The slurry was cast by the doctor blade method on an Al foil current collector (20 μm thickness), and then dried at 80ºC for 18 h under vacuum. Disks of 13 mm in diameter were punched out from the cast, and used as cathodes. The loading of the cathode was typically 1.5 $mg \cdot cm^{-2}$.

5.2.3 Charge and discharge tests

Charge and discharge tests were carried out using two electrode cells, which were assembled in an Ar-filled glove box (Miwa Manufacturing Co., Ltd., MDB-1NKP-DS). Li metal foil (Honjo Metal) was used as a counter electrode, and a microporous polypropylene monolayer membrane (Celgard® 2400) was used as a separator. The electrolyte solution was 1 M $LiPF_6$ dissolved in a 1:2 (by volume) mixture of ethylene carbonate (EC) and dimethyl carbonate (DMC) by volume (Kishida Chemical Co., Ltd., Battery Grade). The charge and discharge tests were performed galvanostatically at a 0.1 C or 1 C rate (1 C = 200 mAh g^{-1}) between 2.5 and 4.6 V at 30ºC or 45ºC using a TOSCAT-3100 battery test system (TOYO SYSTEM CO., LTD.).

5.2.4 Characterization

The crystal structures of the $LiNi_{0.5}Co_{0.2}Mn_{0.3}O_2$ powders uncoated and coated with lithium silicate were investigated by X-ray diffraction (XRD, Rint2500) using Cu Kα radiation. The morphology of the oxide particles was observed with a scanning electron microscope (SEM, JSM-7001FD) and a transmission electron microscope (TEM, JEM-2100F) equipped with an energy dispersive X-ray spectroscopy (EDX). The oxide particles were embedded in a polymer resin, and samples for SEM and TEM observation were prepared by a cross-section polisher (JEOL, SM-09010DM) and a focused ion beam system (Hitachi, FB2000A), respectively. After disassembled the cell, the Li metal foil was soaked in ultra-pure water, and the amount of dissolved Mn ions was measured by inductively coupled plasma emission spectroscopy (ICP, Thermo Fisher Scientific, iCAP

6000 SERIES).

5.3 Results and Discussion

5.3.1 Structure and morphology

XRD patterns of uncoated and lithium silicate-coated $LiNi_{0.5}Co_{0.2}Mn_{0.3}O_2$ samples are shown in Fig. 5-1(a). The XRD pattern of each sample was typical of the layered structure of $LiNi_{0.5}Co_{0.2}Mn_{0.3}O_2$. The intensity ratio of the (003) to the (104) peak is known to be a measure of the cation mixing [22]. As shown in Fig. 5-1(a), the degree of cation mixing of both materials was not appreciably different. Besides, neither the crystalline nor amorphous silicates were detected by XRD because of a small amount of lithium silicates (0.5 wt.%). The XRD pattern of the coating powder (without $LiNi_{0.5}Co_{0.2}Mn_{0.3}O_2$) synthesized and calcined in a similar manner is shown in Fig. 5-1(b) in order to estimate the structure of silicates. The diffraction peaks of the coating agent were assigned to those of Li_2SiO_3 and $Li_2Si_2O_5$, suggesting the possibility of Li_2SiO_3 and $Li_2Si_2O_5$ formation on the lithium silicate-coated $LiNi_{0.5}Co_{0.2}Mn_{0.3}O_2$ samples.

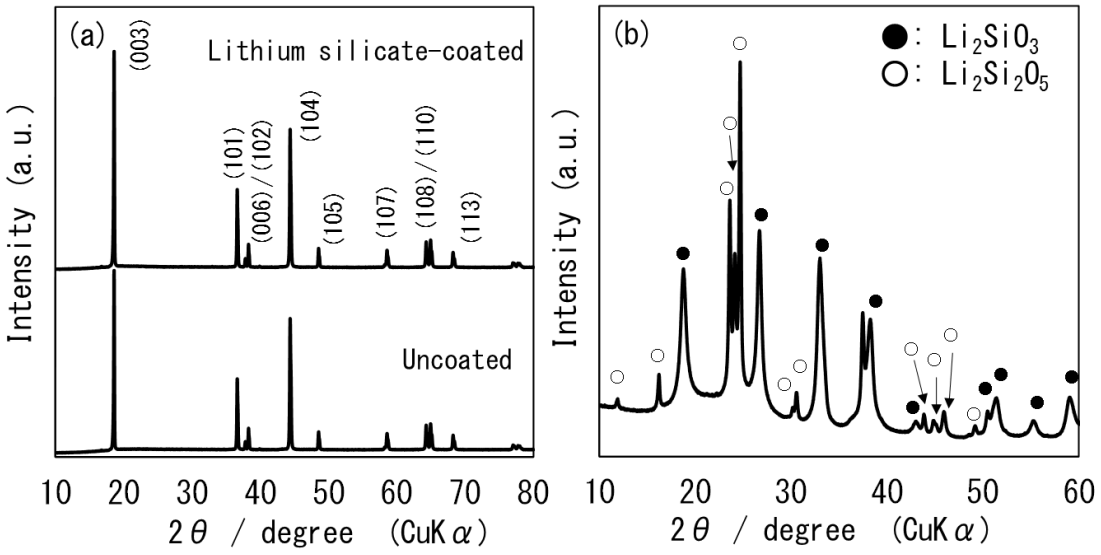

Fig. 5-1 X-ray diffraction patterns of (a) uncoated and lithium silicate-coated $LiNi_{0.5}Co_{0.2}Mn_{0.3}O_2$ and (b) a coating agent (without $LiNi_{0.5}Co_{0.2}Mn_{0.3}O_2$) prepared by the precipitation method.

Fig. 5-2(a) and (b) show the TEM images of the uncoated and the lithium silicate-coated $LiNi_{0.5}Co_{0.2}Mn_{0.3}O_2$ samples. The smooth layer of a few nanometers in thickness was observed on the surface of the lithium silicate-coated $LiNi_{0.5}Co_{0.2}Mn_{0.3}O_2$ particle. From the EDX line analysis, the surface layer was identified with silicate (Fig. 5-2(c)). The signal of Si indicated that Si-rich regions were concentrated not only on the particle surface, but also inside the particle, most probably at grain boundaries. This point is discussed in a later section.

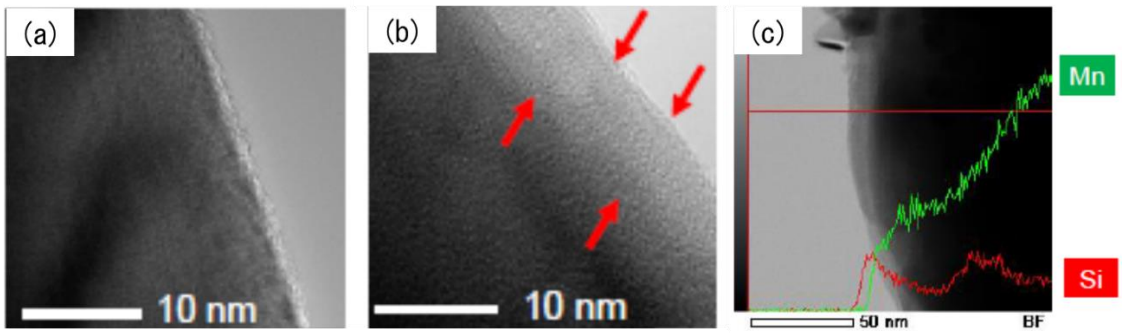

Fig. 5-2 TEM images of (a) uncoated and (b) lithium silicate-coated $LiNi_{0.5}Co_{0.2}Mn_{0.3}O_2$, and (c) line profiles for Mn and Si for the lithium silicate-coated $LiNi_{0.5}Co_{0.2}Mn_{0.3}O_2$.

5.3.2 Charge and discharge properties

Fig. 5-3(a) and (b) show the charge and discharge profiles at a 0.1 C rate between 2.5 and 4.6 V at 30ºC for the uncoated and the lithium silicate-coated $LiNi_{0.5}Co_{0.2}Mn_{0.3}O_2$ samples, respectively. The discharge capacity values and the coulombic efficiency at the first cycle are given in Table 5-1. Both samples gave discharge capacities of around 200 mAh g^{-1} in the initial cycle, which were typical values for the layered Ni-rich lithium transition metal oxide cathodes [1-3]. It is considered that the lithium silicate coating layer synthesized by the antisolvent precipitation method did not inhibit lithium-ion transport. Fig. 5-3(c) shows the variations of specific capacities with cycle number. Both uncoated and coated samples showed similar capacity fading up in the initial 30 cycles. However, the capacity of the uncoated sample decreased more rapidly after 30 cycles than that of the coated sample; that is, the capacity fading on cycling was successfully suppressed for the lithium silicate-coated sample. At the 100^{th} cycle, 81.6% of the initial discharge capacity was obtained for the coated sample, which was about 10% higher than that

obtained for the uncoated sample (71.4%) as shown in Table 5-1. It was shown that the lithium silicate coating using the antisolvent precipitation method is effective for improving the cycle durability of $LiNi_{0.5}Co_{0.2}Mn_{0.3}O_2$. Fig. 5-3(d) shows the variations of coulombic efficiency for the uncoated and lithium silicate-coated sample. The average coulombic efficiencies of the coated and uncoated samples in 100 cycles were 99.4% and 97.8%, respectively. The differential capacity curve ($dQ\ dV^{-1}$) profiles for the coated and uncoated samples were compared by differentiating the 1^{st}, 5^{th}, 50^{th} and 100^{th} charge-discharge curves. Fig. 5-3(e) shows that one peak can be observed corresponding to the one plateau in the charge-discharge curves in Fig. 5-3(a). The peak shift to lower potential and the peak intensity decreases with the cycling. On the other hand, Fig. 5-3(f) shows that the peak intensity in the charge process decreased obviously slower than that of the uncoated sample during the cycling. The result is consistent with the increase in overpotential about the uncoated sample. Fig. 5-3(g) shows the variations of energy efficiency for the uncoated and lithium silicate-coated sample. The energy efficiencies of the coated and uncoated samples at 100^{th} cycle were 93.4% and 87.3%, respectively. This result is consistent with the voltage decay from the charge-discharge curves as shown in Fig. 5-3(a) and Fig. 5-3(b). The variations of capacity retention and average coulombic efficiency revealed that the present coating method effectively suppressed the irreversible decomposition of electrolyte solution.

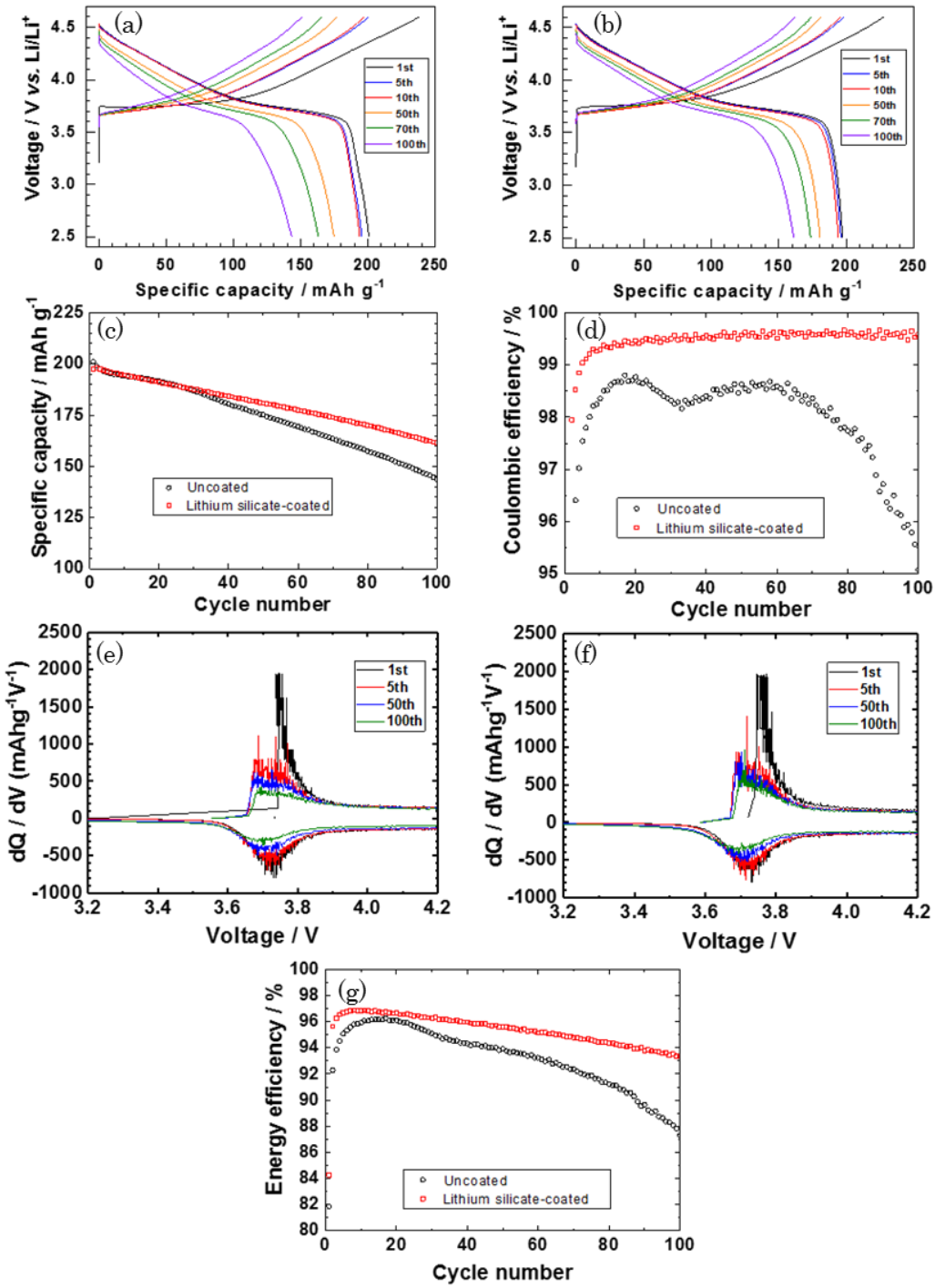

Fig. 5-3 Charge-discharge curves of (a) uncoated and (b) coated $LiNi_{0.5}Co_{0.2}Mn_{0.3}O_2$, and the variations of discharge capacity retention (c) and coulombic efficiency (d). Differential capacity curves in the (e) uncoated and (f) coated $LiNi_{0.5}Co_{0.2}Mn_{0.3}O_2$. The variations of (g) energy efficiency of uncoated and coated $LiNi_{0.5}Co_{0.2}Mn_{0.3}O_2$.

Table 5-1 Discharge capacity, capacity retention and coulombic efficiency of uncoated and lithium silicate-coated $LiNi_{0.5}Co_{0.2}Mn_{0.3}O_2$ at a 0.1 C rate between 2.5 and 4.6 V at 30ºC.

Sample	Discharge capacity at 1st cycle ($mAh \cdot g^{-1}$)	Discharge capacity at 100th cycle ($mAh \cdot g^{-1}$)	Capacity retention (%)	Coulombic efficiency at 1st cycle (%)	Average coulombic efficiency (%)
Uncoated	201	144	71.4	84.3	97.8
Coated	198	161	81.6	86.7	99.4

5.3.3 Manganese ions dissolution as a degradation factor

The dissolution of transition metal ions, especially Mn ions, is one of the degradation factors commonly observed for cathode materials, which is known to be accelerated by HF formed from $LiPF_6$ *via* a hydrolysis reaction [9, 24]. Wu et al. reported another role of lithium silicates; that is, HF and PF_5 are consumed by the addition of Li_2SiO_3 in a carbonate electrolyte [25]. In order to confirm the reactivity of lithium silicates with HF, 1 g of the coating agent (without $LiNi_{0.5}Co_{0.2}Mn_{0.3}O_2$) prepared by the precipitation method was soaked in a mixture of the electrolyte (10 ml) and water (1 ml) and stirred at 60ºC for 10 days as an accelerated test. The solution was filtered to obtain the residue and the filtrate, and the filtrate was dried. XRD patterns of the residue and the dried filtrate

are shown in Fig. 5-4. The residue was mostly Li_2CO_3 with a small amount of $Li_2Si_2O_5$, while the Li_2SiF_6 phase is seen in the dried filtrate. It is clear that Li_2SiF_6 was formed by the reaction of HF and Li_2SiO_3. This fact suggests that lithium silicates prepared by the precipitation method are also effective for removing HF formed in the electrolyte solution.

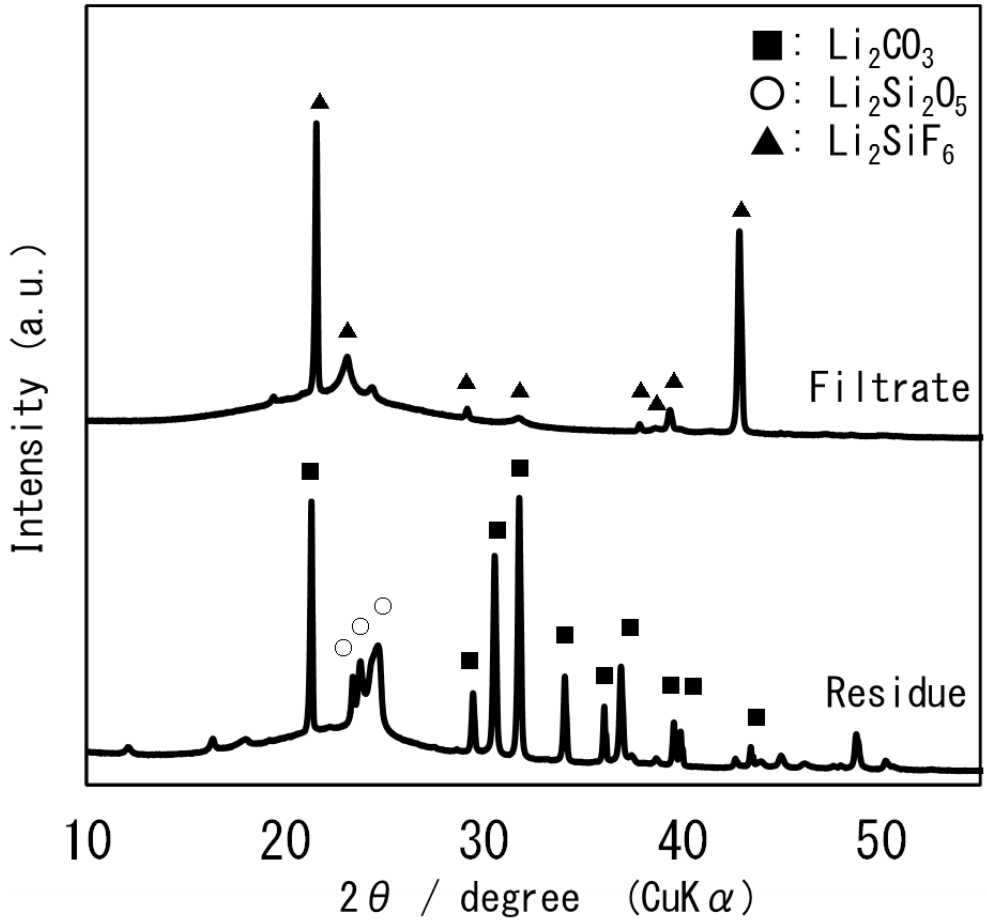

Fig. 5-4 X-ray diffraction patterns of a residue and a dried filtrate of the lithium silicate coating agent after soaked in a mixture of the electrolyte (10 ml) and water (1 ml) for 10 days.

Next the effect of the lithium silicate-coating on Mn dissolution into the electrolyte

was investigated. Charge and discharge tests of the uncoated and coated samples were performed between 2.5 and 4.6 V at a 1 C and at an elevated temperature of 45ºC. After 150th cycle, the cell was disassembled, and the amount of Mn species deposited on the Li counter electrode was measured by ICP. The amounts of dissolved Mn ions from the uncoated and coated samples were 1.84 and 1.42%, respectively, which showed that the lithium silicate coating is effective for the suppression of Mn dissolution during cycling. However, the difference is not appreciably large, and therefore it is reasonable to consider that the main factor of $LiNi_{0.5}Co_{0.2}Mn_{0.3}O_2$ degradation may not be related to transition metal ion dissolution under the experimental conditions in this chapter.

5.3.4 Suppression of crack formation by lithium silicate coating

To understand how the lithium silicate coating improved the capacity retention in more detail, particle morphology changes during cycling were observed by SEM. Fig. 5-5 shows cross-sectional SEM images of the uncoated and coated particles obtained during the cycling. In the uncoated sample after 25 cycles (Fig. 5-5b), cracks were observed along the grain boundaries of the secondary particles, which were not observed before cycling (Fig. 5-5a), and they were extended more significantly after 100 cycles (Fig. 5-5c). On the other hand, crack formation was less significant even after 100 cycles for the lithium silicate-coated sample (Fig. 5-5d). The crack formation is considered to be an important factor for the rapid decrease of the coulombic efficiency after 30 cycles seen in Fig 5-3(c). The electrolyte penetrated into the intergranular cracks inside the particles, and the surface area which is directly in contact with the electrolyte increased. This enhanced irreversible electrolyte decomposition within the particles, and decreased the

coulombic efficiency as shown in Fig. 5-3d. Furthermore the decomposition products accumulated in the intergranular cracks and accelerated the capacity fading as shown in Fig. 5-3c.

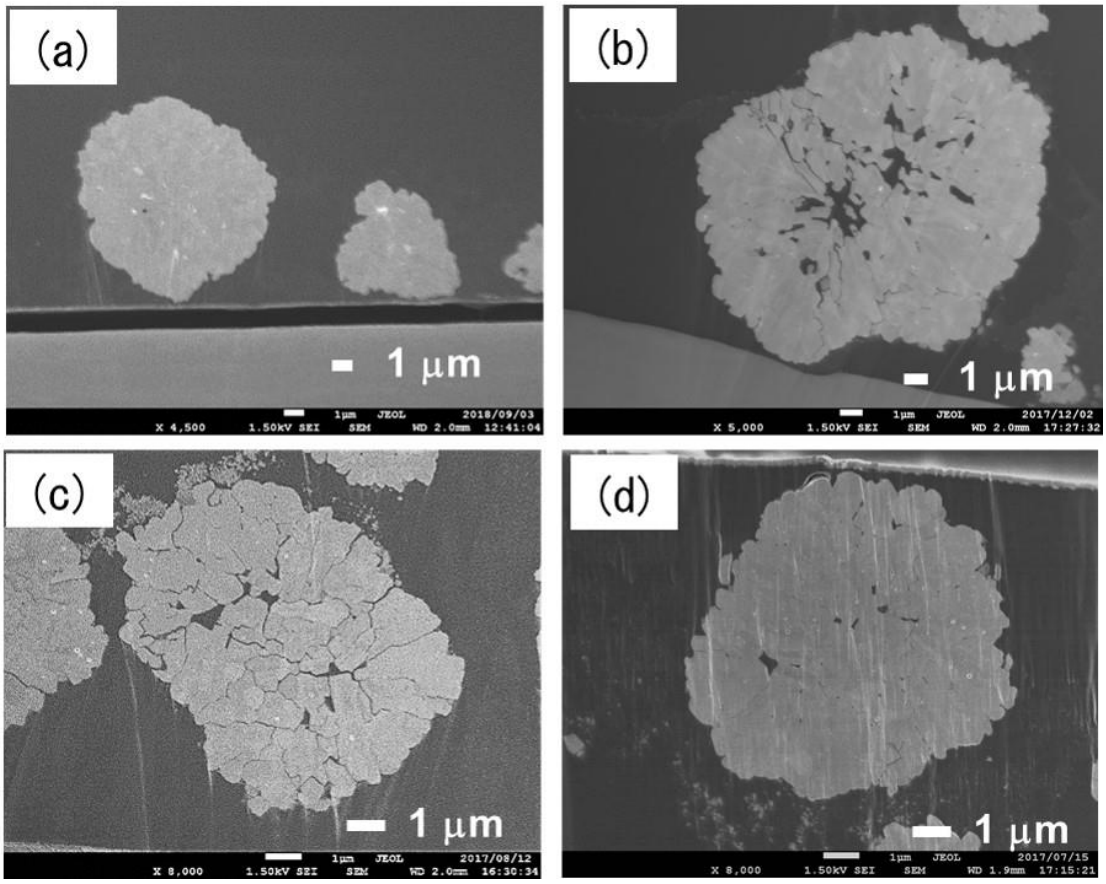

Fig. 5-5 Cross-sectional SEM images of (a, b, c) uncoated and (d) lithium silicate-coated $LiNi_{0.5}Co_{0.2}Mn_{0.3}O_2$ particles (a) before and after (b) 25 and (c, d) 100 cycles at a 0.1 C rate between 2.5 and 4.6 V at 30ºC.

Fig. 5-6 shows the cross-sectional SEM images during accelerated cycling tests at a

1 C rate between 2.5 and 4.6 V at 45ºC, which clearly proved the importance of crack formation in the capacity fading. The uncoated sample showed severely extended cleavages between the grains. On the other hand, the generation of cracks was clearly suppressed in the case of lithium silicate-coated sample. These results clearly indicated that lithium silicate coating suppressed the progress of the cracks.

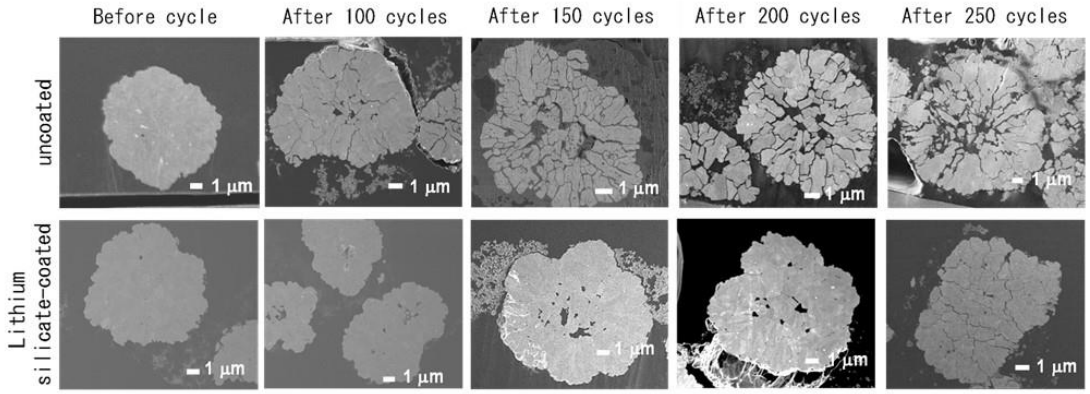

Fig. 5-6 Cross-sectional SEM images before and after 100, 150, 200, 250 cycles of uncoated and lithium silicate-coated $LiNi_{0.5}Co_{0.2}Mn_{0.3}O_2$ during cycling at a 1 C rate between 2.5 and 4.6 V at 45ºC.

In order to evaluate the elementary distribution of Si inside the particle, cross-sectional TEM-EDX analysis was performed for the lithium silicate-coated sample. Si elemental maps are shown in Fig. 5-7. Lithium silicate not only covered the surface of the secondary particles, but also seemed to exist between the grains inside the secondary particles. Fig. 5-8 shows TEM-EDX line profile for Mn and Si elements. It was found Si

element being concentrated at the grain boundaries even at a depth of 400 nm from the surface. Lithium silicates may act as an adhesive and increase the particle strength. In this study, lithium silicates were precipitated on the surface of the secondary particles of $LiNi_{0.5}Co_{0.2}Mn_{0.3}O_2$, but they penetrated within the secondary particles along the grain boundaries when heat-treated at 500°C for 8 h. It should be noted that the penetration of the electrolyte into the cracks may be an important factor to accelerate the capacity fading of $LiNi_{0.5}Co_{0.2}Mn_{0.3}O_2$ as was shown in Fig. 5-6. It is suggested that the presence of the Si-rich regions at the grain boundaries increased the particle strength and suppressed the initial crack formation. The Si-rich regions at the grain boundaries inhibited the intrusion of electrolyte solution inside the secondary particles and prevented the electrolyte decomposition inside the secondary particles, which led to a retard of the crack propagation. Therefore, the capacity retention of $LiNi_{0.5}Co_{0.2}Mn_{0.3}O_2$ was improved by the lithium silicate coating.

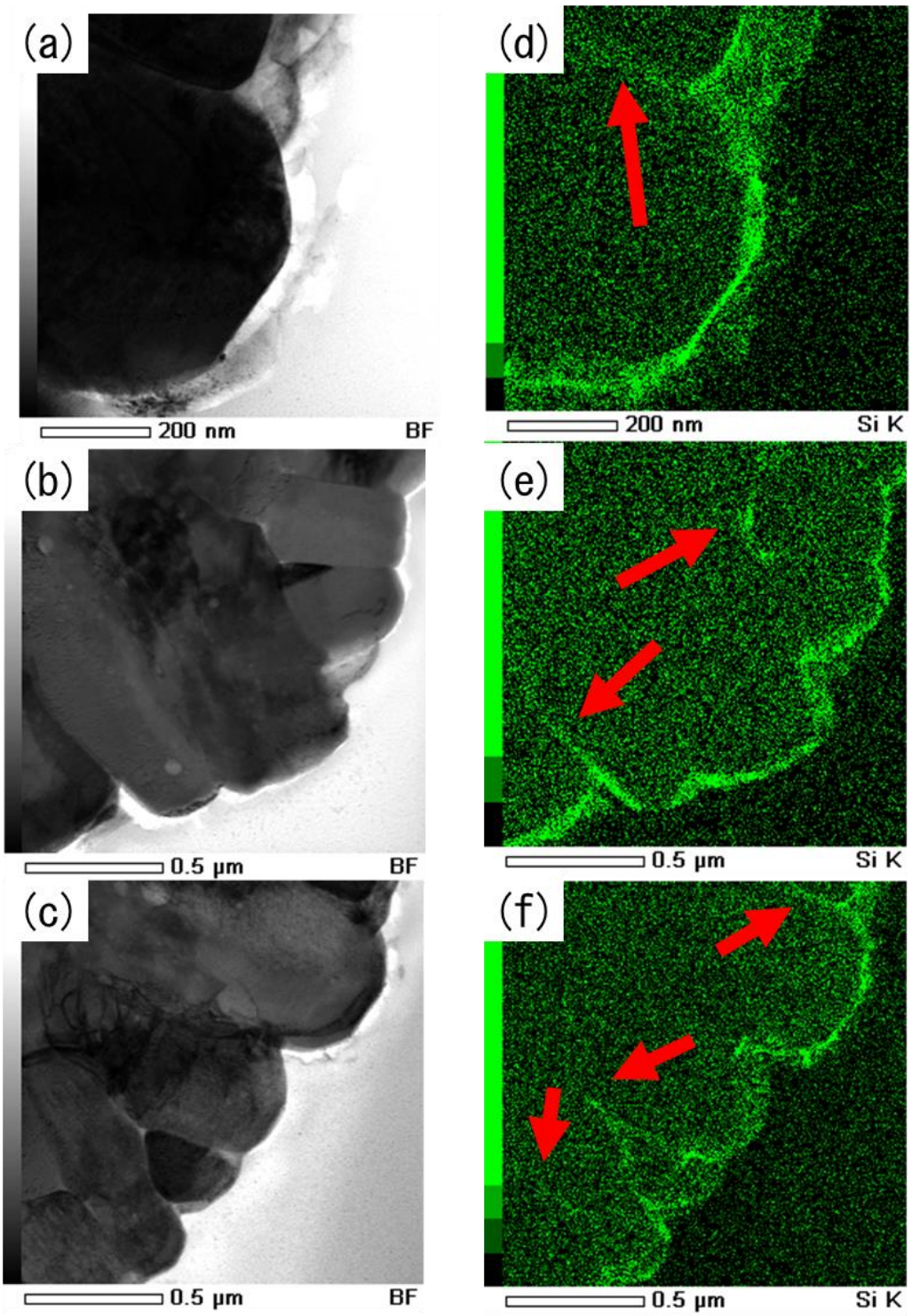

Fig. 5-7 Cross-sectional TEM images of (a, b, c) lithium silicate-coated $LiNi_{0.5}Co_{0.2}Mn_{0.3}O_2$, and cross-sectional TEM-EDX elemental maps for (d, e, f) Si in coated $LiNi_{0.5}Co_{0.2}Mn_{0.3}O_2$. Arrows indicate Si-rich regions at the grain boundaries.

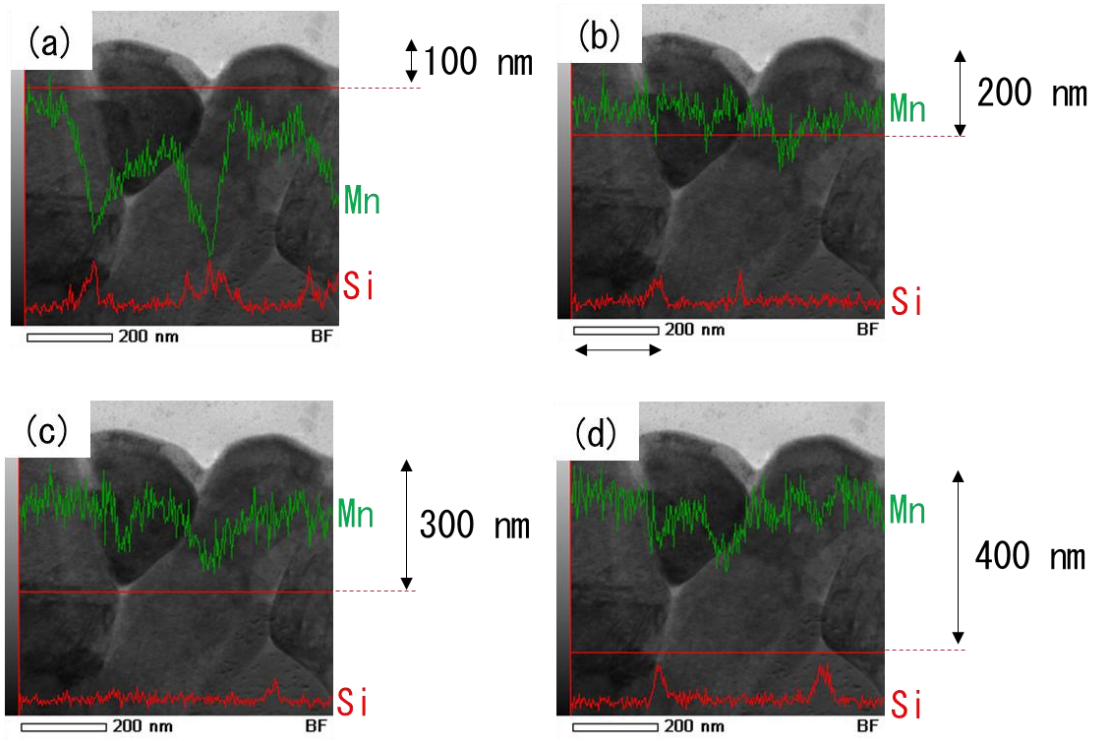

Fig. 5-8 Cross-sectional TEM-EDX line profile for Si in lithium silicate-coated $LiNi_{0.5}Co_{0.2}Mn_{0.3}O_2$ at depths of (a) 100, (b) 200, (c) 300, and (d) 400 nm from the surface of the secondary particle.

5.4 Conclusions

$LiNi_{0.5}Co_{0.2}Mn_{0.3}O_2$ coated with lithium silicates was prepared by a precipitation method and their charge and discharge characteristics as cathodes in lithium-ion batteries were investigated. The $LiNi_{0.5}Co_{0.2}Mn_{0.3}O_2$ particles were coated with a thin layer of lithium silicates consisting of Li_2SiO_3 and $Li_2Si_2O_5$. The capacity fading on cycling was successfully suppressed for the lithium silicate-coated sample. The coulombic efficiency of the coated sample was higher than that of the uncoated sample, and approached a steady-state above 99.5%. During cycling, cracks were formed along the grain boundaries of the secondary particles, which were not observed before cycling. On the other hand, the generation and propagation of cracks were significantly suppressed for the lithium silicate-coated sample. TEM-EDX analysis indicated the presence of Si-rich regions along the grain boundaries inside the secondary particles. This result suggested that the lithium silicate coating suppressed not only the irreversible decomposition of electrolyte solution on the particle surface, but also the crack formation followed by the electrolyte decomposition at the resulting intergranular cracks inside the particles. Therefore lithium silicate coating is an effective way for improving the cycleability of $LiNi_{0.5}Co_{0.2}Mn_{0.3}O_2$ cathode.

References

[1] P. Yan, J. Zheng, M. Gu, J. Xiao, J.-G. Zhang, C.-M. Wang, Nat. Commun. 8 (2017) 14101.

[2] S.-K. Jung, H. Gwon, J. Hong, K.-Y. Park, D.-H. Seo, H. Kim, J. Hyun, W. Yang, K. Kang, Adv. Energy Mater. 4 (2014) 1300787.

[3] K. Ishidzu, Y. Oka, and T. Nakamura, Solid State Ionics 288 (2016) 176.

[4] H.-J. Noh, S. Youn, C. S. Yoon, and Y.-K. Sun, J. Power Sources 233 (2013) 121.

[5] F. Lin, L. M. Markus, D. Nordlund, T.-C. Weng, M. D. Asta, H. L. Xin, M. M. Doeff, N. Commun. 5 (2014) 3529.

[6] M. Borner, F. Horsthemke, F. Kollmer, S. Haseloff, A. Friesen, P. Niehoff, S. Nowak, M. Winter, F. M. Schappacher, J. Power Sources 335 (2016) 45.

[7] S. Hashigami, M. Kawanishi, K. Yoshimi, S. Ujiie, T. Inagaki, M. Hashinokuchi, T. Doi, M. Inaba, Electrochemistry 84 (2016) 842.

[8] C.-H. Shen, Q. Wang, H.-J. Chen, C.-G. Shi, H.-Y. Zhang, L. Huang, J.-T. Li, S.-G. Sun, ACS Appl. Mater. Interfaces 8 (2016) 35323.

[9] D. Arumugam, G. P. Kalaignan, J. Electroanal. Chem. 624 (2008) 197.

[10] Y. Fan, J. Wang, Z. Tang, W. He, J. Zhang, Electrochim. Acta 52 (2007) 3870.

[11] L. Liang, G. Hu, F. Jiang, Y. Cao, J. Alloys Comp. 657 (2016) 570.

[12] E. Zhao, M. Chen, Z. Hu, D. Chen, L. Yang, X. Xiao, J. Power Sources 343 (2017) 345.

[13] B. Seteni, N. Rapulenyane, J. C. Ngila, S. Mpelane, H. Luo, J. Power Sources 353 (2017) 210.

[14] G. H. Waller, P. D. Brooke, B. H. Rainwater, S. Y. Lai, R. Hu, Y. Ding, F. M. Alamgir,

K. H. Sandhage, M. L. Liu, J. Power Sources 306 (2016) 162.

[15] Y. Shi, M. Zhang, D. Qian, Y. S. Meng, Electrochim. Acta 203 (2016) 154.

[16] J.-Z. Kong, S.-S. Wang, G.-A. Tai, L. Zhu, L.-G. Wang, H.-F. Zhai, D. Wu, A.-D. Li, H. Li, J. Alloys Comp. 657 (2016) 593.

[17] L. Yu, X. Qiu, J. Xi, W. Zhu, L. Chen, Electrochim. Acta 51 (2006) 6406.

[18] K. Liu, G.-L. Yang, Y. Dong, T. Shi, and L. Chen, J. Power Sources 281 (2015) 370.

[19] J. S. Chae, S. B. Yoon, W. S. Yoon, Y. M. Kang, S. M. Park, J. W. Lee, K. C. Roh, J. Alloys Comp. 601 (2014) 217.

[20] D. Wang, X. Li, Z. Wang, H. Guo, X. Chen, X. Zheng, Y. Xu, J. Ru, Electrochim. Acta 174 (2015) 1225.

[21] S. Tan, L. Wang, L. Bian, J. Xu, W. Ren, P. Hu, A. Chang, J. Power Sources 277 (2015) 139.

[22] S.-H. Han, J. H. Song, T. Yim, Y.-J. Kim, J.-S. Yu, S. Yoon, J. Electrochem. Soc. 163 (2016) A748.

[23] Y. J. Hong, S. H. Choi, C. M. Sim, J.-K. Lee, Y. C. Kang, Mater. Res. Bull. 47 (2012) 4359.

[24] L. F. Wang, C. C. Ou, K. A. Striebel, J. S. Chenc, J. Electrochem. Soc. 150 (2003) A905.

[25] B. Wu, Y. Ren, D. Mu, X. Liu, F. Wu, Electrochim. Acta 143 (2014) 324.

CHAPTER 6

Surface Modification of Spray Pyrolyzed $LiNi_{0.5}Co_{0.2}Mn_{0.3}O_2$ Cathode Particles with Lithium Boron Oxide

6.1 Introduction

Rechargeable lithium-ion batteries (LIBs) have been widely used not only in portable electronic devices, but also in automobiles including plug-in hybrid vehicles (PHEVs) and electric vehicles (EVs) due to their high energy density. The development of electrode materials with high energy density is indispensable to meet a variety of demands such as high specific capacity, low cost, and long cycle life [1]. Layered lithium transition metal oxide $LiNi_{1-x-y}Co_xMn_yO_2$ has attractive electrochemical properties, which can be varied with the composition of Ni, Co and Mn in the structure, as a cathode. Although increasing the content of Ni raises the specific capacity, it deteriorates the capacity retention and the thermal stability [2]. High cost Co also affects the capacity, and offers an increased electronic conductivity, whereas Mn contributes to the structural stability and thereby safety. The most well-known composition is $LiNi_{1/3}Co_{1/3}Mn_{1/3}O_2$, which has been already used in commercially available LIBs because it has well-balanced charge/discharge properties as a cathode with a capacity of around 150 mAh g^{-1} between 2.5 and 4.2 V [3].

Recently Ni-rich layered lithium transition metal oxide $LiNi_{1-x-y}Co_xMn_yO_2$ has attracted much attention for further increasing that capacity. $LiNi_{0.5}Co_{0.2}Mn_{0.3}O_2$ is

considered one of the most promising cathodes because it offers a high capacity of around 200 $mAh \cdot g^{-1}$ by raising the cut-off potential to 4.5-4.6 V vs. Li^+/Li on charging [4]. However, the high content of Ni and the high cut-off potential result in poor cycle performance. Many studies have been reported on the degradation factors for the capacity fading of the Ni-rich layered materials, which include the decomposition of electrolytes and the irreversible structural transformations to the spinel and rock salt phases on the particle surface [4-7]. The dissolution of transition metal ions from active materials is also considered as a degradation factor [7, 8]. In order to mitigate these problems, coating of the surface of $LiNi_{0.5}Co_{0.2}Mn_{0.3}O_2$ with oxides has been investigated [9-13].

Crack formation inside the secondary particles has been recently recognized as a severe degradation factor, which is caused by a volume change of the material upon lithium ion extraction and reinsertion [14-17]. The layered cathode materials are usually granulated to reduce the surface area and to improve the packing density in the electrode. The size of commercially available cathode materials is typically around 10 μm [7, 17]. However, the granulation causes stress due to the larger expansion and shrinkage during charge and discharge cycling, and the crack formation of the Ni-rich cathode materials becomes significant. The cracks disconnect the electrical pathway among the grains in a secondary particle. In addition, the irreversible reactions of electrolyte decomposition should occur within the cracks, and as a result they accelerate the deterioration of the charge/discharge properties.

In Chapter 6, the layered $LiNi_{0.5}Co_{0.2}Mn_{0.3}O_2$ was synthesized by a spray pyrolysis method. The particles prepared by spray pyrolysis have some advantages such as narrow particle size distribution, high purity, and easy control in composition and morphology of multi-component metal oxides [18]. Since spray pyrolyzed particles are small in the range

of 100 nm - 2 μm, it is expected that the crack formation is less likely to occur due to a small stress induced inside the secondary particles. On the other hand, the surface of small particles needs to be protected because of their large surface area. Hence the spray pyrolyzed $LiNi_{0.5}Co_{0.2}Mn_{0.3}O_2$ particles were coated with lithium boron oxide (LBO) by an antisolvent precipitation method [19] and the charge and discharge properties of the cathodes were investigated. LBO was selected because it has lithium-ion conductivity. The cathodes at the charged and discharged states after the charge/discharge tests were analyzed by synchrotron-based hard x-ray photoelectron spectroscopy (HAXPES) to obtain information on the structural transformations and the decomposition of the electrolyte as degradation factors.

6.2 Experimental

6.2.1 Preparation of the $LiNi_{0.5}Co_{0.2}Mn_{0.3}O_2$ particles by spray pyrolysis

Stoichiometric amounts of lithium nitrate (99.9%, Wako Pure Chemical Industries, Ltd.), manganese nitrate hexahydrate (99.9%, Wako Pure Chemical Industries, Ltd.), nickel nitrate hexahydrate (99.9%, Wako Pure Chemical Industries, Ltd.) and cobalt nitrate hexahydrate (99.0%, Wako Pure Chemical Industries, Ltd.) were weighed to prepare 0.25 mol of $LiNi_{0.5}Co_{0.2}Mn_{0.3}O_2$ and were dissolved in 500 mL of deionized water. The solution was stirred for 2 hours, diluted with deionized water to 1 L, and was used for spray pyrolysis. The apparatus of spray pyrolysis was described in Chapter 2 [20]. The solution was atomized using ultrasonic vibrators with an oscillation frequency of 1.65 MHz in an atomizing vessel. Because the ultrasonic vibrators raise the temperature of the solution during atomizing, cold water was circulated around the atomizing vessel to keep the temperature of the solutions lower than 30ºC. This is because atomization at a high temperature tends to give inhomogeneous droplets. The reaction furnace consisted of four independent heating zones, whose temperatures were set at 200, 400, 800, and 800ºC from the inlet to the outlet. The atomized mists were flown into an alumina tube in the furnace area with 1 L min^{-1} of air. The droplets including lithium and the transition metal ions were dried, decomposed, reacted, and sintered when passing through the reaction furnace. The powder was collected using a membrane filter and was heat-treated at 850ºC for 8 hours in air.

6.2.2 Coating procedure of $LiNi_{0.5}Co_{0.2}Mn_{0.3}O_2$ with lithium boron oxide

LBO was coated on the surface of the $LiNi_{0.5}Co_{0.2}Mn_{0.3}O_2$ powder *via* an antisolvent precipitation method [19]. Lithium metaborate $LiBO_2$ (Wako Pure Chemical Industries, Ltd.) was added to ultra-pure water so as to be 2 or 5 wt.% with respect to $LiNi_{0.5}Co_{0.2}Mn_{0.3}O_2$. This suspension was allowed to stand overnight at 45ºC and $LiBO_2$ was completely dissolved in aqueous solution. $LiNi_{0.5}Co_{0.2}Mn_{0.3}O_2$ powder prepared by spray pyrolysis was added to the lithium borate solution followed by stirring at 50ºC. Then ethanol as an antisolvent was added dropwisely to the suspension with vigorous stirring. LBO was precipitated out on the $LiNi_{0.5}Co_{0.2}Mn_{0.3}O_2$ by a poor solubility in ethanol. The precipitate was filtered and dried at 60ºC for 12 h. Then, the powder was annealed at 500ºC for 8 h to obtain lithium borate-coated $LiNi_{0.5}Co_{0.2}Mn_{0.3}O_2$. The 2 and 5 wt.% coated samples were hereafter referred to as 2 and 5 wt.% LBO-NCM, respectively.

6.2.3 Cell fabrication and charge/discharge tests

A cathode slurry was prepared by mixing the oxide powder (80 wt.%), an acetylene black conductor (Denka Co., Ltd., 10 wt.%), a polyvinylidene difluoride binder (PVDF, Kureha Corp., 10 wt.%) using 1-methyl-2-pyrrolidinone (Wako Pure Chemical Industries, Ltd.) as a solvent. The slurry was cast by the doctor blade method on an Al foil current collector (20 μm thickness), and then dried at 80ºC for 18 h under vacuum. The sheet was punched into circular disks having a diameter of 13 mm as cathodes. The loading of the cathode was typically 2.0 mg cm^{-2}.

Charge and discharge tests were carried out using two electrode cells, which were assembled in an Ar-filled glove box (Miwa Manufacturing Co., Ltd., MDB-1NKP-DS).

Li metal foil (Honjo Metal) was used as a counter electrode, and a microporous polypropylene monolayer membrane (Celgard® 2400) was used as a separator. The electrolyte solution was 1 M $LiPF_6$ dissolved in a 1:2 (by volume) mixture of ethylene carbonate (EC) and dimethyl carbonate (DMC) (Kishida Chemical Co., Ltd., Battery Grade). The charge and discharge tests were performed galvanostatically at a 1 C rate (1 C = 200 mAh g^{-1}) between 2.5 and 4.5 V at 30ºC using a TOSCAT-3100 battery test system (TOYO SYSTEM CO., LTD.). The rate capability tests were performed in the voltage range of 2.5-4.5 V at 0.1, 0.2, 0.5, 1, 2, 5 and 10 C for three cycles each. The electrochemical impedance spectroscopy (EIS) was measured using a three-electrode cell over the frequency range of 100 kHz to 0.1 Hz at 3.8 V during the charging in the 2, 15 and 30^{th} cycle at 30ºC.

6.2.4 Characterization

The crystal structure of the $LiNi_{0.5}Co_{0.2}Mn_{0.3}O_2$ powders uncoated and coated with LBO was investigated by X-ray diffraction (XRD, Shimadzu XRD-6000) using Cu Kα radiation. The morphology of the oxide particles was observed with a scanning electron microscope (SEM, JSM-7001FD) and a transmission electron microscope (TEM, JEM-2100F). The oxide particles were embedded in a polymer resin, and samples for SEM observation were prepared by a cross-section polisher (JEOL, SM-09010DM). After disassembled the cell, the Li metal foil was soaked in ultra-pure water, and the amount of dissolved transition metal ions were measured by inductively coupled plasma emission spectroscopy (ICP, Thermo Fisher Scientific, iCAP 6000 SERIES). HAXPES measurements were carried out at the BL16XU beam line at SPring-8 in Japan. The

excitation energy was 7947 eV and the pass energy was set to 200 eV. The binding energies of the HAXPES spectra were calibrated by the carbon binding energy (284.6 eV) and the peak intensities were normalized by the intensity of the main peak of each element.

6.3 Results and Discussion

6.3.1 Structure and morphology of LBO-NCM prepared by spray pyrolysis

XRD patterns of uncoated NCM, 2 wt.% LBO-NCM and 5 wt.% LBO-NCM prepared by spray pyrolysis were shown in Fig. 6-1. The XRD pattern of each sample was typical of the $LiNi_{0.5}Co_{0.2}Mn_{0.3}O_2$ layered structure. The diffraction peak intensity ratio *R* of the (003) to the (104) peak is known to be a measure of the cation mixing [21]. The *R* values of uncoated NCM, 2 wt.% LBO-NCM and 5 wt.% LBO-NCM were 0.91, 0.86 and 0.86, respectively. The *R* values decreased by the coating of LBO. This may be due to partial occupation of small-sized boron ions in lithium positions within the layered structure [21]. It was also considered that part of Li ions in $LiNi_{0.5}Co_{0.2}Mn_{0.3}O_2$ was consumed to form LBO. On the other hand, crystalline borates were not detected by XRD. This result indicated that LBO compounds may exist as an amorphous state.

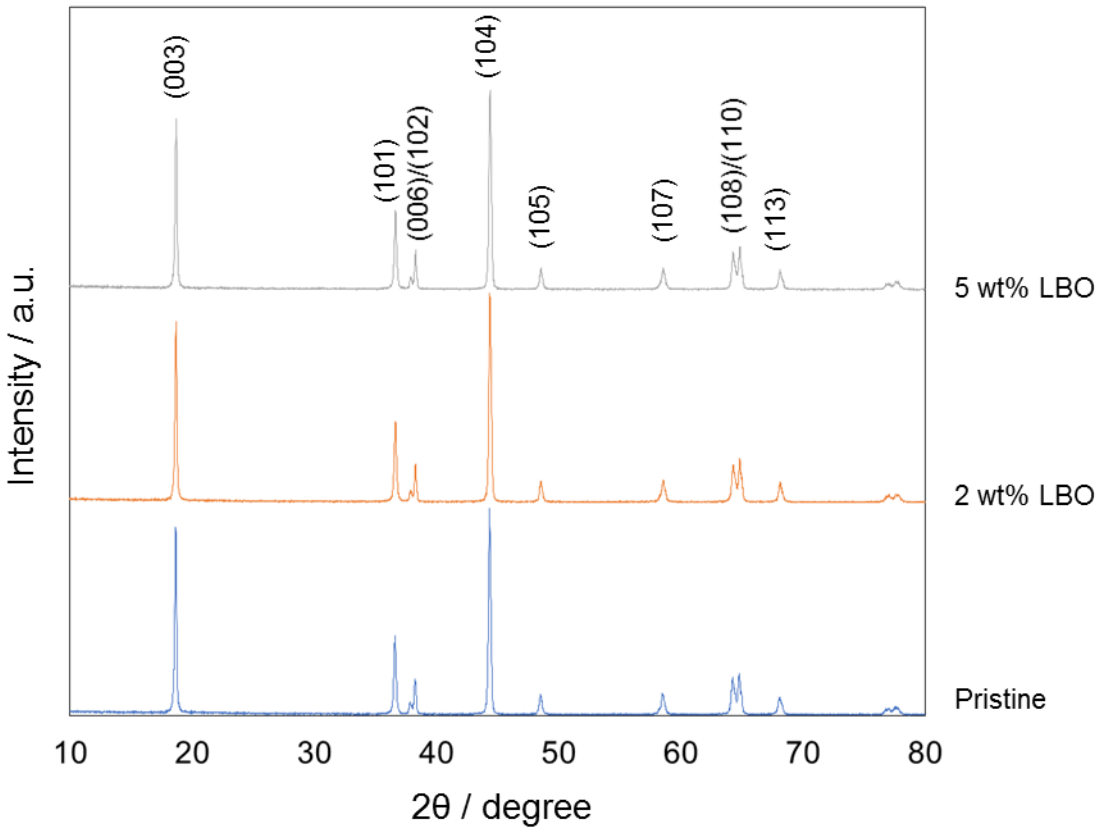

Fig. 6-1 X-ray diffraction patterns of spray pyrolyzed $LiNi_{0.5}Co_{0.2}Mn_{0.3}O_2$ particles coated with 0, 2 and 5 wt.% LBO by an antisolvent precipitation method.

Figs. 6-2(a)-(f) show SEM images of uncoated NCM, 2 wt.% LBO-NCM and 5 wt.% LBO-NCM. The particles were not agglomerated and their diameter was distributed in the range of 500 nm to 1 μm for each sample. The secondary particles consisted of primary particles of about 100 nm in diameter. The particle shape and size were not appreciably changed by LBO coating. Figs. 6-2(g)-(j) show TEM images of 2 and 5 wt.% LBO-NCMs. The smooth and uniform thin layer of LBO with a thickness of 10 nm was

observed on the surface of both samples. The spray pyrolysis method usually gives spherical particles with a void inside; however, void-free non-spherical particles were obtained in the present study. The dense structure of the particles is favorable because the cathode/electrolyte interfaces are protected effectively by the LBO coating.

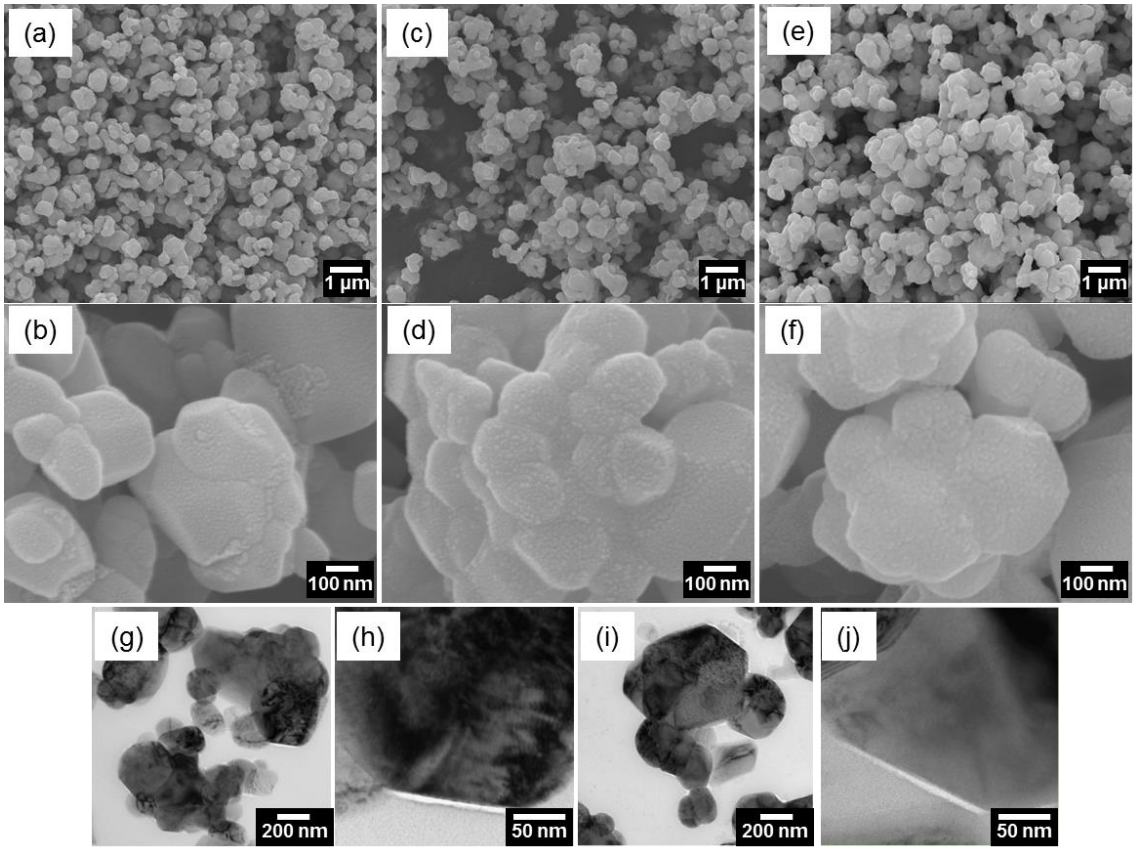

Fig. 6-2 SEM images of $LiNi_{0.5}Co_{0.2}Mn_{0.3}O_2$ particles coated with (a, b) 0 wt.%, (c, d) 2 wt.% and (e, f) 5 wt.% LBO. TEM images of $LiNi_{0.5}Co_{0.2}Mn_{0.3}O_2$ particles coated with (g, h) 2 wt.% and (I, j) 5 wt.% LBO.

In order to confirm the formation of LBO at the surface of the particles, HAXPES was measured as shown in Fig. 6-3. From the HAXPES B 1s spectra in Fig. 6-3(a), a boron component with a binding energy of around 193 eV was detected for both LBO-NCM samples. In Fig. 6-3(b), the O 1s peak around 529 eV is assigned to the lattice oxygen. Another peak at around 532 eV indicates absorbed oxygen on the surface after coating due to the presence of LBO. These results indicated that LBO coating layer was formed on the $LiNi_{0.5}Co_{0.2}Mn_{0.3}O_2$ surface by the antisolvent precipitation method.

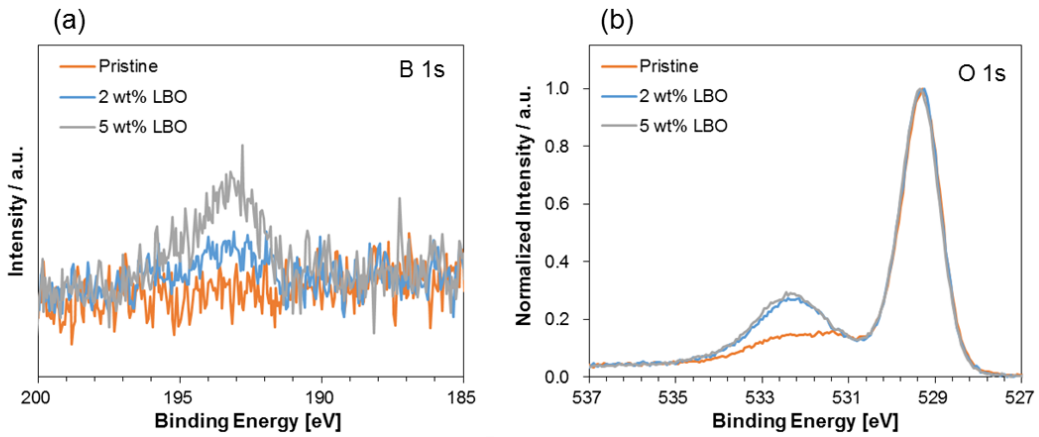

Fig. 6-3 (a) B 1s and (b) O 1s HAXPES spectra of uncoated NCM, 2 wt.% LBO-NCM and 5 wt.% LBO-NCM.

6.3.2 Charge and discharge properties

The discharge curves at various rates for uncoated NCM, 2 wt.% LBO-NCM and 5 wt.% LBO-NCM are shown in Figs. 6-4 (a)-(c). All samples provided discharge capacities higher than 190 mAh g^{-1} at 0.1 C between 2.5 and 4.5 V, which are typical

values for the layered lithium transition-metal oxide $LiNi_{0.5}Co_{0.2}Mn_{0.3}O_2$ cathodes. The discharge capacity of the uncoated sample rapidly decreased with increasing the discharge rate, whereas the LBO-coated samples were capable of maintaining a higher discharge capacity. For the uncoated sample, larger overpotential was observed. The uncoated sample showed no capacity at 5 and 10 C rates because the charging was immediately terminated by reaching the upper cut-off potential of 4.5 V (Fig. 6-4 (a)). On the other hand, 2 and 5 wt.% LBO-NCM samples showed 57 and 80 mAh g^{-1}, respectively, even at a high rate of 10 C. These results suggest that the coating material promotes the charge/discharge reaction rates at the electrode/electrolyte interface.

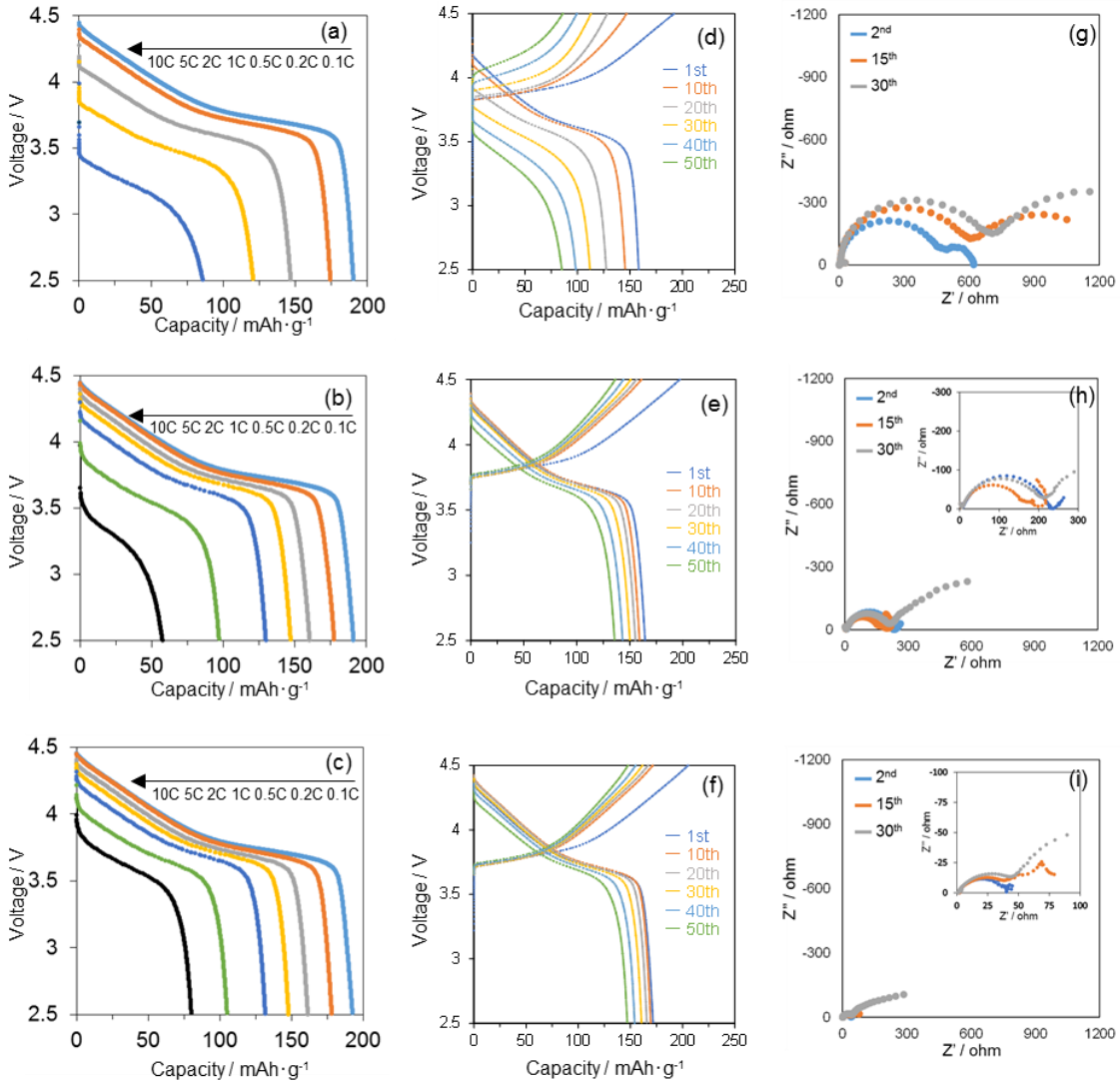

Fig. 6-4 Discharge curves (a-c) at various C-rates between 2.5-4.5 V, charge-discharge curves (d-f) at 1 C between 2.5-4.5 V, and Nyquist plots (g-i) obtained at 3.8 V during the charging in the 2, 15, and 30th cycle for (a, d, g) uncoated NCM, (b, e, h) 2 wt.% LBO-NCM, and (c, f, i) 5 wt.% LBO-NCM in 1 M $LiPF_6$/EC+DMC (1:2) at 30^{o}C.

Figs. 6-4 (d)-(f) compare the charge-discharge curves during charge/discharge cycling tests for the uncoated and the LBO-coated $LiNi_{0.5}Co_{0.2}Mn_{0.3}O_2$ samples. The discharge capacity of the uncoated sample declined rapidly. The capacity retentions at the 50th cycle of uncoated NCM, 2 wt.% LBO-NCM and 5 wt.% LBO-NCM were 53.8%, 82.5% and 85.6%, respectively, which shows that the capacity retention was highly improved by LBO coating. The coulombic efficiency of both LBO-coated samples was 99.6% at 50 cycle, which was higher than that of uncoated sample (98.9%). Therefore, the lithium borate coating is effective for improving the cycleability of $LiNi_{0.5}Co_{0.2}Mn_{0.3}O_2$ as well as suppressing side reactions at the cathode/electrolyte interface.

Figs. 6-4 (g)-(i) show Nyquist plots of uncoated NCM, 2 wt.% LBO-NCM and 5 wt.% LBO-NCM obtained at 3.8 V during the charging in the 2, 15, and 30^{th} cycle. The intersection between the real axis and the higher-frequency arc is generally attributed to the ohmic resistance of the electrolyte. The higher-frequency arc is assigned to the contact resistance at the interface among the active materials and conducting carbon particles, which should be increased by the formation of an insulating solid electrolyte interphase and decomposition products of organic compounds on the surface. The lower frequency arc is assigned to the lithium ion transfer resistance (charge transfer resistance) between the electrode and the electrolyte. The impedance spectra of the three samples were remarkably different even in the 2^{nd} cycle, which reflects the difference in the structure of the NCM particle/electrolyte interface formed during the first cycle. The LBO coating effectively reduced the impedance of the electrode. It was also revealed that the increase of resistances estimated from the lower and higher frequency arcs was significantly suppressed by the LBO coating during cycling. These results clearly indicate that the

oxidative decomposition of the electrolyte and the resulting inactivation of the particle surface are suppressed by the LBO coating.

6.3.3 Characterization after cycling

The effect of the LBO-coating on the dissolution of transition metal ions into the electrolyte was investigated. Charge and discharge tests of uncoated NCM, 2 wt.% LBO-NCM and 5 wt.% LBO-NCM were performed between 2.5 and 4.5 V at 1 C at 30ºC. After 30 cycles, the cells were disassembled, and the amount of transition metal ions deposited on the Li counter electrode was measured by ICP. The amounts of dissolved Mn ions from uncoated NCM, 2 wt.% LBO-NCM and 5 wt.% LBO-NCM were 0.33, 0.20 and 0.22%, respectively. The amounts of dissolved Ni ions were 0.69, 0.67 and 0.55%, respectively, and those of dissolved Co ions were 0.23, 0.08 and 0.12%, respectively. These results showed that the LBO coating is effective for the suppression of transition metal ions dissolution during cycling.

TEM images of 5 wt.% LBO-NCM after 50 cycles are shown in Figs. 6-5(a) and (b). The morphology of the LBO coating layer was not changed from that before cycling and it was presumed that most of the coating material remained on the surface of $LiNi_{0.5}Co_{0.2}Mn_{0.3}O_2$ particles. It was therefore considered that the surface of $LiNi_{0.5}Co_{0.2}Mn_{0.3}O_2$ particles was effectively protected from the side reactions by the stable LBO coating layer during cycling.

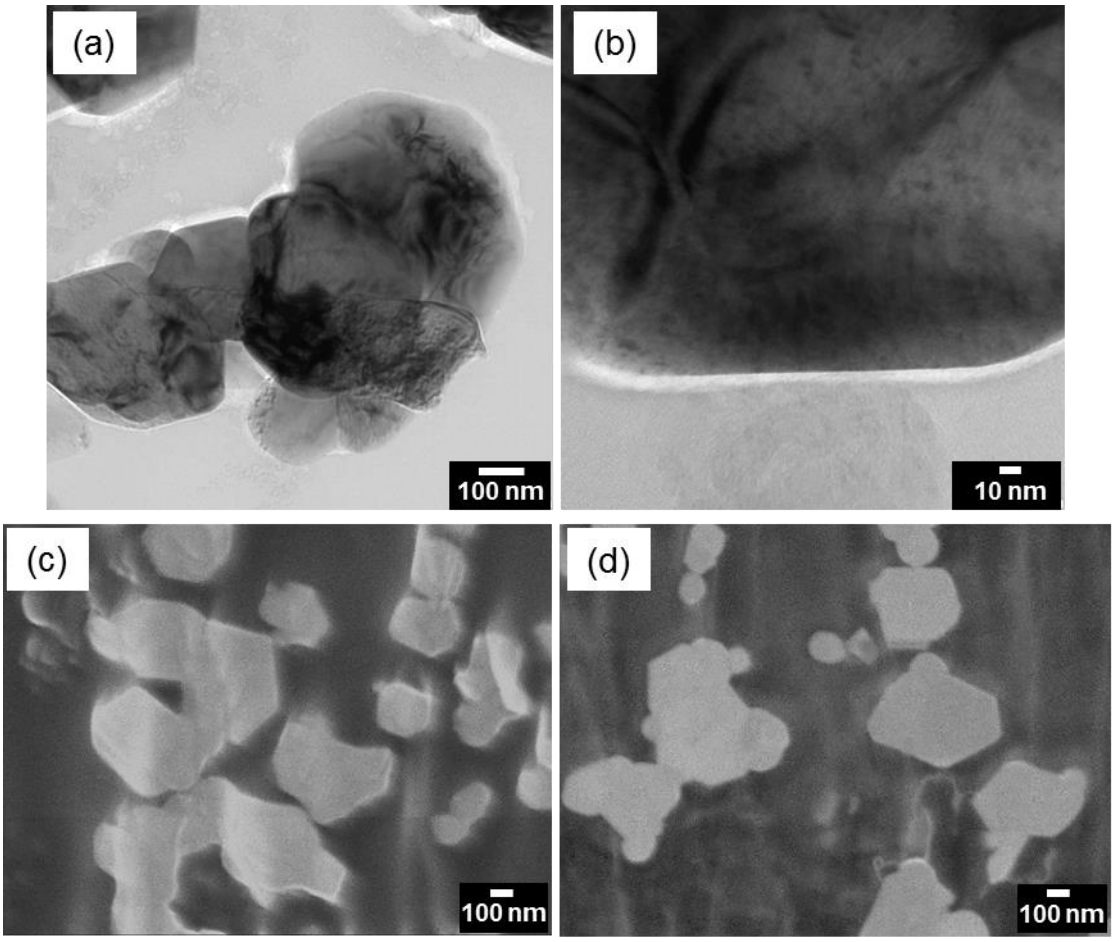

Fig. 6-5 TEM images (a, b) of $LiNi_{0.5}Co_{0.2}Mn_{0.3}O_2$ particles coated with 5 wt.% of LBO after 50 cycles, and cross-sectional SEM images of (c) uncoated NCM and (d) 5 wt.% LBO-NCM after 50 cycles.

The cross-sectional SEM images of the uncoated NCM and 5 wt.% LBO-NCM after 50 cycles are shown in Figs. 6-5 (c) and (d). Crack-free cross sections were maintained for both samples after 50 cycles. These results indicated that the suppression of crack formation is less likely to be the reason why the LBO coating improved the cycleability shown in Fig. 6-4. This is reasonable because the spray pyrolyzed particles are less than 1 μm in the present study. Consequently, the crack formation can be excluded from the

major degradation factor of spray pyrolyzed NCM prepared in the present study, though it is an important degradation factor of commercially available NCM cathode materials with a larger particle diameter (typically 10 μm) [17, 19, 22].

6.3.4 Hard X-ray photoelectron spectroscopy

In order to investigate the cathode surface chemistry, HAXPES spectra were measured for uncoated NCM and 5 wt% LBO-NCM. HAXPES C 1s, O 1s and F 1s spectra obtained at the fully 4.5 V charged state after the 1st and 50th charge-discharge cycle are displayed in Fig. 6-6. B 1s and P 2s spectra were also measured, but are not shown here because the peaks were overlapped and the P 2p peaks were very weak. In the C 1s spectrum of the uncoated sample, a peak at 284.6 eV characteristic of conductive carbon and another peak at 290.4 eV assigned to the PVDF binder were observed [22]. In the O 1s spectrum of the uncoated sample, a peak at 529.1 eV is characteristic of lattice oxygen, and a broad peak at 531.5-533.5 eV is assigned to lithium carbonate [23]. No obvious changes were observed in these spectra for 5 wt% LBO-NCM after the 1st cycle and for both samples after 50 cycles although there was a little change for the peak at 531.5-533.5 eV in the O 1s spectra. The peaks at 531.5-533.5 eV are assigned to C−O and C=O species on the surface of the cathode particles, which is consistent with electrolyte decomposition products formed on the particle surface.

In F 1s spectra, a peak assigned to LiF and a peak assigned to PVDF and $LiPF_6$ species were observed at 685.0 and 687.5 eV, respectively [23]. In the case of the uncoated sample, the peak intensity of LiF strongly increased after 50 cycle, while the increase was slightly suppressed for 5 wt% LBO-NCM. This result suggested that the LBO coating

suppressed the formation of LiF, which originates from oxidative decomposition of the electrolyte salts during cycling. From these results, it is concluded that the LBO coating is effective for suppressing oxidative decomposition of the solvents and electrolyte though the effect is not so remarkable.

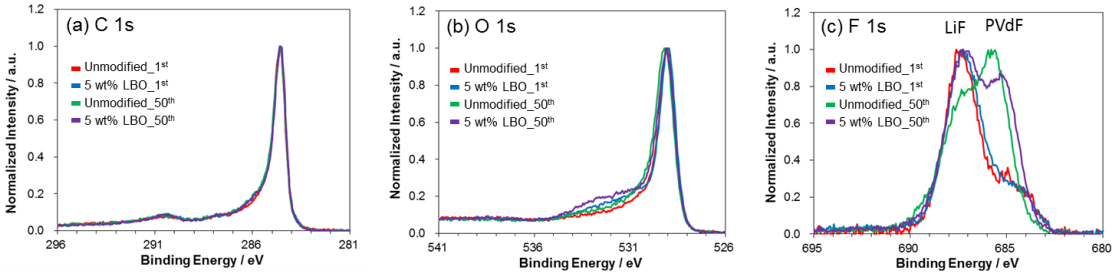

Fig. 6-6 HAXPES (a) C 1s, (b) O 1s and (c) F 1s spectra of uncoated NCM and 5 wt.% LBO-NCM at the fully 4.5 V charged state after the 1st and 50th cycle.

HAXPES Ni 2p and Co 2p spectra for uncoated NCM and 5 wt% LBO-NCM were displayed in Fig. 6-7 and Fig. 6-8, respectively. Any appreciable shifts and the reduction were not observed in the Mn spectra (not shown) during 50 cycling. Fig. 6-7(a) showed Ni 2p HAXPES spectra for uncoated NCM and 5 wt% LBO-NCM at 4.5 V in the charging process after the 1st and 50th charge-discharge cycle. The spectra of Ni $2p_{3/2}$ showed that the oxidation state of Ni was a mixture of Ni^{2+}, Ni^{3+} and Ni^{4+} for all samples [24]. Shimoda et al. reported that the chemical shifts for the trivalent and tetravalent Ni references were very close to each other although the Ni^{4+} peak should appear at a higher binding energy than the Ni^{2+} and Ni^{3+} peaks [25]. In this study, the Ni^{3+} and Ni^{4+} peaks were not separated, either. The shoulders of Ni $2p_{3/2}$ at the lower valence side increased

in intensity after cycling. This fact clearly indicated that part of the active material particle surface remained at the discharged state even when it was fully charged (to 4.5 V) due to an increased overpotential upon cycling as shown in Fig. 6-4. The increase of Ni^{2+} after 50 cycles may suggest the formation of the reduced species such as NiO rock-salt phase; however, the effect of an increase in overpotential could not be eliminated in this figure.

Fig. 6-7(b) showed Ni 2p HAXPES spectra for uncoated NCM and 5 wt% LBO-NCM at 2.5 V in the discharging process after the 1st and 50th charge-discharge cycle. No obvious changes were observed in the Ni $2p_{2/3}$ spectra for both samples after 50 cycles. It showed that Ni was divalent at the active material surface in the discharged $LiNi_{0.5}Co_{0.2}Mn_{0.3}O_2$ at 2.5 V.

In order to eliminate the influence of overpotential, the samples after 1st and 50th cycle were charged to 4.0 V, then constant voltage (CV) charging (until 1 μA) was performed. As shown in Fig. 6-7(c), a peak shift towards the lower binding energy was observed in the unmodified sample after 50 cycles. On the other hand, no peak shift was observed in 5 wt% LBO after 50 cycles as shown in Fig. 6-7(d). The presence of low-valence content of Ni in the unmodified sample suggested the formation of a reduced phase such as the rock-salt NiO phase during cycling, which deteriorated the cycleability and rate capability. Moreover, both samples after 50th cycle were charged to 4.5 V, then constant voltage charging was performed (4.5 V_CV). Taking into account that the peak position of both 4.0 V_CV samples after 2 cycles was the same, the modified 4.5 V_CV sample (Fig. 6-7(d)) shifted to the higher valence side than the unmodified 4.5 V_CV sample (Fig. 6-7(c)). This result also suggested that low valence components were generated in the unmodified samples after 50 cycles.

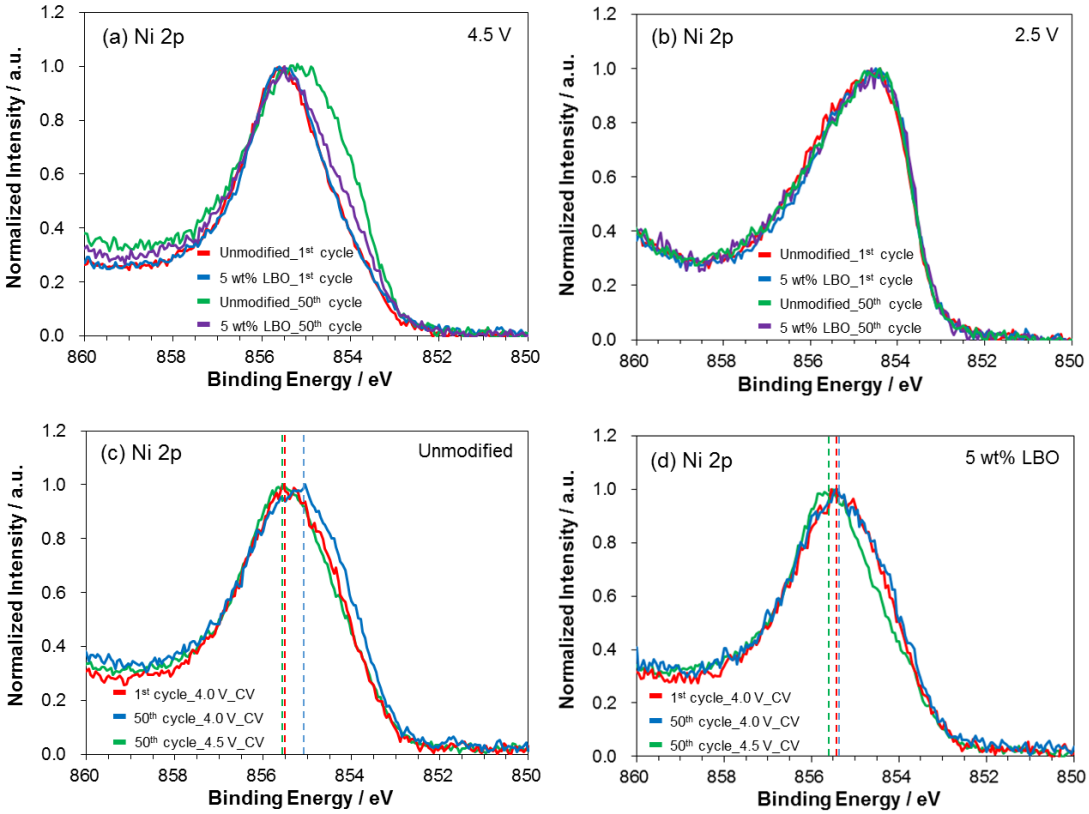

Fig. 6-7 HAXPES Ni 2p spectra of uncoated and 5 wt% LBO-NCM at the (a) 4.5 V charged state and (b) 2.5 V discharged state after the 1st and 50th cycle. Ni 2p spectra of (c) unmodified and (d) 5 wt% LBO-NCM after constant voltage charging at 4.0 and 4.5 V.

Fig. 6-8 showed Co 2p HAXPES spectra for uncoated NCM and 5 wt% LBO-NCM at (a) 4.5 V and (b) 2.5 V states after the 1st and 50th charge-discharge cycling. Compared with Fig. 6-8(a) and Fig. 6-8(b), it was revealed that the Co binding energy (BE) shifted to a lower energy slightly with charging. It has a correlation opposite of the usual, however, it was reported that the higher BE and lower BE of Co $2p_{3/2}$ peak were attributed to lower valence and higher valence, respectively [26-31]. This agrees with the charge

compensation. Therefore, we judge that the shift to the low binding energy with charging means a high-valence state of Co. As shown in Fig. 6-8(a), high energy shoulders slightly appeared in Co $2p_{3/2}$ spectra after 50 cycles for the unmodified sample, which supported that the part of the active material particle surface remained at the discharged state due to an increased overpotential. As shown in Fig. 6-8(b), high energy shoulders slightly appeared in Co $2p_{3/2}$ spectra for the uncoated sample after 50 cycles while such tendency was not observed for 5 wt% LBO-NCM after 50 cycles. The oxidation state of Co can be used to investigate the formation of reduced phases on the surface of $LiNi_{0.5}Co_{0.2}Mn_{0.3}O_2$ in the discharged state [18]. This result in the Co $2p_{3/2}$ spectra indicated that 5 wt% LBO-NCM had an enhanced durability against the surface structural transformation caused by the reduction of surface Co. The presence of Co^{2+} may suggest the formation of a reduced phase, such as the rock-salt CoO phase, during cycling, which deteriorates the cycleability and rate capability. As shown in Figs. 6-8 (c) and (d), no obvious changes were observed in the Co $2p_{2/3}$ spectra for both samples. It was suggested that the valence of cobalt did not change at high voltage during charging.

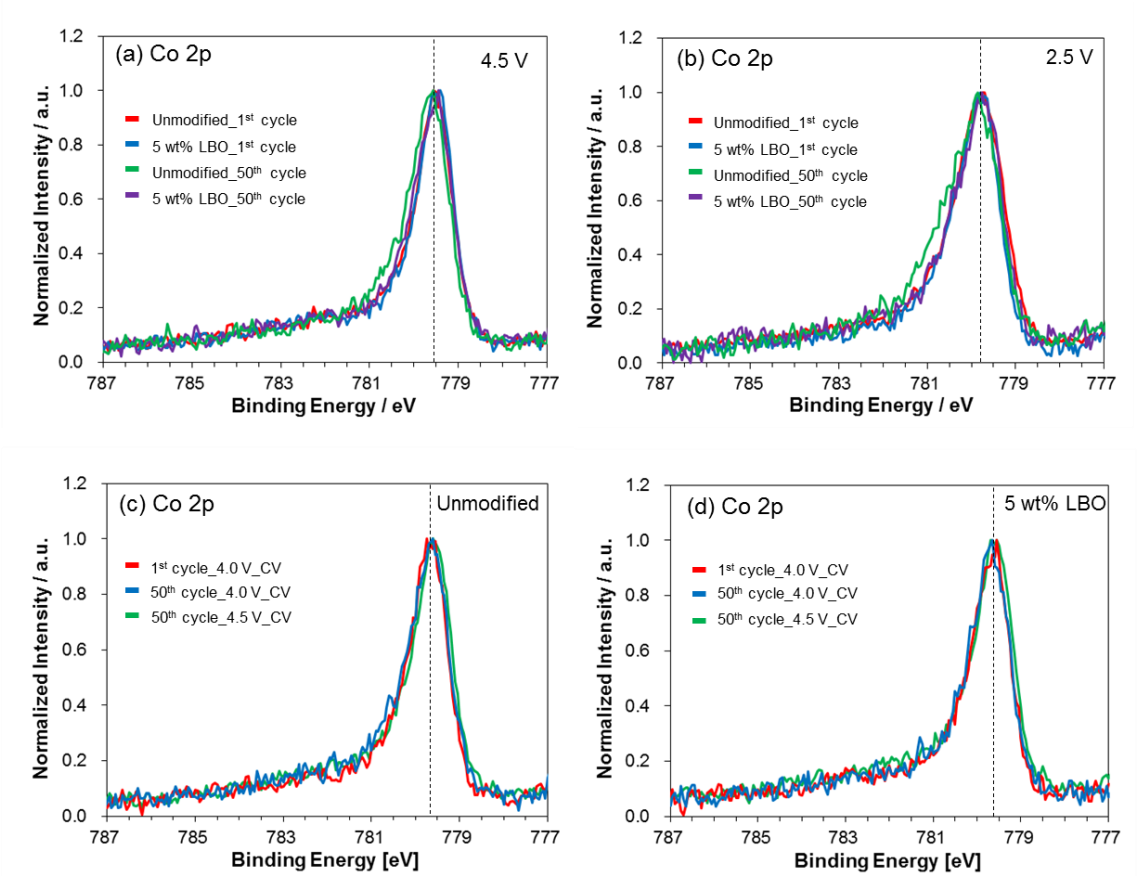

Fig. 6-8 HAXPES Co 2p spectra of uncoated and 5 wt% LBO-NCM at the (a) 4.5 V charged state and (b) 2.5 V discharged state after the 1st and 50th cycle. Co 2p spectra of (c) unmodified and (d) 5 wt% LBO-NCM after constant voltage charging at 4.0 and 4.5 V.

6.4 Conclusions

A highly uniform 10 nm thick LBO layer was coated by an antisolvent precipitation method on the surface of spray pyrolyzed NCM particles. Their diameter was distributed in the range of 500 nm to 1 μm. The discharge capacity of the uncoated sample rapidly decreased with an increase in the charge/discharge rate, whereas the LBO-NCM samples were capable of maintaining higher discharge capacities at high rates. The capacity retention up to 50 cycles was significantly improved by the LBO coating. The EIS measurements indicated that the stable impedance of the LBO-NCM samples during cycling gave improved cyclic performance. Crack formation during cycling was not observed for both uncoated NCM and LBO-NCM prepared by spray pyrolysis. The morphology of LBO coating layer was not changed during cycling, which showed that it was stable and maintained on the surface of $LiNi_{0.5}Co_{0.2}Mn_{0.3}O_2$. HAXPES measurements revealed that the LBO coating suppressed the formation of LiF and organic decomposition products on the cathode particle surface. Furthermore, they suggested that the LBO-coated samples have a high durability against a surface structural transformation caused by the reduction of surface Co during cycling.

References

[1] J.-M. Tarascon, M. Armand, Issues and challenges facing rechargeable lithium batteries, Nature 414 (2001) 359-367.

[2] H.-J. Noh, S. Youn, C. S. Yoon, Y.-K. Sun, Comparison of the structural and electrochemical properties of layered $Li[Ni_xCo_yMn_z]O_2$ (x=1/3, 0.5, 0.6, 0.7, 0.8 and 0.85) cathode material for lithium-ion batteries, J. Power Sources 233 (2013) 121-130.

[3] D. D. MacNeil, Z. Lu, J. R. Dahn, Structure and Electrochemistry of $Li[Ni_xCo_{1-2x}Mn_x]O_2$ ($0<x<1/2$), J. Electrochem. Soc. 149 (2002) A1332.

[4] S.-K. Jung, H. Gwon, J. Hong, K.-Y. Park, D.-H. Seo, H. Kim, J. Hyun, W. Yang, K. Kang, Understanding the Degradation Mechanisms of $LiNi_{0.5}Co_{0.2}Mn_{0.3}O_2$ Cathode Material in Lithium Ion Batteries, Adv. Energy Mater. 4 (2014) 1300787.

[5] F. Lin, L. M. Markus, D. Nordlund, T.-C. Weng, M. D. Asta, H. L. Xin, M. M. Doeff, Surface reconstruction and chemical evolution of stoichiometric layered cathode materials for lithium-ion batteries, Nat. Commun. 5 (2014) 3529.

[6] P. Yan, J. Zheng, J.-G. Zhang, C. Wang, Atomic Resolution Structural and Chemical Imaging Revealing the Sequential Migration of Ni, Co, and Mn upon the Battery Cycling of Layered Cathode, Nano Lett. 17 (2017) 3946-3951.

[7] M. Borner, F. Horsthemke, F. Kollmer, S. Haseloff, A. Friesen, P. Niehoff, S. Nowak, M. Winter, F. M. Schappacher, Degradation effects on the surface of commercial $LiNi_{0.5}Co_{0.2}Mn_{0.3}O_2$ electrodes, J. Power Sources 335 (2016) 45-55.

[8] J. A. Gilbert, I. A. Shkrob, D. P. Abraham, Transition Metal Dissolution, Ion Migration, Electrocatalytic Reduction and Capacity Loss in Lithium-Ion Full Cells, J.

Electrochem. Soc. 164(2) (2017) A389-A399

[9] Y. Shi, M. Zhang, D. Qian, Y. S. Meng, Ultrathin Al_2O_3 Coatings for Improved Cycling Performance and Thermal Stability of $LiNi_{0.5}Co_{0.2}Mn_{0.3}O_2$ Cathode Material, Electrochim. Acta 203 (2016) 154-161.

[10] J.-Z. Kong, S.-S. Wang, G.-A. Tai, L. Zhu, L.-G. Wang, H.-F. Zhai, D. Wu, A.-D. Li, H. Li, Enhanced electrochemical performance of $LiNi_{0.5}Co_{0.2}Mn_{0.3}O_2$ cathode material by ultrathin ZrO_2 coating, J. Alloys Comp. 657 (2016) 593-600.

[11] W. Liu, M. Wang, X. L. Gao, W. Zhang, J. Chen, H. Zhou, X. Zhang, Improvement of the high-temperature, high-voltage cycling performance of $LiNi_{0.5}Co_{0.2}Mn_{0.3}O_2$ cathode with TiO_2 coating, J. Alloys Comp. 543 (2012) 181-188.

[12] K. Liu, G.-L. Yang, Y. Dong, T. Shi, and L. Chen, Enhanced cycling stability and rate performance of $LiNi_{0.5}Co_{0.2}Mn_{0.3}O_2$ by CeO_2 coating at high cut-off voltage, J. Power Sources 281 (2015) 370-377.

[13] D. Wang, X. Li, Z. Wang, H. Guo, X. Chen, X. Zheng, Y. Xu, J. Ru, Multifunctional Li_2O-$2B_2O_3$ coating for enhancing high voltage electrochemical performances and thermal stability of layered structured $LiNi_{0.5}Co_{0.2}Mn_{0.3}O_2$ cathode materials for lithium ion batteries, Electrochim. Acta 174 (2015) 1225-1233.

[14] P. Yan, J. Zheng, M. Gu, J. Xiao, J.-G. Zhang, C.-M. Wang, Intragranular cracking as a critical barrier for high-voltage usage of layer-structured cathode for lithium-ion batteries, Nat. Commun. 8 (2017) 14101.

[15] C.-H. Shen, Q. Wang, H.-J. Chen, C.-G. Shi, H.-Y. Zhang, L. Huang, J.-T. Li, S.-G. Sun, In Situ Multitechnical Investigation into Capacity Fading of High-Voltage $LiNi_{0.5}Co_{0.2}Mn_{0.3}O_2$, ACS Appl. Mater. Interfaces 8 (2016) 35323-35335.

[16] H.-H. Ryu, K.-J. Park, C. S. Yoon, Y.-K. Sun, Capacity fading of Ni-rich

$Li[Ni_xCo_yMn_{1-x-y}]O_2$ ($0.6<x<0.95$) cathodes for high-energy-density lithium-ion batteries : bulk or surface degradation?, Chem. Mater. 80 (2018) 1155-1163.

[17] S. Watanabe, M. Kinoshita, T. Hosokawa, K. Morigaki, K. Nakura, Capacity fade of $LiAl_yNi_{1-x-y}Co_xO_2$ cathode for lithium-ion batteries during accelerated calendar and cycle life tests (surface analysis of $LiAl_yNi_{1-x-y}Co_xO_2$ cathode after cycle tests in restricted depth of discharge ranges), J. Power Sources 258 (2014) 210-217.

[18] F. Lin, D. Nordlund, Y. Li, M. K. Quan, L. Cheng, T.-C. Weng, Y. Liu, H. L. Xin, M. M. Doeff, Metal segregation in hierarchically structured cathode materials for high-energy lithium batteries, Nat. Energy 1 (2016) 15004.

[19] S. Hashigami, K. Yoshimi, Y. Kato, H. Yoshida, T. Inagaki, M. Hashinokuchi, T. Doi, M. Inaba, Durability improvement of $LiNi_{0.5}Co_{0.2}Mn_{0.3}O_2$ cathode coated with lithium boron oxide glass prepared by an antisolvent precipitation method, J. Alloys Comp. submitted.

[20] S. Hashigami, H. Yoshida, D. Ueno, M. Kawano, T. Inagaki, Improvement for the redox durability of Ni-gadolinia doped ceria anodes due to the use of the composite particles prepared by spray pyrolysis method, J. Power Sources 248 (2014) 190-195.

[21] S.-H. Han, J. H. Song, T. Yim, Y.-J. Kim, J.-S. Yu, S. Yoon, Improvement of structural stability during high-voltage cycling in high-nickel cathode materials with B_2O_3 addition, J. Electrochem. Soc. 163(5) (2016) A748-750.

[22] S. Hashigami, Y. Kato, K. Yoshimi, H. Yoshida, T. Inagaki, M. Hashinokuchi, T. Doi, M. Inaba, Influence of lithium silicate coating on retarding crack formation in $LiNi_{0.5}Co_{0.2}Mn_{0.3}O_2$ cathode particles, Electrochim. Acta 291 (2018) 304-310.

[23] Y. Li, F. Lian, L. Ma, C. Liu, L. Yang, X. Sun, K. Chou, Fluoroethylene carbonate as electrolyte additive for improving the electrochemical performances of high-

capacity $Li_{1.16}[Mn_{0.75}Ni_{0.25}]_{0.84}O_2$ material, Electrochim. Acta 168 (2015) 261-270.

[24] J. Im, J. Lee, M.-H. Ryon, Y. M. Lee, K. Y. Cho, Fluorinated carbonate-based electrolyte for high-voltage $Li(Ni_{0.5}Mn_{0.3}Co_{0.2})O_2$/graphite lithium-ion battery, J. Electrochem. Soc. 164(1) (2017) A6381-A6385.

[25] R. Gottschall, R. Schollhorn, M. Muhler, N. Jansen, D. Walcher, P. Gutlich, Electronica state of nickel in barium nickel oxide, $BaNiO_3$, Inorg. Chem. 37 (1998) 1513-1518.

[26] K. Shimoda, T. Minato, K. Nakanishi, H. Komatsu, T. Matsunaga, H. Tanida, H. Arai, Y. Ukyo, Y. Uchimoto, Z. Ogumi, Oxidation behavior of lattice oxygen in Li-rich manganese-based layered oxide studied by hard X-ray photoelectron spectroscopy, J. Mater. Chem. A 4 (2016) 5909-5916.

[27] Y. Huang, B. Zhao, R. Ang, S. Lin, Z. Huang, S. Tan Enhanced thermoelectric performance and room-temperature spin-state transition of Co^{4+} ions in the $Ca_3Co_{4-x}Rh_xO_9$ system, J. Phys. Chem. C 117 (2013) 11459-11470.

CHAPTER 7

General Conclusions and Publication List

7.1 General Conclusions

In this thesis, the author focused surface modification of the active materials with oxides such as silicates and borates and developed mitigation methods for capacity fading of Li-rich NCM and high-Ni NCM cathode materials that are promising for advanced LIBs with high energy density. Degradation factors were discussed in detail and the roles of the surface modification in the improvement of cycle performance were discussed.

The main achievements in this work are summarized as follows:

In Chapter 2, Li_2MnO_3-$LiMn_{1/3}Ni_{1/3}Co_{1/3}O_2$ modified with SiO_2 aerosol was synthesized by simple single-step spray pyrolysis. We found that a small amount of SiO_2 addition remarkably suppressed the capacity and voltage fade of Li_2MnO_3-$LiMn_{1/3}Ni_{1/3}Co_{1/3}O_2$ during cycling. ICP measurements showed that Mn dissolution at an elevated temperature was suppressed by SiO_2 addition. SEM analysis revealed that the addition of SiO_2 enhanced the sintering of the primary particles in the spherical secondary particles, while TEM-EDX analysis indicated that SiO_2 particles were not included inside the primary particles, but on the surface of the primary particles. These results demonstrate that SiO_2 modification is an effective way for suppressing the reaction of Mn dissolution and improving the cycle performance of lithium-excess layered lithium

manganese oxide cathodes.

In Chapter 3, we investigated the effect of acid addition to the starting solutions of the SiO_2-modified Li_2MnO_3-$LiMn_{1/3}Ni_{1/3}Co_{1/3}O_2$ of spray pyrolysis and described the properties of the synthesize particles and the rate capabilities using these particles as the cathode. The addition of citric acid increased the specific surface area and enhanced the rate capability of SiO_2-modified Li_2MnO_3-$LiMn_{1/3}Ni_{1/3}Co_{1/3}O_2$. However, an excess amount of citric acid resulted in the collapsed particles, which showed poor capacity retention. The addition of boric acid deteriorated the rate performance of SiO_2-modified Li_2MnO_3-$LiMn_{1/3}Ni_{1/3}Co_{1/3}O_2$, which was considered to be due to the reduced specific surface area and the presence of a glass layer formed from the lithium and boron components. It was confirmed that the highly dispersed particles having a higher specific surface area obtained by spray pyrolysis using citric acid show better performance in both rate-capability and cycleability.

In Chapter 4, lithium boron oxide (LBO) was coated on $LiNi_{0.5}Co_{0.2}Mn_{0.3}O_2$ by an antisolvent precipitation method to improve electrochemical performance. The conventional impregnation method was also examined for comparison. The $LiNi_{0.5}Co_{0.2}Mn_{0.3}O_2$ particles were coated with a thin and uniform layer of $LiBO_2$ by using the antisolvent precipitation method. On the contrary, the surface was covered with small particles of a mixture of $LiB_2O_4{\cdot}H_2O$, $Li_2B_4O_9$, and $LiBO_2$ in the impregnation method. The LBO layer coated by the antisolvent precipitation method suppressed the capacity fading on cycling more effectively than that coated by the impregnation method. The LBO-coated cathode prepared by the antisolvent precipitation method also exhibited

improved rate capability. Moreover, the LBO-coating suppressed clack formation along the grain boundaries of the secondary particles by inhibiting the penetration of the electrolyte solution into the intergranular cracks. It is therefore concluded that LBO coating by the antisolvent precipitation method is an easy and effective way for improving the cyclability of $LiNi_{0.5}Co_{0.2}Mn_{0.3}O_2$ cathode.

In Chapter 5, we coated $LiNi_{0.5}Co_{0.2}Mn_{0.3}O_2$ particles with a thin layer of lithium silicate by a precipitation method, and investigated the charge and discharge properties. The $LiNi_{0.5}Co_{0.2}Mn_{0.3}O_2$ particles were coated with a thin layer of lithium silicates consisting of Li_2SiO_3 and $Li_2Si_2O_5$. The capacity fading on cycling was successfully suppressed for the lithium silicate-coated sample. During cycling, cracks were formed along the grain boundaries of the secondary particles, which were not observed before cycling. On the other hand, the generation and propagation of cracks were significantly suppressed for the lithium silicate-coated sample. TEM-EDX analysis indicated the presence of Si-rich regions along the grain boundaries inside the secondary particles. This result suggested that the lithium silicate coating suppressed not only the irreversible decomposition of electrolyte solution on the particle surface, but also the crack formation followed by the electrolyte decomposition at the resulting intergranular cracks inside the particles.

In Chapter 6, we synthesized layered $LiNi_{0.5}Co_{0.2}Mn_{0.3}O_2$ using by a spray pyrolysis method and coated the spray pyrolyzed $LiNi_{0.5}Co_{0.2}Mn_{0.3}O_2$ particles with lithium boron oxide (LBO) by an antisolvent precipitation method. The discharge capacity of the uncoated sample rapidly decreased with an increase in the charge/discharge rate, whereas

the LBO-NCM samples were capable of maintaining higher discharge capacities at high rates. The capacity retention up to 50 cycles was significantly improved by the LBO coating. Crack formation during cycling was not observed for both uncoated NCM and LBO-NCM prepared by spray pyrolysis. The morphology of LBO coating layer was not changed during cycling, which showed that it was stable and maintained on the surface of $LiNi_{0.5}Co_{0.2}Mn_{0.3}O_2$. HAXPES measurements revealed that the LBO coating suppressed the formation of LiF and organic decomposition products on the cathode particle surface. Furthermore, they suggested that the LBO-coated samples have a high durability against a surface structural transformation caused by the reduction of surface Co during cycling.

In this thesis, the author clarified the degradation factors during charge-discharge cycling for advanced LIB cathodes such as Li-rich NCM cathodes and high-Ni NCM cathodes. New surface modification methods with borates and silicates using the spray pyrolysis and the anti-solvent precipitation method were developed for mitigating these degradation factors, and it was confirmed that the surface modification is an effective mitigation technique for the capacity fading of the cathodes. On the other hand, it was difficult to suppress the voltage fading of the Li-rich NCM cathodes by surface modification, which is considered to be a major barrier toward practical application of the cathodes. In addition, further investigation is required for the development of life prediction methods using nondestructive analytical techniques.

7.2 Publication List

Chapter 2

"Suppression of Manganese-ion Dissolution by SiO_2 Aerosol Addition from Spray Pyrolyzed Li_2MnO_3-$LiMn_{1/3}Ni_{1/3}Co_{1/3}O_2$"

Satoshi Hashigami, Masayuki Kawanishi, Kei Yoshimi, Satoshi Ujiie, Toru Inagaki, Michihiro Hashinokuchi, Takayuki Doi, and Minoru Inaba: Electrochemistry 84(11) (2016) 842-847.

Chapter 3

"Synthesis of SiO_2-modified Li_2MnO_3-$LiMn_{1/3}Ni_{1/3}Co_{1/3}O_2$ by spray pyrolysis with acid addition as cathode materials for lithium ion batteries"

Satoshi Hashigami, Kei Yoshimi, Masayuki Kawanishi, Satoshi Ujiie, Toru Inagaki, Michihiro Hashinokuchi, Takayuki Doi, and Minoru Inaba: ECS Transactions 73(1) (2016) 11-17.

Chapter 4

"Improvement of cycleability and rate-capability of $LiNi_{0.5}Co_{0.2}Mn_{0.3}O_2$ cathode materials coated with lithium boron oxide by an antisolvent precipitation method"

Satoshi Hashigami, Kei Yoshimi, Yukihiro Kato, Hiroyuki Yoshida, Toru Inagaki, Masakazu Haruta, Michihiro Hashinokuchi, Takayuki Doi, and Minoru Inaba: ChemistrySelect, submitted.

Chapter 5

"Influence of lithium silicate coating on retarding crack formation in $LiNi_{0.5}Co_{0.2}Mn_{0.3}O_2$ cathode particles"

Satoshi Hashigami, Yukihiro Kato, Kei Yoshimi, Hiroyuki Yoshida, Toru Inagaki, Michihiro Hashinokuchi, Takayuki Doi, and Minoru Inaba: Electrochimica Acta 291 (2018) 304-310.

Chapter 6

"Hard X-ray photoelectron spectroscopy analysis of surface chemistry of spray pyrolyzed $LiNi_{0.5}Co_{0.2}Mn_{0.3}O_2$ positive electrode coated with lithium boron oxide"

Satoshi Hashigami, Kei Yoshimi, Yukihiro Kato, Hiroyuki Yoshida, Toru Inagaki, Masamoto Tatematsu, Hiroshi Deguchi, Michihiro Hashinokuchi, Takayuki Doi, and Minoru Inaba: Electrochemistry, submitted.

Acknowledgements

This thesis is a compilation of "Studies on Improved Durability of Cathode Materials for Advanced Lithium-ion Batteries", which was carried out by the author under the supervision of Professor Minoru Inaba at Department of Molecular Chemistry and Biochemistry, Doshisha University during 2016−2018.

The author wishes to express his hearty gratitude to Professor Minoru Inaba for his warm and continuous instruction and encouragement throughout the course of the present work. The author is greatly indebted to Professor Ken Hirota and Professor Yoshiyuki Shirakawa, Graduate School of Engineering, Doshisha University, for their helpful discussion and comments.

The author also wishes to express his sincere thanks to Dr. Michihiro Hashinokuchi, Dr. Masakazu Haruta, Dr. Hideo Daimon and Dr. Takayuki Doi for their useful guidance and fruitful discussions. The author is grateful to all the members of Professor Inaba's laboratory, especially Mr. Masayuki Kawanishi, Mr. Kei Yoshimi, and Mr. Yukihiro Kato, for their excellent contributions to this work.

Furthermore, the author gratefully acknowledges Executive Officer of Research and Development Department of The Kansai Electric Power Company, Inc., Mr. Toshiki Hanada, Executive General Manager of R&D Center Mr. Toshiaki Suga, former Executive General Manager Mr. Hiroshi Yonezawa, Deputy General Manager Mr. Eiji Yonemitsu, Manager of Fundamental Technology Laboratory Mr. Seiichi Higuchi and all the members of Fundamental Technology Laboratory, especially Chief Researcher Dr. Toru Inagaki, Senior Researcher Dr. Hiroyuki Yoshida, Senior Research Engineer Dr. Satoshi Ujiie, Senior Research Engineer Mr. Masamoto Tatematsu, Chief Researcher Dr. Hiroshi Deguchi and Chief Researcher Dr. Eriko Yagasaki, for their stimulating support and assistance.

Finally, the author would like to express special thanks to his wife, Miki, his daughter, Rei, and his parents, Takeshi and Michiko, for their continuous encouragement. This thesis could never have been completed without their assistance and support.

Satoshi Hashigami
March 2019